COMPUTATIONAL MODELING OF SOOT NUCLEATION

by

Seung-Hyun Chung

A dissertation submitted in partial fulfillment
of the requirements for the degree of
Doctor of Philosophy
(Mechanical Engineering)
in the University of Michigan
2011

Doctoral Committee:

Associate Professor Angela Violi, Chair
Professor James F. Driscoll
Professor Volker Sick
Associate Professor Hong G. Im

Acknowledgements

First, I would like to express my deepest appreciation to my advisor, Professor Angela Violi, for her wonderful guidance in preparing this thesis and giving me a great opportunity to explore and develop skills in the many fields needed to successfully conduct research. These skills are not only related to the science but also to written and verbal communications. I also would like to thank my dissertation committee members, Professor James F. Driscoll, Professor Volker Sick, and Professor Hong G. Im.

I have benefited greatly from the interactions with all former and current group members: Dr. Seungho Choi, Dr. Steve Fiedler, Dr. Lam Huynh, Dr. Wendung Hsu, Dr. Hairong Tao, Dr. Soumik Banerjee, Dr. Paolo Elvati, Kyungchan Chae, Kuang-chuan Lin, Jason Lai, Adaleena Mookerjee, and Stephanie.

Most of all, I deeply appreciate to the unconditional supports from my family members. Needless to mention, this thesis would not be possible without my wife, Hyejin Chun. My daughter Taeun always gave me a big smile whenever I came back home. I thank to my father, mother, and brother for their love and firm support throughout my stay at University of Michigan.

I thank to all of my friends here, while it is not possible to list all of them in this acknowledgement. I also thank to the all members of AA bible study group for a lot of unforgettable memories.

Table of Contents

List of Figures

List of Tables

List of Appendices

Chapter 1

Introduction

1.1. Soot

The term “soot” refers to black carbonaceous particles formed by incomplete combustion of hydrocarbon molecules. Soot has many different sources, which include the burning of fossil and biomass fuels in internal combustion engines, furnaces, and boilers, forest fires, or any other deliberate or accidental fires. The production of soot in a flame is a complex process consisting of several mechanisms taking place in series and depends strongly on the fuel composition [1].

The formation of soot has become one of the prime themes in combustion research because of its importance not only for fuel engine efficiency, but also for the environment, and human health. For example, a recent study indicates that soot is currently the second driver of climate change [2] - behind CO_2 but ahead

of methane – and concluded that controlling soot may be the only method of significantly slowing Arctic warming within the next two decades. Also, increased levels of soot particles in the air are linked to health hazards such as heart disease and lung cancer. This association was first demonstrated in the early 1970s [3], and a recent report also estimates that particulate matter (PM) pollution has caused 22,000 – 52,000 deaths per year in the United States since 2000 [4]. Therefore, there has been an intense effort to understand the associated physics and chemistry and, in particular, to develop detailed mechanistic models [5, 6].

Such detailed models usually consist of two principal parts [5-10]: elementary gas-phase chemistry and subsequent soot particle dynamics. The link between these two parts, the transition of gas-phase species to solid particles, is crucial, but very poorly understood. The objective of this study is to explore this process using recently advanced molecular modeling approaches.

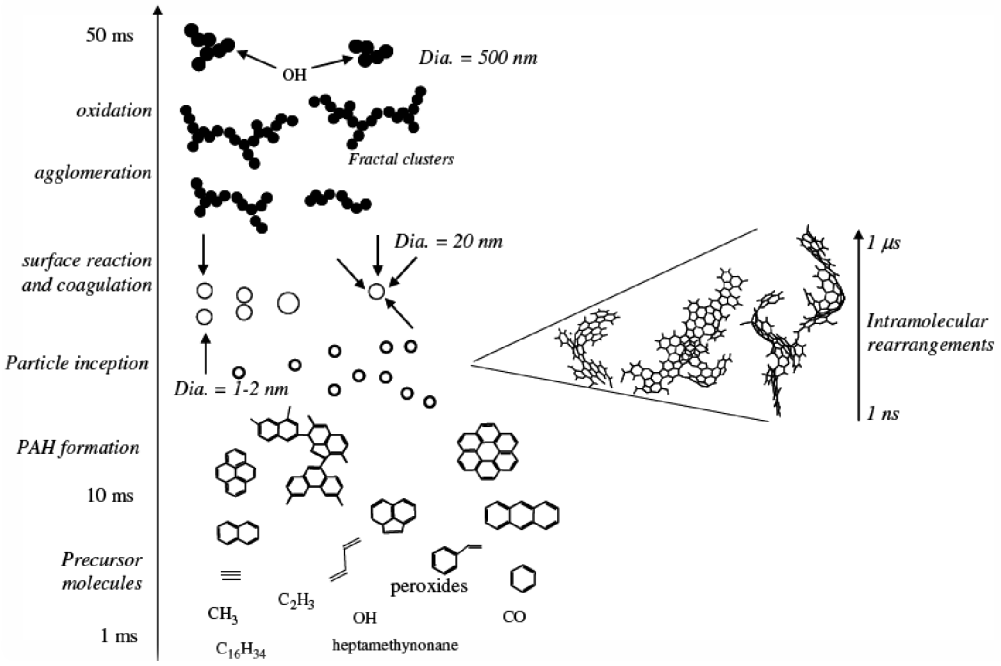

Figure 1.1. Processes involved in the formation of soot particles in flames [11].

1.2. Soot formation process

Soot formation has been viewed as having four major processes [6, 12-16]: soot particle nucleation, soot particle coagulation, soot particle surface reactions, and soot particle agglomeration. Figure 1.1 shows the schematics of the process involved in the formation of soot particles in flames. In the fuel-pyrolysis zone of the flame, the fuel molecules are broken down into various fragments, including C_2H_2, CH_3, hydrocarbon radicals, hydrogen atom, etc. As the combustion process

continues, these molecules combine into hydrogen-rich bigger structures, enabling the transition from the gas-phase to the solid phase. Once soot particles are formed, they collide with each other, forming larger particles [6]. Experimental studies observed that initially the particles look spherical and later acquire a fractal shape [12]. Also, the surface growth occurs mainly via the well-known H-abstraction-C_2H_2-addition (HACA) mechanism in environments of acetylene abundance. This mechanism was first introduced by Frenklach and Wang [6, 17]; it is a repetitive reaction sequence of two principal steps: (i) abstraction of a hydrogen atom from the reacting hydrocarbon by a gaseous hydrogen atom,

$$A_i + H \rightarrow A_{i-} + H_2 \qquad (1.1)$$

followed by (ii) addition of a gaseous acetylene molecule to the radical site formed,

$$A_{i-} + C_2H_2 \rightarrow \text{products} \qquad (1.2)$$

Counter-balancing the surface growth is the oxidation of soot particles, which occurs predominantly by OH radicals and O_2 molecules.

1.3. Soot model

Soot modeling remains one of the most challenging subjects in combustion science. The soot formation process spans a wide range of length scales, starting from sizes corresponding to small molecules, such as acetylene, to large soot particles that are a few micrometers in size, and the relevant time scale also ranges from a few nanoseconds in case of intramolecular rearrangement to a few seconds for convective transport of soot particles. Moreover, unlike other gaseous combustion-generated pollutants (CO, CO_2, and NOx) that have a well-defined chemical composition, each soot particle has its unique chemical composition, size, and morphology [18]. As a result, modeling of the entire process using a single approach is inadequate.

A detailed kinetic model of soot formation can be viewed as comprised of two principal components: gas-phase chemistry and soot particle dynamics [6]. Gas-phase chemistry determines the flame structure using a large set of gas-phase species and reactions, and the particle dynamics describes the evolution of the particle ensemble using the Smoluchowski coagulation equation. Particle dynamics are often modeled by using either a discrete-sectional method [7, 9] or the method of moments [8, 10]. In the discrete-sectional method, [19] the particle ensemble is divided into sections and the particle properties are averaged within each section. In the method of moments, [8, 10] the particle dynamics is rewritten

in terms of moments of the particle size distribution function. While we need the infinite set of these moments to solve the problem, the determination of just the first few derivatives is sufficient for most practical applications, such as obtaining soot volume fraction, specific surface area, light absorption, and light scattering.

The link between gas-phase chemistry and soot particle dynamics is a process called soot nucleation. While this is a very crucial step, the experimental findings are limited and the process still remains the least understood step within the soot formation process [6, 8, 20]. This process is the main focus of this thesis.

1.4. Soot nucleation

Nucleation is a widely used term across many fields of science and technology. Examples range from vapor condensation to protein crystallization, and most of these apparently different phenomena share common property of requiring the overcoming of an energetic barrier and the formation of an initial nucleus [21]. These characteristics apply also to the process of soot nucleation, which bridges the transition from gaseous hydrocarbons to macromolecular building blocks (nanoparticles) that eventually turn into soot. In combustion conditions, however, the peculiar environment, which is characterized by high temperatures and large pools of radicals, make this process very complex.

Nearly three decades ago, Stein and Fahr [22] analyzed the stability of hydrocarbon molecules and concluded that PAH is the most stable bonding configuration at typical flame temperatures. At present, the majority consensus on the general nature of soot particle inception is that the soot particles form via PAH molecules. In an early modeling work of soot formation by Frenklach et al. [23], soot nucleation was described as a purely chemical growth of PAH, and this model significantly under-predicted the corresponding particle size. In their follow-up study [17, 24], Frenklach and co-investigators first proposed that the dimerization, the formation of a compound by the union of two molecules, of PAHs as small as pyrene was necessary to correctly reproduce soot particle size distributions. Miller and co-workers [20, 25, 26] also tested the importance of PAH dimerization in soot nucleation process. They initially ruled out the possibility that soot nucleation can begin with PAH dimerization [25] but later revisited the problem from a kinetic perspective and concluded that the process can occur when the PAH size is four times larger than pyrene [26]. In this later analysis, the lifetimes of dimers under flame conditions were calculated by assuming that the energy of the initial collision could be either accommodated by the PAH molecules themselves or removed by molecules in the bath. However, Schuetz and Frenklach [27] re-emphasized the role of pyrene by investigating the collision of two pyrene molecules using semi-empirical molecular dynamics (MD) method. By comparing the lifetime of pyrene dimer with the collision time with

gas molecules in the bath, they concluded that aromatic dimers of species as small as pyrene can survive long enough to evolve into soot nuclei. As a result, pyrene dimerization as a soot nucleation step has been widely accepted and adopted by many current soot modeling studies [5, 8, 28-30].

However, there is still no definitive experimental data to support the dimerization of pyrene as a key soot nucleation step [20]. Moreover, recent experimental and theoretical studies indicate that pyrene dimerization might not be an important step in soot formation process. For example, Chung and Violi [31] observed pyrene dimers or trimers using MD simulations and concluded that they are not stable enough to grow into soot nuclei at soot generating temperature conditions. Sabbah et al. [5] also presented experimental measurements and theoretical study on the kinetics of pyrene dimerization. They demonstrated that the reaction strongly favors the dissociation of the pyrene dimer at high temperature and concluded that the dimerization of pyrene may not be a key nucleation step.

1.5. Outline

As stated above, the use of pyrene dimerization to model soot nucleation needs to be carefully re-evaluated. In this study, we do that by exploring two possible pathways for soot nucleation: purely chemical growth and collisions among PAH molecules. In order to investigate the soot nucleation process, various molecular modeling approaches, such as molecular dynamics simulation, the kinetic Monte-Carlo method, and ab-initio methods, will be used, and the results will be compared to the available experimental data. Specifically, we will address the effect of flame structures on the soot nucleation process, and propose implementation of the results of this thesis into current soot models.

Brief descriptions of each chapter are presented below:

In Chapter 2, a multiscale computational tool is used to study the formation of nanoparticles via chemical growth in different combustion regimes. The systems chosen for this computational study are two counterflow diffusion flames. The availability of experimental data will help to guide and validate the numerical approach. First we describe the novel implementation of the computational methodology. Then, two different flame configurations are studied, and an analysis of the nanoparticle growth rates, their H/C ratios, and morphologies is reported, together with a detailed discussion of the reactions that contribute to

particle inception.

In Chapter 3, using MD, the clustering of the homomolecular systems of C_{60}, C_{80}, C_{180}, and C_{240} fullerenes is analyzed. We study fullerenes because they have characteristics resembling the particles found in soot, but their simpler structure makes simulation more tractable. The computational findings are then related to the published experimental data discussed in Chapter 2 to assess the feasibility of physical agglomeration.

In Chapter 4, the role of various PAHs, including pyrene, in the soot formation process is investigated. As noted above, the dimerization of PAHs has been regarded as one of the most important physical agglomeration processes in soot formation. In particular, the dimerization of pyrene is widely used as a de-facto nucleation process in many soot modeling studies. However, recent findings indicate that the dimerization of pyrene may not be a key step in soot formation. The results from this study are utilized to obtain accurate nucleation rates for soot models.

In Chapter 5, we re-evaluate the current practical use of pyrene dimerization as a soot nucleation process using collision efficiencies obtained in Chapter 4. In particular, two PAH dimerization pathways – pyrene dimerization and coronene dimerization – are compared. These nucleation pathways are applied to the

detailed soot model, and the results are compared with the experimental data from a jet-stirred / plug-flow reactor (JSR/PFR) system. We also present the procedure to obtain the nucleation rate as an Arrhenius form from the temperature dependent collision efficiency values.

In Chapter 6, the summary of this thesis and future work are presented.

Chapter 2

Formation of nanoparticles via chemical growth reactions

2.1. Objective

In this chapter, a multiscale computational tool is used to study the formation of nanoparticles via chemical growth in different combustion regimes [32, 33]. The systems chosen for this computational study are two counterflow diffusion flames experimentally studied by Kang et al. [34]. The availability of experimental data will help to guide and validate the numerical approach. After a section describing the novel implementations to the computational methodology, two different flame configurations are studied, and an analysis of the nanoparticle growth rates, their H/C ratios, and morphologies is reported together with a detailed discussion of the reactions that contribute to particle inception.

2.2. Computational method

During the past several years, Violi and co-workers [32, 35-41] have reported a computational approach to describe the formation of nanoparticles via chemical reactions using a combination of molecular dynamics (MD) and kinetic Monte-Carlo (KMC) methodologies. The KMC explores the conformational space defined by the interactions between gas-phase species and nanoparticles while the MD module relaxes the nanoparticle structures at flame temperatures. This novel methodology, embedded in the atomistic model for particle inception (AMPI) code, describes the transition from gas-phase species to incipient particles via chemical interactions and it keeps track of particle composition, morphology, surface area, volume, etc.

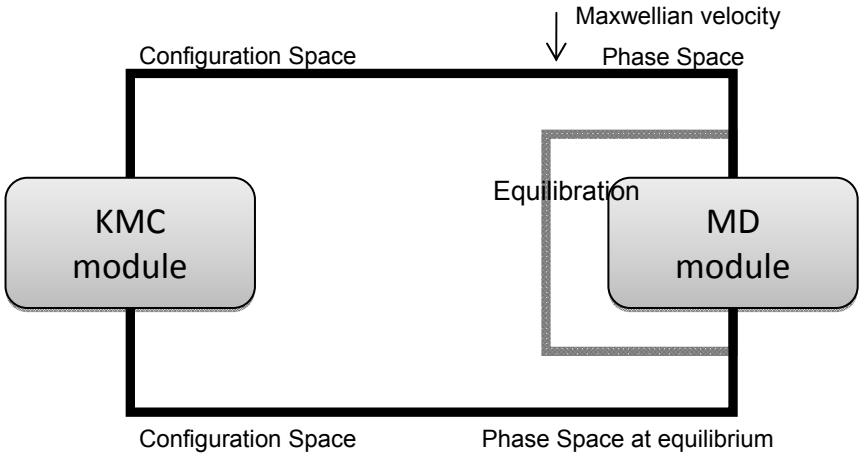

Figure 2.1. Schematic representation of the AMPI code.

2.2.1. Atomistic model for particle inception (AMPI) algorithm

Particle growth occurs on a time scale that is generally not accessible to fully atomistic models such as MD, whereas an atomically resolved Monte Carlo method parameterized by accurate chemical kinetic data is capable of exploring growth over long times and large length scales. The AMPI code proposes a new approach to study the transition from gas-phase to nanoparticles, involving the coupling of KMC and MD. This coupling provides a key to the multiple time-scales involved in the formation of nanoparticles, spanning pico- or nanoseconds for intramolecular processes that can occur for example on a particle surface to milliseconds for intermolecular reactions.

After reading a set of inputs, including temperature, species concentrations in the gas-phase and reaction rates, the AMPI code determines the number of sites available for reactions on the growing structure by identifying each atom as a radical, neutral, aliphatic and aromatic site.

The KMC procedure used in this study is often referred as the BKL algorithm or the n-fold way algorithm [42]. Let us assume that our system is currently in state i, and we have a set of pathways N, and associated rate constants k_{ij}. For each of these pathways, the probability distribution for the first escape time is:

$$p_{ij}(t) = k_{ij}\exp\left(-k_{ij}t\right) \qquad (2.1)$$

The pathway selection procedure proceeds as follows. We imagine that for each of the N escape pathways we have an object with a length equal to the rate constant k_{ij} for that pathway. The sum of these objects gives a total length k_{tot}. Let array element $s(j)$ represents the length of all the objects up to and including object j:

$$\mathrm{s}(j) = \sum_{q}^{j} k_{iq} \qquad (2.2)$$

A random number r, distributed on (0,1), is then drawn and it is multiplied by k_{tot}. Stepping through the array s, the module will stop at the first element for which $s(j) > rk_{tot}$. This is the selected pathway. To advance the clock, we draw a random time from the exponential distribution for the rate constant k_{tot}.

$$\delta t_{\mathrm{KMC}} = \frac{-\ln(r)}{k_{tot}} \qquad (2.3)$$

The time advance has nothing to do with which event is chosen. The time to escape depends only on the total escape rate [40].

Once the system is in the new state, the code performs a MD simulation run that allows the newly formed structure to reach thermal equilibrium. The NVT ensemble, which has the constant number of particles (N), the volume (V), and a well-defined temperature (T), given by the temperature of the heat bath with

which it would be in equilibrium, is used for the simulation. The temperature is set equal to the flame temperature at the location analyzed. The AMPI code alternates between a KMC step and a MD step.

As inputs, the AMPI code requires a detailed description of the gas-phase environment that for this work is provided by the OPPDIF code [43] of the CHEMKIN suite of programs, with a chemical model that includes 172 species and 4890 reactions steps up to the C16 mechanism.[1]

2.2.2. A new version of the AMPI code for C, H, O systems

In order to study the importance of oxidation reactions during the nanoparticle formation process, a new version of the AMPI code has been implemented and the two major modules, MD and KMC, have been modified accordingly in this study. These modifications include (i) new oxygen related terms in the potential and MD module, (ii) oxygen related reactions in KMC module. The new AMPI code can be used to study complex systems composed of C, H and O atoms.

[1] http://www.chem.polimi.it/CRECKModeling/

2.2.2.1. MD module

To describe the bonded interactions within the MD module, we used the adaptive intermolecular reactive empirical bond-order (AIREBO) potential developed by Ni *et al.* [44], who expanded the second-generation empirical bond order (REBO) potential for hydrocarbons, as parameterized by Brenner and co-workers [45-47], to include covalent C-O, H-O, and O-O interactions. This potential allows for chemical bond rupture and bond formation to occur. To increase its utility we then included non-bonded and torsional interactions. For the Lennard-Jones potential, parameters for O-O were taken from the DREIDING force field [48] while C-O and H-O parameters were obtained by the Lorentz-Berthelot combining rules [49] using C-C, H-H and O-O parameters. For the torsional interactions, we considered the following systems: X-C-C-Y combination, X-C-C-O, X-C-O-Y and X-O-O-Y. For the X-C-C-O and X-C-O-Y, the same functional form of AIREBO X-C-C-Y was used and the parameters were obtained from ethanol [50] for the X-C-C-O torsional interaction and from methanol [51] for the X-C-O-Y interaction.

For the X-O-O-Y configuration, considering two bonds *IJ* and *KL* connected via a common bond *JK* involving two sp^3 atoms of the oxygen, we used the following functional form [48]:

$$E_{IJKL} = \frac{1}{2} V_{JK}\{1 - \cos[2(\varphi - 90°)]\} \qquad (2.4)$$

where V_{JK} is the barrier to rotation, φ is the dihedral angle between the *IJK* and *JKL* planes, 90 is the equilibrium angle and 2 is the periodicity. This function is zero at the equilibrium angle and never negative. The rotation barrier (V_{JK}) in the DREIDING force field is 2.0 kcal/mol and this is the same value used in a dihedral single bond involving two sp^3 carbon atoms. Experimental data on H_2O_2, however, indicate a barrier of 7.33 kcal/mol [52] and, therefore, this last value is used in the AMPI code. The impact of replacing H atom with other species on the rotational barrier is expected to be small, considering a theoretical calculation on ClOOCl indicates a barrier of 8.8 kcal/mol [53].

Sometimes stiff Lennard-Jones (LJ) potential can prevent bonding reaction if the transition between non-bonded to bonded interaction is not adequate. To assess this point, we looked at the chemistry of gas-phase collisions between phenyl and OH with different kinetic energies and initial conditions. Collisions in the gas phase are simulated by giving OH a translational velocity towards the phenyl. Incident kinetic energies ranged from 0.5 to 10 eV per molecule. In each case, the outcomes of 10 collisions from different initial random molecular orientations were studied. According to the incident energy, phenyl and OH react if OH gets close to the radical on the phenyl while the phenyl or OH repels each other if they are not favorably oriented. When OH is favorable aligned with

phenyl and the kinetic energy is less than 6.5 eV, we observed the formation of phenol produced through a new bond between C and O.

2.2.2.2. KMC module

We implemented the KMC module of the AMPI code with the following reactions to describe the oxidation of nanoparticles:

$$R_i + O \rightarrow R_{i-1} + CO \quad (2.5)$$

$$R_i - O + O \rightarrow R_{i-1} + CO_2 \quad (2.6)$$

$$R_i - H + O \rightarrow R_{i-1} + CO + \frac{1}{2}H_2 \quad (2.7)$$

$$R_i - H + O/OH \rightarrow R_i + OH/H_2O \quad (2.8)$$

$$R_i + O/OH \rightarrow R_i - O/R_i - OH \quad (2.9)$$

where $R_i - H$ is an aromatic molecule with *i* pericondensed rings, and R_i is its radical. The rates for these oxidation reactions are obtained from benzene and higher PAH oxidation reaction list by Appel et al. [8]. We also implemented the code with oxidation reactions occurring on non-aromatic carbon atoms, and a total

of 158 new reactions were added to the AMPI code. Some of the key reaction rates are listed in Table 2.1:

Table 2.1. Reaction rates in the extended Arrhenius format ($A\ T^{\beta}\ e^{-Ea/RT}$) for some reactions implemented in the KMC module.

Reactions	A	β	E_a	Reference
$C_5H_4O+H=CH_2CHCHCH+CO$	2.10E+61	-13.27	40810	[54]
$C_5H_4O+O=C_4H_4+CO_2$	1.00E+13	0	2000	[54]
$C_5H_5+O=C_5H_5O$	7.06E+04	1.03	-6960	[55]
$C_5H_5+OH=C_5H_4OH+H$	2.15E+30	-4.61	25050	[55]
$C_5H_6+OH=C_5H_5+H_2O$	3.08E+06	2	0	[55]
$C_6H_5+O=C_5H_5+CO$	1.00E+14	0	0	[56]
$C_6H_5+OH=C_6H_5O+H$	5.00E+13	0	0	[57]
$C_6H_5O+CH_3=C_6H_5OCH_3$	1.21E+13	0	0	[58]
$C_6H_5O+O=C_5H_5+CO_2$	1.00E+13	0	0	[54]
$C_6H_5O+O=C_6H_4O_2+H$	8.50E+13	0	0	[54]
$C_6H_5OH+H=C_6H_6+OH$	7.10E+12	0	5385	[59]
$C_6H_5OH+O=C_6H_5O+OH$	2.81E+13	0	7352	[60]
$C_6H_5OH+OH=C_6H_5O+H$	5.00E+13	0	0	[57]
$C_6H_5OH+OH=C_6H_5O+H_2O$	2.95E+06	2	-1312	[61]
$C_6H_6+O=C_6H_5O+H$	2.40E+13	0	4668	[62]
$C_6H_6+OH=C_6H_5+H_2O$	2.11E+13	0	4571	[63]
$C_6H_6+OH=C_6H_5OH+H$	1.32E+13	0	10592	[64]

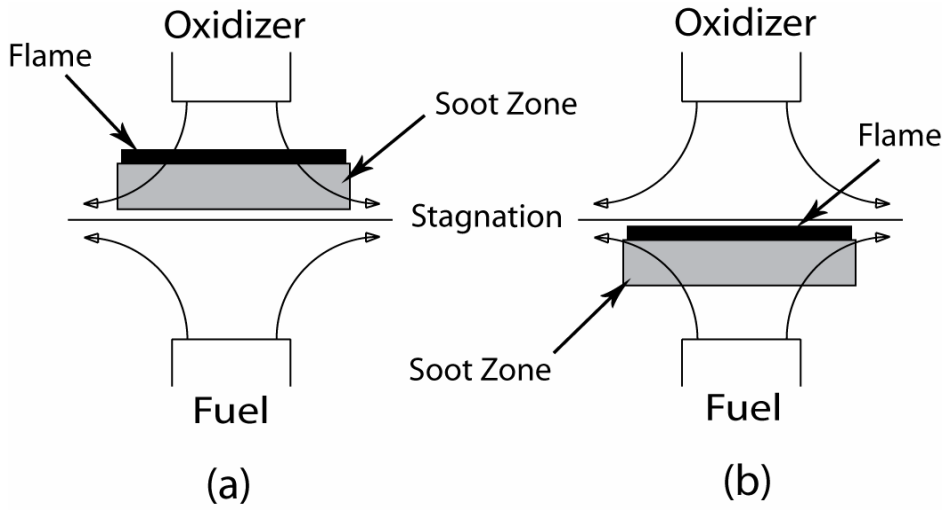

Figure 2.2. Schematics of: (a) soot formation (SF) and (b) soot formation–oxidation (SFO) counter flow diffusion flames [34].

2.3. Counterflow diffusion flame

The systems chosen for this computational study are two counterflow diffusion flames experimentally studied by Kang *et al.* [34]. Counterflow diffusion flames are very attractive from the standpoint of combustion science, since the flame is spatially much wider than an equivalent premixed flame. Particle formation in counterflow diffusion flames has been extensively investigated for their ability to represent turbulent flames within the laminar flamelet model. For diffusion flames, flow characteristics play an important role

in the formation, growth, and oxidation of particles [65, 66] and sooting characteristics can be significantly affected by the flame location. When a diffusion flame is located on the fuel side, the gas velocity is directed toward the flame and particles follow the gas-phase streamlines. On the other hand, when the flame is located on the oxidizer side, the gas velocity is directed to the stagnation plane and particles move away from the flame [34]. As a consequence particle growth will be significantly different and this makes the counter-flow diffusion flames very appealing to study the different processes that contribute to the formation of particles.

Counterflow diffusion flames are frequently located on the oxidizer side when pure hydrocarbon is supplied from the fuel side. Upon appropriate dilution of the fuel and oxidizer streams, however, the flame can be moved to the fuel side [67, 68]. A soot formation (SF) flame is obtained when the flame is located on the oxidizer side of a stagnation plane, such that soot particles once formed are convected away from the flame toward the stagnation plane. Thus, soot oxidation is absent. A soot formation/oxidation (SFO) flame occurs when the flame is located on the fuel side such that soot particles are transported toward the high temperature oxidizer side. Due to oxidation, SFO flames demonstrate similar behavior to sooting premixed flames. Figure 2.2 reports the schematics for the two configurations.

Soot emissions from a combustion source are much less than the amount actually generated within the system. The difference usually comes from the combustion of soot particles in oxygen-containing regions beyond the soot-formation zone [12]. During the formation of polycyclic aromatic hydrocarbons (PAHs) and soot, oxidation reactions often play an important role depending on the flame structure. The effect of oxidation at the molecular level can instigate competing reactions: carbon mass is diverted from further growth, while O and OH can promote formation of soot by building up the radical pool [6]. It is the purpose of this work to get insights on the effects of oxidation environments on nanoparticle growth using computational tools.

For this study we analyzed a SFO and a SF flame of propane. The flame conditions for the SFO flame were (X_{C3H8}, X_{O2}) = (0.25, 0.7) with the fuel flow composed of 25 % C_3H_8 in N_2 and the oxidizer stream of 70 % O_2 and 30 % N_2. The SF flame had (X_{C3H8}, X_{O2}) = (1.0, 0.3). The volume-averaged nozzle exit velocities for the SF and SFO flames were 0.2 m/s for the fuel and oxidizer streams. Both the nozzle exit diameter and the separation distance between the two nozzles were 14.2 mm. As mentioned above, these flames have been experimentally investigated by Kang *et al.* [34] who employed soot extinction-scattering, PAH fluorescence, and laser Doppler velocimetry measurements to determine the characteristics of the particle zone structures.

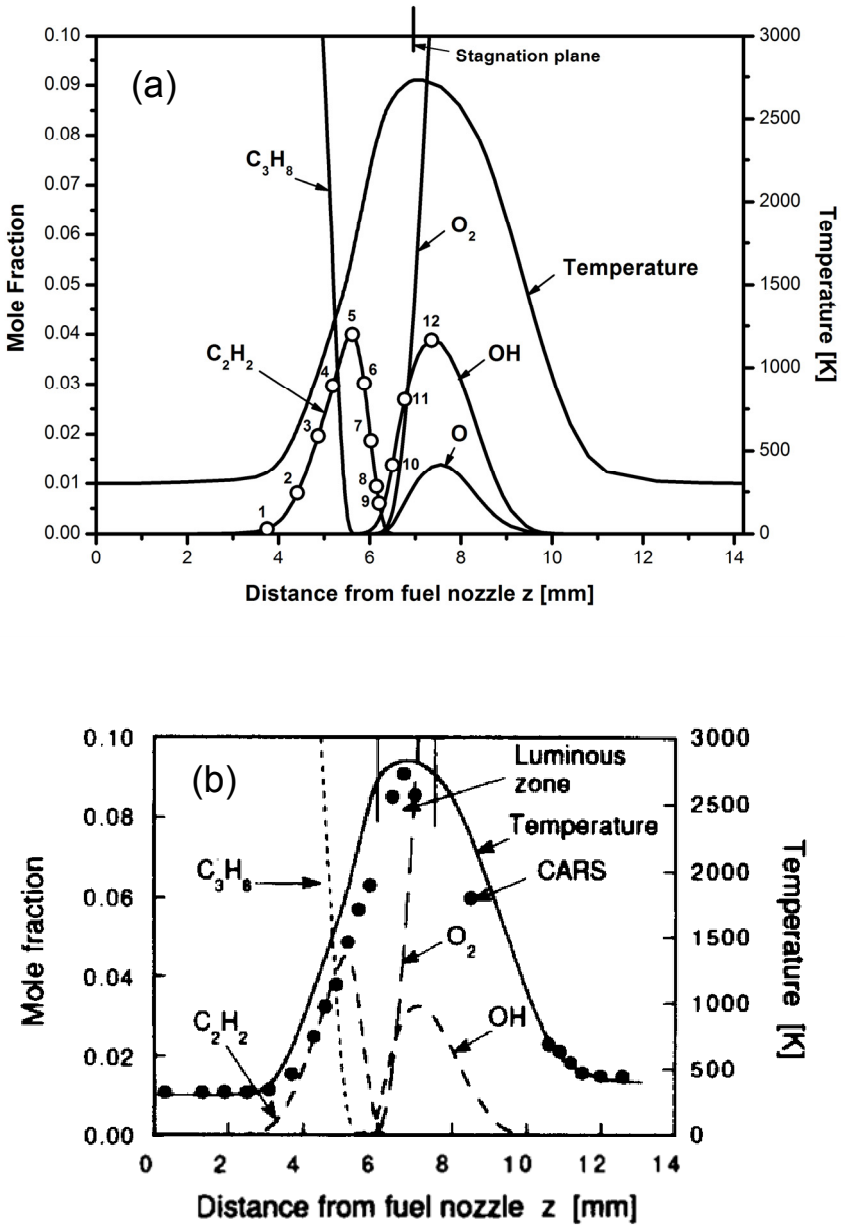

Figure 2.3. (a) Numerical results for the temperature profile and C_3H_8, C_2H_2, O_2, OH and O concentrations in the SFO flame. (○) represents the locations sampled by the AMPI code. (b) Experimental data from Kang et al. [34].

2.3.1. Soot-formation-oxidation (SFO) flame

Figure 2.3 (a) shows the computed resulted obtained with OPPDIF [43] for the concentrations of propane, oxygen, acetylene, hydroxyl and oxygen radicals together with the temperature profile for the SFO flame (X_{C3H8}, X_{O2})= (0.25, 0.7). These conditions correspond to a flame location close to the gas-phase stagnation plane. In such case, the soot zone is located on the fuel side and particles are transported toward the particle stagnation plane, that is, toward the higher temperature region, where they are finally get oxidized.

The computed temperature values by OPPDIF code [43] agree well with the measured temperature profile (Figure 2.3 (b)) from coherent anti-Stokes Raman spectroscopic measurements reported by Kang *et al.* [34]. Propane is pyrolyzed to form hydrocarbons such as C_2H_2 that exists in the range z = 3 – 6 mm where z is the distance from the fuel nozzle. In the same figure the computed concentration profile of OH is shown in order to identify the flame location. The particle stagnation plane is located around Point 11 and the luminous zone has been experimentally identified between Points 9 and 12.

To determine the characteristics of the sooting zone, we analyzed several locations in the flame covering 12 Points from the fuel to the oxidizer side. The circles in Figure 2.3 (a) show the locations sampled with the AMPI code. Upon

inclusion of the gas-phase species concentrations and temperature into the AMPI code, several runs were carried out to study particle formation in these twelve locations. Since the AMPI code follows the growth of a single particle at a specific location of the flame, we generated an ensemble of twenty particles for each location. Figure 2.4 shows the number of carbon atoms present on the nanoparticles as a function of time for locations 4 through 7. At Points 1-3 corresponding to the early formation of acetylene, the particle growth was found to be very slow. For example, at z = 3.75 mm (Point 1) the first reaction selected by the KMC module of the AMPI code was hydrogen abstraction and it took 1096 seconds to proceed, which is very slow when compared with the flame velocity at that point (11.23cm/s). Towards the peak of acetylene the growth rate increased dramatically.

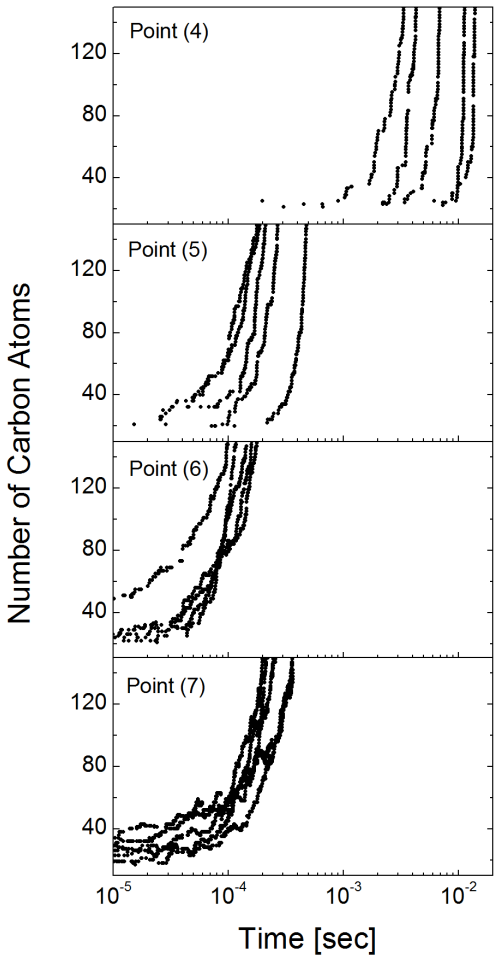

Figure 2.4. Number of carbon atoms on the particle as a function of time for z = 5.19 mm (Point 4), z = 5.62 mm (Point 5), z = 5.88 mm (Point 6) and z = 6.03 mm (Point 7).

At z = 5.19 mm (Point 4) particle growth occurs on the order of 10^{-3} sec as shown in Fig. 3 and in the same location the gas velocity is ~ 10 cm/s. If we assume that particle's velocity is similar to the gas velocity, the particle formed in Point 4 would proceed O(10^{-3} sec) * O(10 cm/s) = O(0.1 mm) and with the distance between locations 4 and 5 being around 0.43 mm, the particle might be convected away to Point 5 before it significantly increases in size. The nanoparticle growth rate dramatically changes between locations 4 and 5. At location 5, particle growth took O(10^{-4} sec) and since the gas velocity at this point is similar to the one in location 4, particles move O(0.01 mm). According to these results, we can conclude that the particle inception becomes significant in this SFO flame between locations 4 and 5 where the concentration of acetylene reaches its peak. The computational results are in very good agreement with the PAH signal Q_f measured by Kang *et al.* [34] that starts to rise at z = 4 mm, and with the scattering signal Q_{vv} that begins to rise at z = 5mm, too. This indicates that the particle inception process is well described by the AMPI code in this environment. At z = 5.62 mm (Point 5), z = 5.88 mm (Point 6) and z = 6.03 mm (Point 7), the computed growth rates are similar because of two counterbalancing effects. As we move towards the stagnation plane, the temperature increases going from 1700K at Point 5 to 2200K at Point 7, and the concentration of hydrocarbons, including acetylene, decreases. Figure 2.5 reports examples of particle configurations obtained at Points 5, 6 and 7.

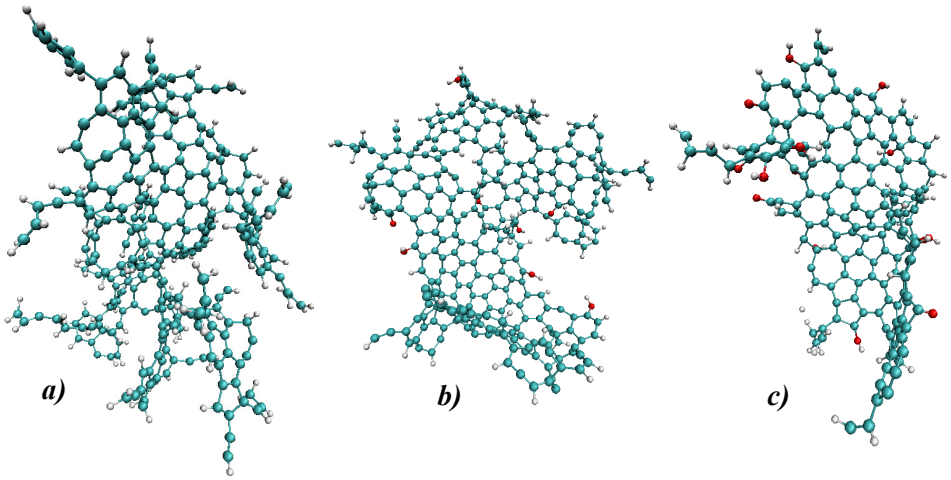

Figure 2.5. Carbonaceous nanoparticles produced by the AMPI code at points 5 *(a)*, 6 *(b)*, and 7 *(c)*. Carbon atoms are shown in blue, hydrogen atoms are silver and oxygen atoms are red.

Table 2.2 lists the main reactions occurring at Points 5, 6 and 7. Ring closure reactions, in which nascent rings are formed through dehydrogenation mechanisms [69], acetylene addition and hydrogen eliminations and additions are the most frequent reactions. The importance of C_2H_2 in early inception zone is also in agreement with the experimental data by Kang *et al.* which shows the coincidence of the maximum values of PAH fluorescence, soot particle number density, at the point of the onset of the scattering signal indicates that the particle inception occurs from PAH through C_2H_2.

Table 2.2. Principal reactions occurring in the particle inception region of the SFO flame.

Reactions	% at Point 5	% at Point 6	% at Point 7
Cyclodehydrogenation	18.2	15.1	8.0
Abstraction reactions			
Hydrogen abstraction by H radical	13.8	14.5	14.2
Hydrogen abstraction by CH_3 radical	9.3	3.9	0.8
Hydrogen abstraction by OH radical	2.3	7.5	11.1
Addition reactions			
C_2H_2	31.7	23.2	10.8
C_2H_4	6.9	1.1	0.1
C_4H_2	0.9	0.5	0.2
CH_3	2.2	0.6	0.2
H	12.4	26.3	35.7

Ethylene addition to radicals on the growing seed plays a significant role at Point 4, but this contribution diminishes faster than the contribution of acetylene as we move towards the stagnation plane, since the C_2H_4 concentration starts decreasing at 5.3 mm while acetylene peaks at 5.6 mm (Point 5).

In the region from z = 5.6 mm to 6 mm (Points 5 - 7) hydrogen addition to radical sites on the particle is significant and this causes a reduction of the number of reactive sites on the growing seed. At Point 5 (z = 5.62 mm), hydrogen abstraction by CH_3 also significantly contribute to the particle growth. At z = 5.88 mm corresponding to Point 6, hydrogen abstraction by OH becomes important.

H/C ratios of the particles generated at locations 5, 6 and 7 are reported in Figure 2.6 as function of time. We carried out the simulations until particles of similar sizes were produced by the AMPI code. Low values of the H/C ratios at z = 5.88 mm (Point 6) and 6.03 mm (Point 7) are indicative of more aromatic structures as compared to higher values of H/C ratios obtained at z = 5.62 mm, location 5. This is due to the significant concentration of hydrocarbons that can react with the particle and to the cyclodehydrogenation reactions in which hydrogen atoms are lost, and a new ring is created by the formation of a new transannular C-C bond [69]. At Point 5 the low temperature (T ~ 1680K) causes a low rate of the cyclodehydrogenation reactions.

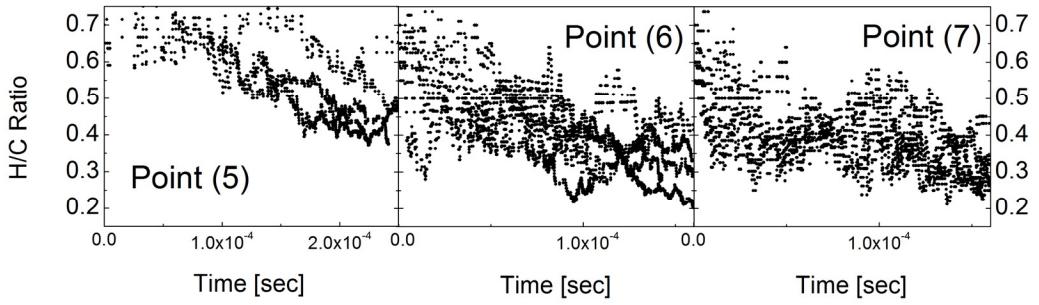

Figure 2.6. H/C ratios of nanoparticles at points 5, 6 and 7 as a function of time.

Ellipticity parameters are often used to characterize particle morphology. To this end, the aspect ratio (AR), defined as AR = *a/b* where *a* is a major axis and *b* is a minor axes of the particle is computed to get insights on the shape of the particles formed in flame. Figure 2.7 shows the aspect ratios of particles at locations 5, 6 and 7 in the flame. The AR of a circle is one and of an ellipse with the ratio of axes 2:1 is equal to two.

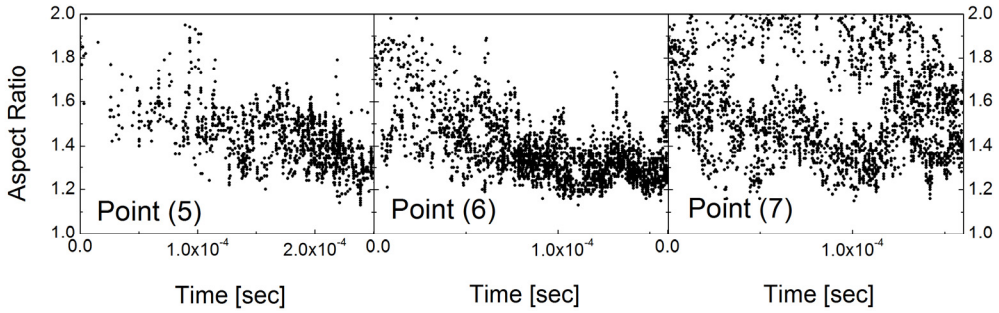

Figure 2.7. Aspect ratios of nanoparticles at points 5, 6 and 7 as a function of time.

The results reported for Point 7 are due to particle fragmentation. Reactions related to oxidation and the following MD simulation sometimes led the particle into two pieces and AMPI code follows the growth of the largest fragment. In this case, their aspect ratios change rapidly and become bimodal.

At z = 6.15 mm (Point 8 in Figure 2.3) oxidation reactions start to play an important role and we did not observe particle growth beyond this location. To study the effect of oxidation, we used a particle produced at Point 7 - $C_{90}H_{44}O_5$ as initial seed for the analyses at Points 8 through 12. The reason for this approximation was to determine the effects of O and OH radicals, despite the fact that likely a particle formed at Point 7 would undergo further chemical reactions, coagulation growth and other mechanisms before it reaches the oxidation region.

Figure 2.8 shows the number of carbon atoms present on the growing species as a function of time at locations 8 - 12. The curves are representative of different runs. The decrease at long time is indicative of the breakdown of the particles into small fragments. At z = 6.15 mm (Point 8), some particles are reduced in size and others undergo addition from the gas phase. Around z = 6.21 mm, location 9, the mole fractions of OH and C_2H_2 become almost equal and the burnout is significant. The contributions of OH and O to the particle growth are twofold: they remove carbon from the nanoparticle producing CO and CO_2 and they react with radicals on the particle, preventing further addition of hydrocarbons.

From Point 8 toward the oxidizer stream, an increasing concentration of OH radicals oxidizes the particles causing a decrease of the particle sizes. This result agrees well with the experimental data showing after z = 6 mm a decrease in the particle size and volume fraction. Although a decrease of PAH is mitigated by the formation of PAH from the oxidation of particles, the net amount of PAH gradually decreases because of oxidation by radicals such as OH. This counterflow flame located near the stagnation plane can be classified as a soot formation-oxidation flame as the particle mechanism is dominated by oxidation.

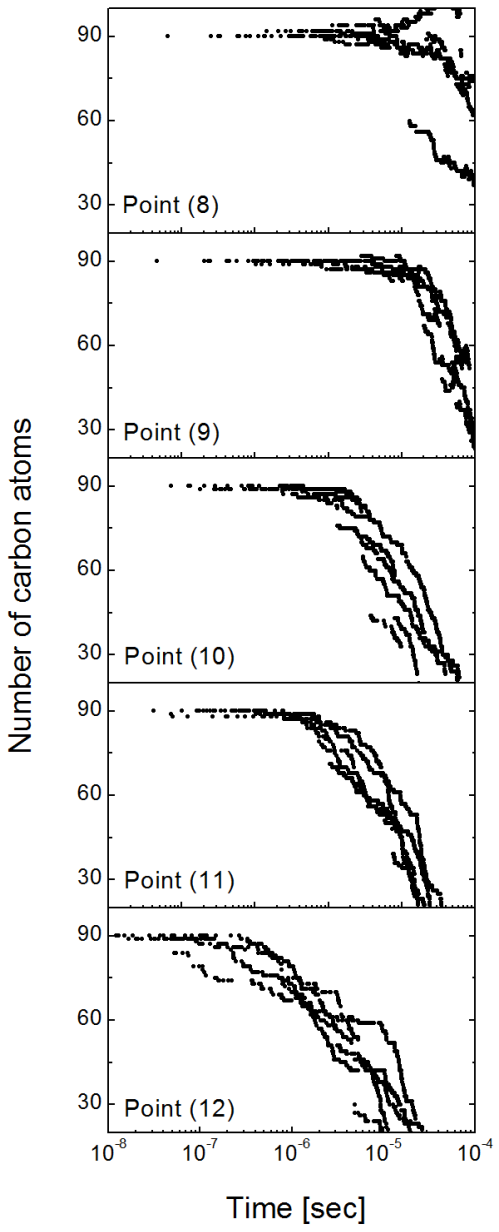

Figure 2.8. Number of carbon atoms on the growing particle as a function of time for z = 6.15 mm (Point 8), z = 6.21 mm (Point 9), z = 6.50 mm (Point 10), z = 6.77 mm (Point 11) and z = 7.36 mm (Point 12).

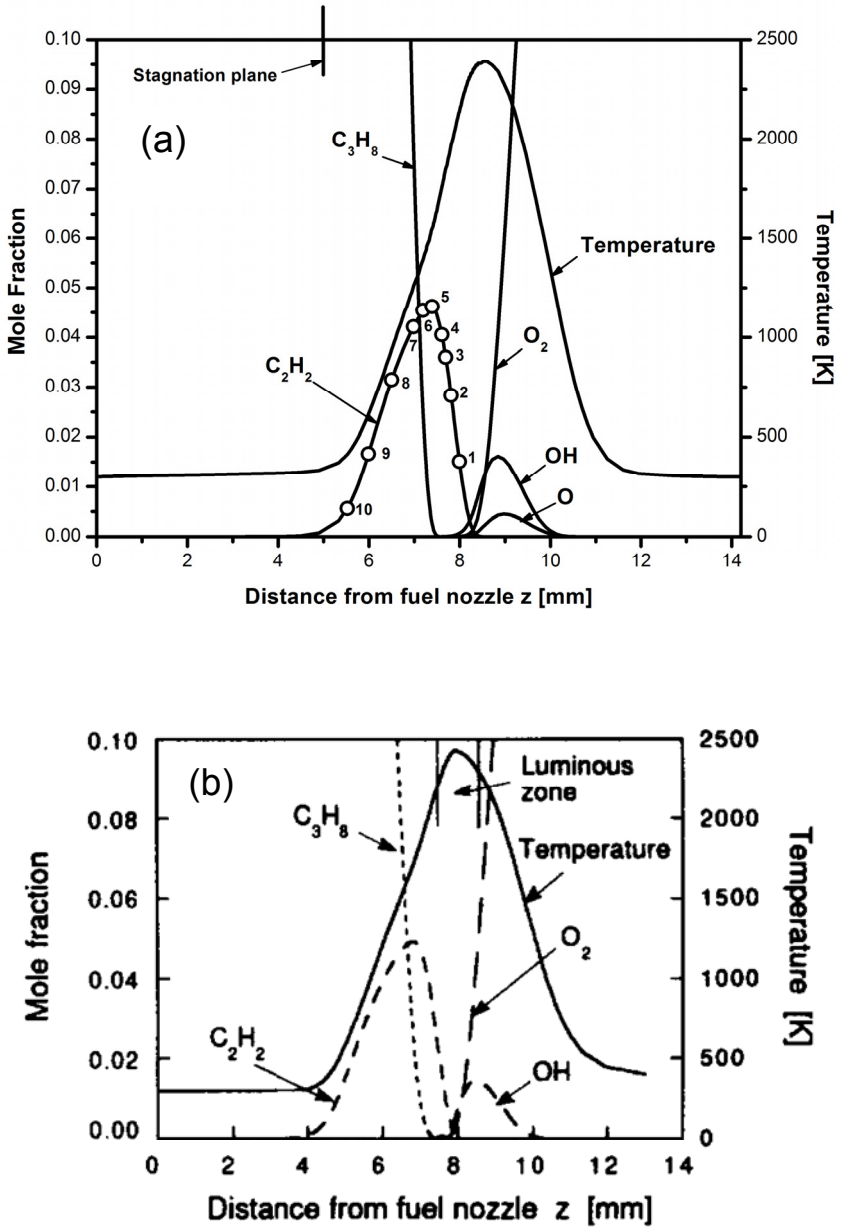

Figure 2.9. (a) Numerical results for the temperature profile and C_3H_8, C_2H_2, O_2, OH and O concentrations in the SF flame. (○) represents the locations sampled by the AMPI code. (b) Experimental data from Kang et al. [34].

2.3.2. Soot-formation (SF) flame

Figure 2.9 (a) illustrates the computed profiles of temperature and species concentrations for the soot-formation (SF) flame (X_{C3H8}, X_{O2}) = (1.0, 0.3). In this case, the soot zone is located on the oxidizer side in the region of 5 mm < z < 7 mm, next to the flame zone of 7.5 mm < z < 8.5 mm and particles are transported away from the flame toward the fuel side. In a manner similar to the previous flame, we analyzed 10 locations in the flame to study the particle growth. The locations are reported in Figure 2.9 (a). Figure 2.10 shows the change in number of carbon atoms on the growing particle as function of time for Points 3 through 7. No significant particle growth was computed at Points 1 and 2 (z = 8.0 mm and z = 7.8 mm, respectively). At Point 3, z = 7.7 mm, particle growth suddenly becomes significant. The computational results are in agreement with the experimental measurements by Kang *et al* [34] showing that the soot inception is located around z ~ 7 mm, having almost the same temperature as in the case of the SFO flame (Point 5). Nanoparticles are formed in the region between the flame front and the maximum aromatic concentration since the significant presence of H-atoms is able to initiate the growth process by abstracting H atom from aromatic sites. The fastest growth rate was computed at z = 7.7 mm (Point 3) and z = 7.6 mm (Point 4) and no significant growth was obtained after Point 7 due to the low temperature and rapid decrease of hydrocarbon concentrations.

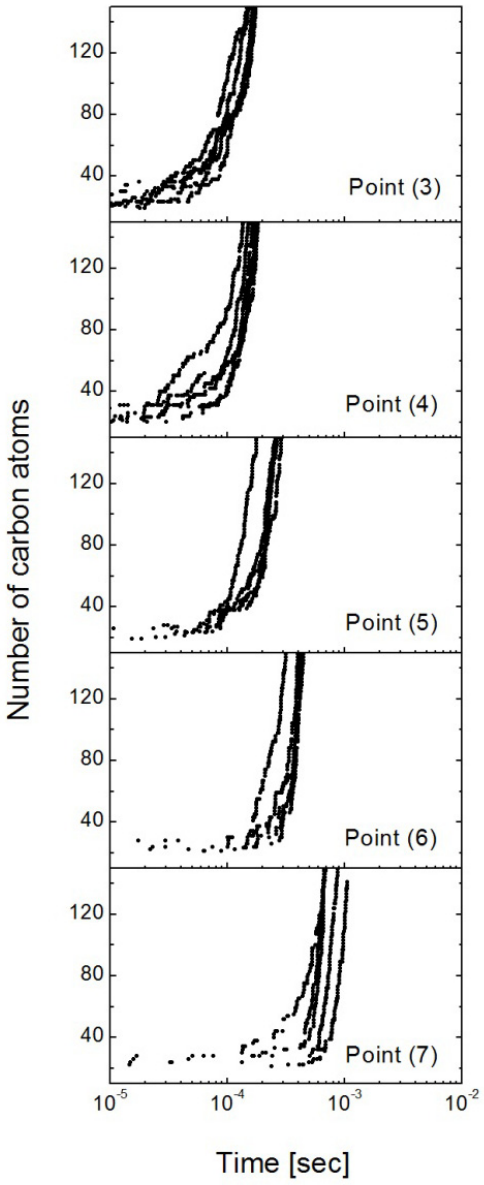

Figure 2.10. Number of carbon atoms on the growing particle as function of time in the SF flame at z = 7.7 mm (Point 3), z = 7.6 mm (Point 4), z = 7.4 mm (Point 5), z = 7.2 mm (Point 6) and z = 7.0 mm (Point 7).

Figure 2.11 shows examples of particle configurations formed at various locations in the flame. Differently from the SFO flame, at Point 3, where the particle inception begins, we observed oxygen atoms on the particle since the inception region is close to the flame. The number of oxygen atoms on the particle decreases moving further from the flame. We identified a maximum concentration of 15 % of oxygen atoms on the particles.

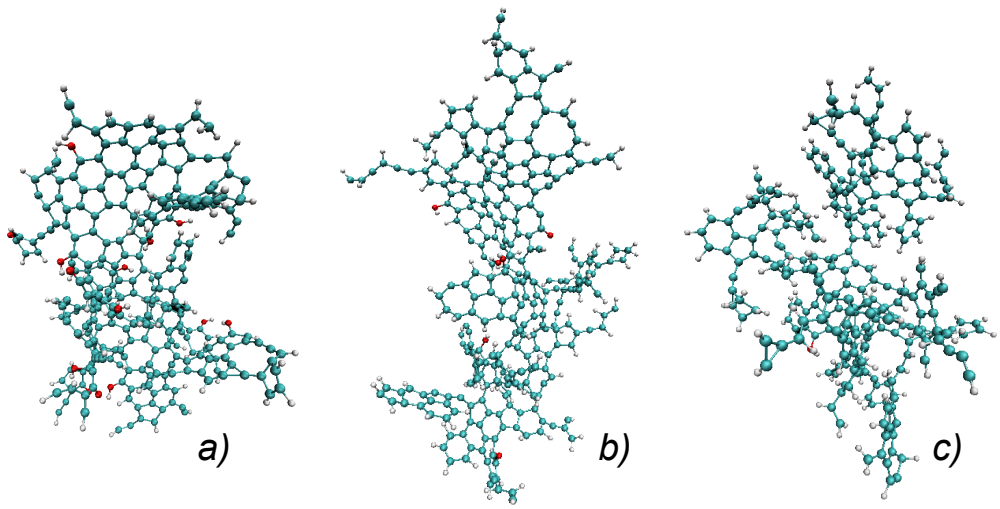

Figure 2.11. Carbonaceous nanoparticles produced by AMPI code at points 3 *(a)*, 4 *(b)* and 5 *(c)*. Carbon atoms are shown in blue, hydrogen atoms are silver and oxygen atoms are red.

Figure 2.12 shows the change in H/C ratio for the particles produced at Points 3 - 5 together with the change in the aspect ratio. The values and trends are very similar to the ones reported for the SFO flame. Table 2.3 reports the major reactions occurring at Points 3, 4, 5, 6 and 7. Acetylene additions still play an important role and PAH contribution to particle growth is not significant in this region.

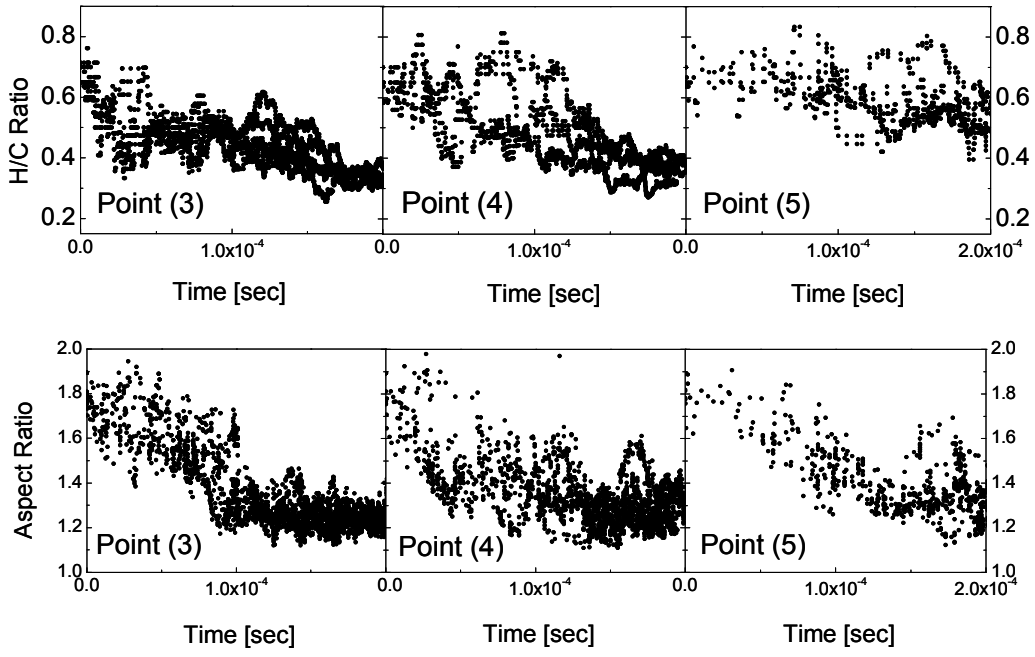

Figure 2.12. H/C ratio and Aspect Ratio of nanoparticles produced at Point 3 through 5 in the SF flame.

Table 2.3. Major reactions in the soot inception region of SF flame.

Reaction	% at Point 3	% at Point 4	% at Point 5	% at Point 6	% at Point 7
Cyclodehydrogenation reactions	10.6	14.0	16.7	16.0	14.8
Abstraction reactions					
Hydrogen abstraction by H radical	13.8	12.5	10.2	9.7	7.0
Hydrogen abstraction by CH_3 radical	2.3	5.2	8.0	12.0	16.4
Hydrogen abstraction by OH radical	10.2	7.2	3.8	1.5	0.8
Addition reactions					
C_2H_2	20.3	29.9	36.4	34.7	33.1
C_2H_4	0.3	2.2	6.7	10.6	14.4
C_4H_2	0.4	0.7	0.4	0.8	0.9
CH_3	0.4	1.0	2.2	3.2	3.1
H	28.7	21.2	11.7	9.5	7.4
PAH	0.0	0.0	0.2	0.6	1.1

The contribution of hydrogen abstraction by hydrogen and OH radicals to particle growth decreases moving further from the oxidizer side, and at the same time hydrogen abstractions by hydrocarbon radicals become more frequent. Hwang et al. suggested that in the particle growth region, hydrocarbon radicals are likely responsible for the growth by abstracting hydrogen and producing radical sites on the surface of particles before the addition of C_2H_2 becomes significant [67, 68]. Our results reported in Figure 2.10, however, show that the particle growth rate significantly drops after Point 4. To assess the importance of hydrogen abstractions by hydrocarbons, we conducted a sensitivity analysis by switching off these reactions in the AMPI code. Figure 2.13 reports the change of number of carbon atoms with time without hydrogen abstraction by hydrocarbon radicals for Points 3 - 7. When comparing Figure 2.10 and Figure 2.13, we notice that hydrogen abstraction reactions by hydrocarbon radicals contribute to the particle growth for Points 5 through 7 but their contribution was not significant enough to change the overall rates. This is mainly due to the temperature drop in this region. In summary, hydrogen abstractions by hydrocarbon radicals are not a major factor to boost particle growth in low temperature region.

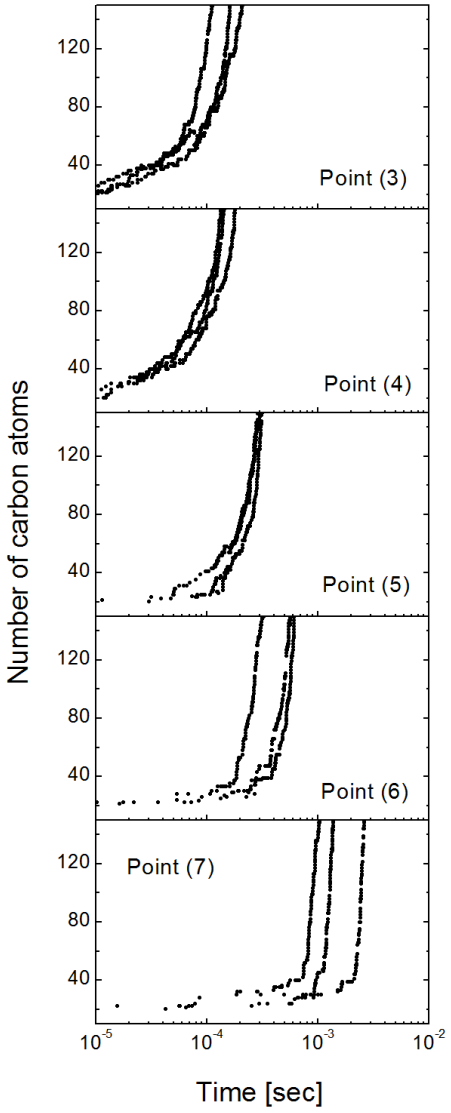

Figure 2.13. SF flame without hydrogen abstraction reaction by hydrocarbon radicals. Number of carbon in a particle as a function of time for z = 7.7 mm (Point 3), z = 7.6 mm (Point 4), z = 7.4 mm (Point 5), z = 7.2 mm (Point 6) and z = 7.0 mm (Point 7).

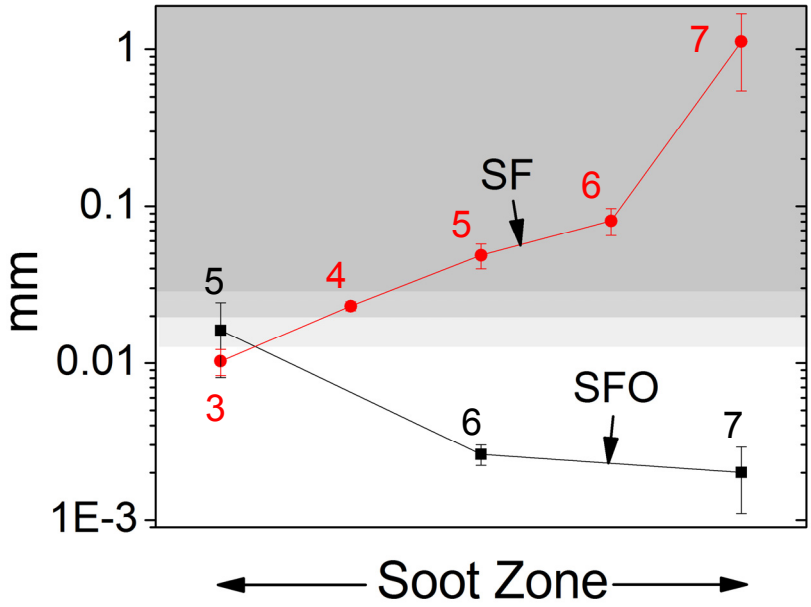

Figure 2.14. The length scales (y axis) calculated by multiplying the growth time taken for a particle's mass to reach the mass of a pyrene dimer by the flow rate at the corresponding flame location. Black - Points 5, 6, and 7 in the SFO flame, Red - Points 3, 4, 5, 6, and 7 in the SF flame.

2.3.3. Comparison between the SF flame and the SFO flame.

Figure 2.14 shows the length scales calculated by multiplying two values: (i) the growth time taken for a particle's mass to reach the mass of a pyrene dimer,

and (ii) the flow rate at the corresponding flame location. These values are calculated at the points that correspond to the soot zones of the SFO flame and the SF flame. This figure shows that the length scales in the SF flame are significantly longer than those in the SFO flame except at one point. Considering the total soot zone length is 1 ~ 3 mm, the length scales in the SF flame (0.01 ~ 1 mm) are too long to consider chemical reactions as a viable mechanism for soot inception, compare to the length scales in the SFO flame (0.001 ~ 0.01 mm). Therefore, unlike the SFO flame, AMPI is an adequate approach to describing the particle inception in the SF flame, where hydrogen radicals are rare and the temperature is relatively low (see Figure 2.9).

Figure 2.15 reports the concentration of PAH in both flames. PAH concentration is defined as the sum of aromatic species obtained from the CHEMKIN results and include as main species C_5H_5, C_5H_6, C_6H_5, C_6H_6, C_6H_8, C_6H_{10}, $C_6H_5C_2H$, $C_6H_5C_2H_2$, $C_6H_5C_2H_3$, indenyl, naphthalene, naphthyl, acenapthalene and acenapthyl. The concentration of PAH in the SF flame is almost twice that in the SFO flame. In the SF flame, as the stagnation plane is approached (z = 5 mm) with the drop in temperature, the particle inception due to chemical growth is expected to decrease (Figure 2.14), while PAH concentrations continuously increase until the gas stagnation plane is reached. Hence, soot inception via PAH agglomeration, instead of PAH growth through the H-

abstraction-C_2H_2 addition (HACA) reactions, can be a viable particle formation process under these conditions [68, 70-72].

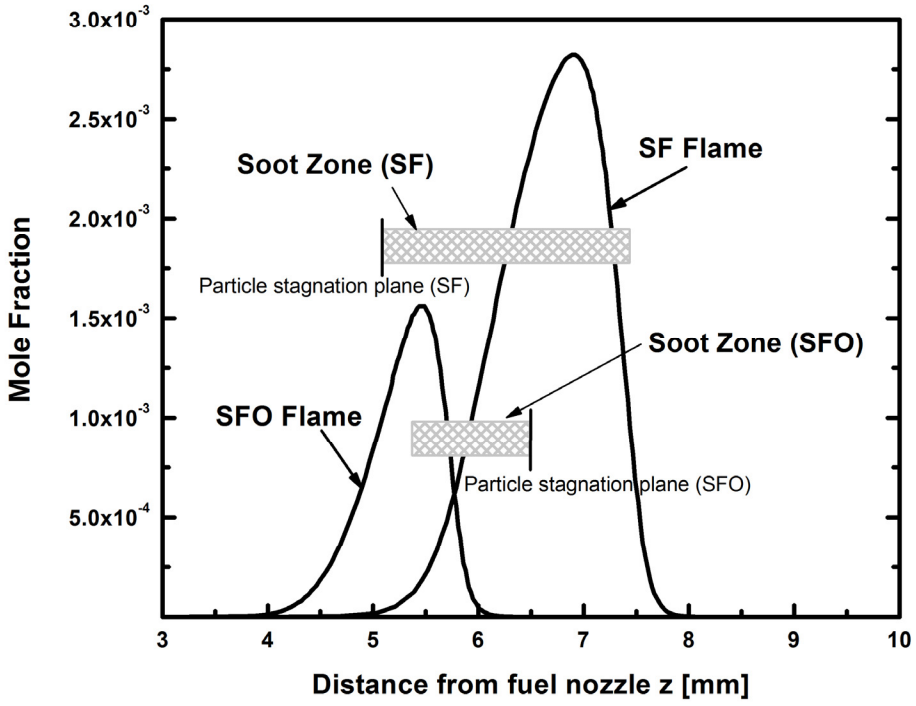

Figure 2.15. Sum of PAH concentrations for SF and SFO flames. Soot zones of both flames are approximately indicated as crossed gray boxes.

Moreover, the soot zone of the SF flame encompasses the entire high PAH concentration region. In contrast, the sooting zone of the SFO flame coincides with only a small fraction of the PAH concentration region. Therefore, PAH contribution in the SF flame is expected to be more significant than in the SFO flame.

2.4. Conclusions

In this section we investigated the particle formation characteristics of counterflow diffusion flames using a new version of the multiscale AMPI code that we implemented to describe oxygen-containing systems. A total of 158 new oxidation reactions were added to the AMPI code, and the potential for the MD module was expanded to describe systems containing C, H and O.

Soot formation characteristics in counterflow diffusion flames can be categorized into soot formation/oxidation flame (SFO) and soot formation flame (SF), based on the relative position between the flame and the particle stagnation plane. In the SFO flame the soot zone is located on the fuel side of both the particle stagnation and the maximum temperature location. The AMPI code was used to describe the inception process in both configurations, and structural

properties of the nanoparticles, including H/C ratio and aspect ratio, were computed.

The AMPI code that describes the particle inception via chemical reactions is able to reproduce very well the experimental trends observed by Kang et al. [5] for the SFO flame. We determined the particle formation zone by computing the nanoparticle growth rates at twelve locations in the flame. The growth rate was significant in the region of the C_2H_2 peak, and the main reaction sequence contributing to the growth was the HACA mechanism. Once generated particles are transported towards the higher temperature region and eventually they pass through an O and OH abundant zone to be oxidized. Oxidation regions were well predicted by the AMPI code. Oxidation reactions competed with surface growth by diverting carbon atoms (e.g., $R_i + O = R_{i-1} + CO$ and $R_i\text{-}H + O = R_{i-1} + CO + 1/2\ H_2$) and terminating radicals present on the growing structure ($R_i\text{-}H + O/OH = R_i + OH/H_2O$).

For the SF flame, we analyzed ten points using the AMPI code. For this soot formation flame, the soot zone is on the oxidizer side of the stagnation plane. The flow field in the soot zone is directed towards the fuel stream in the region between the flame and the particle stagnation plane. Particles, once generated on the fuel side of the flame, are transported away from the flame. As a result, they

cannot pass through the flame and they are not exposed to oxidizing species, such as OH and O_2.

At the beginning of the particle inception zone (Points 3 - 5 in Figure 2.9), the kinetic growth mechanism embedded in the AMPI code was able to describe particle formation because of the high concentration of C_2H_2 and high temperature (~ 2000 K). In this flame, however, we did not observe any significant chemical growth after Point 7 in Figure 2.9 where the temperature is reduced to ~ 1250K. To explain the experimental evidence showing particle formation in this region, another possible soot inception pathway needs to be considered. Agglomeration of PAH molecules and PAH coagulation on nanoparticles are likely to be responsible for the soot volume fractions in the low-temperature region of this flame.

Chapter 3

Nucleation of fullerenes as a model for examining the physical agglomeration pathway of soot

3.1. Objective

In Chapter 2, combustion regimes were identified where the formation of nanoparticles simply based on chemical reactions was not enough to justify the results by AMPI code. Following up on these results, the dependence of sizes and concentrations on the physical agglomeration of nanoparticles in a wide range of temperatures is explored in this chapter. Fullerenes have characteristics resembling the particles found in soot, but their simpler structure makes simulation more tractable. In this chapter, using MD, the clustering of the homomolecular systems of C_{60}, C_{80}, C_{180}, and C_{240} fullerenes are analyzed. The computational findings are then related to the experimental data to assess the feasibility of physical agglomeration.

3.2. Interaction between nanoparticles

The dependence of sizes and concentrations on the physical agglomeration of nanoparticles in a wide range of temperatures is explored in this chapter. To this end, MD is used to study systems composed of carbonaceous nanoparticles (fullerenes $C_{60,}$ C_{80}, C_{180}, and C_{240}) in the temperature range 500 K - 2000 K. There are two main reasons for choosing fullerenes as representatives for nanoparticles: (i) Fullerenes have a graphene-like shell structure resembling the aromatic part of nanoparticles [20, 25-27, 33], and (ii) Fullerenes of various sizes have similar morphologies with minimal steric hindrance, and it is, therefore, easy to single out the effect of particle size on coagulation rate. After presenting the methodology and the computational results in terms of agglomeration behavior as function of particle size and temperature, a discussion of the computational results for fullerene agglomeration will be followed in the context of soot formation and available experimental data.

3.3. Computational method

3.3.1. Molecular dynamic simulation

Homo-molecular systems of $C_{60,}$ C_{80}, C_{180}, and C_{240} were simulated using the canonical NVT ensemble with cubical periodic boundary conditions. The familiar form of a short-range 6-12 Lennard-Jones (LJ) potential was employed to model the non-bonded interactions between atoms. The total conformational energy between two fullerene molecules was defined as:

$$V = \sum_{ij} \left(-\frac{A}{r_{ij}^6} + \frac{B}{r_{ij}^{12}} \right) \tag{3.1}$$

where A and B are the attractive and repulsive constants and r_{ij} is the distance between two interacting atoms. The values of A and B were taken from the discrete carbon-carbon potential for C_{60} - C_{60} developed by Girifalco et al. [73, 74] (A = 15.2 eV×Å^6, and B = 34.8×10^3 eV×Å^{12}), who determined the energy of sublimation and the lattice parameters of a face-centered cubit fullerene cluster using first-, second-, and third-neighbor interactions. This potential has been used by other research groups to compute molecular properties of C_{60} and compared with experimental data for the heat of sublimation and lattice constant [73, 75]. The LJ potential cut off was set at 30 Å, and the molecules were considered to be rigid. The elimination of intramolecular potential is related to the continuum

model proposed by Girifalco [73], which simplifies the system by averaging the potential over the surfaces of the molecules. This model has been used to study the growth of fullerene clusters, interaction of C_{60} with a graphite surface and thermal expansion of C_{60} [76, 77]. The discrete atom-atom model was used in this study to facilitate the scale up of the potential to bigger fullerene molecules. The temperature was controlled using the Nosé-Hoover thermostat, which is an extended-system method for controlling the temperature of simulated system. It allows temperatures to fluctuate about an average value, and uses a damping factor to control the oscillation of this temperature. Keeping the temperature constant is very important and an inefficient thermalization may have a strong influence on the results. A recent work by Wedekind et al. [78] investigated the influence of carrier gases and thermostats on nucleation processes described with MD. The authors analyzed the efficiency of velocity rescaling, Nosé-Hoover, and a carrier gas (mimicking the experimental condition), and reported that the choice of the thermostating method does not have a significant influence on the nucleation rate, obtaining deviations of less than a factor of 1.7.

The trajectories were integrated using the Velocity Verlet method, using a time step of 0.05 ps. All calculations were performed using the DL_POLY _2.18 software package [79].

3.3.2. Initial conditions

The concentration of particles was set at 8×10^{18} cm^{-3}, with 343 molecules for the C_{60} and C_{80} systems ($35 \times 35 \times 35$ nm box) and 125 molecules for the C_{180} and C_{240} cases ($25 \times 25 \times 25$ nm box). The value of particle concentrations chosen for the simulations is higher than the numbers measured in flames. To address this point, however, in the later in this chapter, we report a detailed discussion of the effect of particle concentration on the degree of clustering of nanoparticles. The systems of molecules were initially simulated at high temperatures (~ 3500 K) to sample three initial configurations. The temperature range analyzed spans 500 K – 2000 K considering intervals of 100 K for a total of 16 temperatures.

3.3.3. Identification of clusters

An important component of this study is the definition of molecular clusters. While the simplest way is to use the distance cutoff, this criterion can become increasingly inadequate in a scenario where small clusters are constantly produced and destroyed, since the distance cutoff will overestimate the number of clusters by not distinguishing between mere collisions and agglomeration events. Therefore, in addition to this first criterion, we also compared the rotational and vibrational energies of a molecular pair to the binding potential energy, defined as

the sum of atomistic intermolecular interactions. This criterion can be expressed as follows:

$$\frac{\sum m_i}{2}\left(\frac{\sum v_i m_i}{\sum m_i}-\frac{\sum v_i m_i+\sum v_j m_j}{\sum m_i+\sum m_j}\right)^2+\frac{\sum m_j}{2}\left(\frac{\sum v_j m_j}{\sum m_j}-\frac{\sum v_i m_i+\sum v_j m_j}{\sum m_i+\sum m_j}\right)^2 < \sum_i\sum_j\left[\left(-\frac{A}{r_{ij}^{12}}\right)+\left(\frac{B}{r_{ij}^{6}}\right)\right] \quad (3.2)$$

where *i, j* are the atoms in two different molecules, m_i is the mass of atom *i*, v_i is the velocity of atom *i*, r_{ij} is the distance between atom *i* and atom *j*, and *A* and *B* are the LJ parameters used in the MD simulations. Under the assumption that both molecules are internally rigid, the left side represents the sum of the rotational and vibrational energies of a newly formed dimer. These energies are associated with the reaction coordinate of dissociation of the dimer and therefore inequality (3.2) can be a strong indicator of the stability of dimers. For a system composed of *N* molecules, *N(N-1)* molecular pairs were evaluated.

3.4. Simulation results

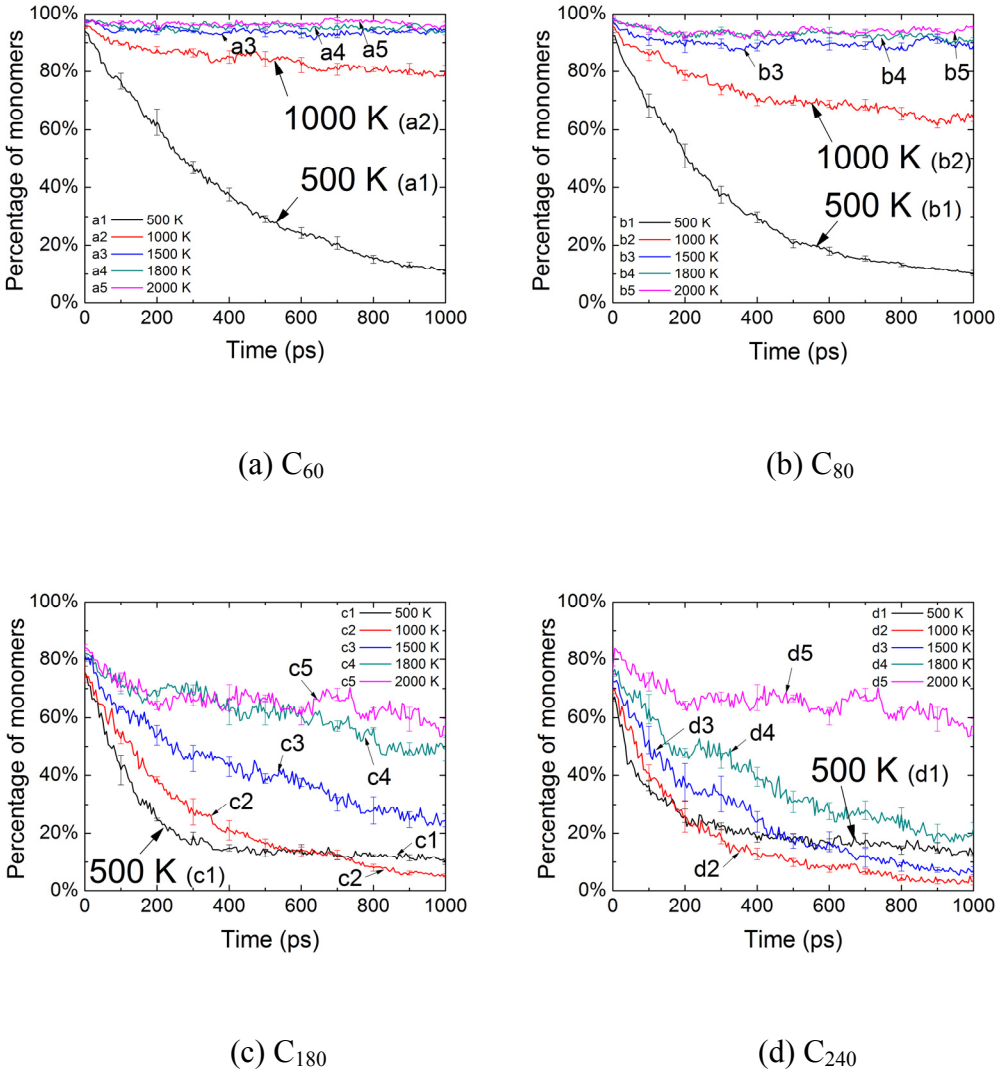

(a) C_{60} (b) C_{80}

(c) C_{180} (d) C_{240}

Figure 3.1. Percentages of C_{60}, C_{80}, C_{180}, and C_{240} fullerene molecules in the state of monomers as function of time at various temperatures.

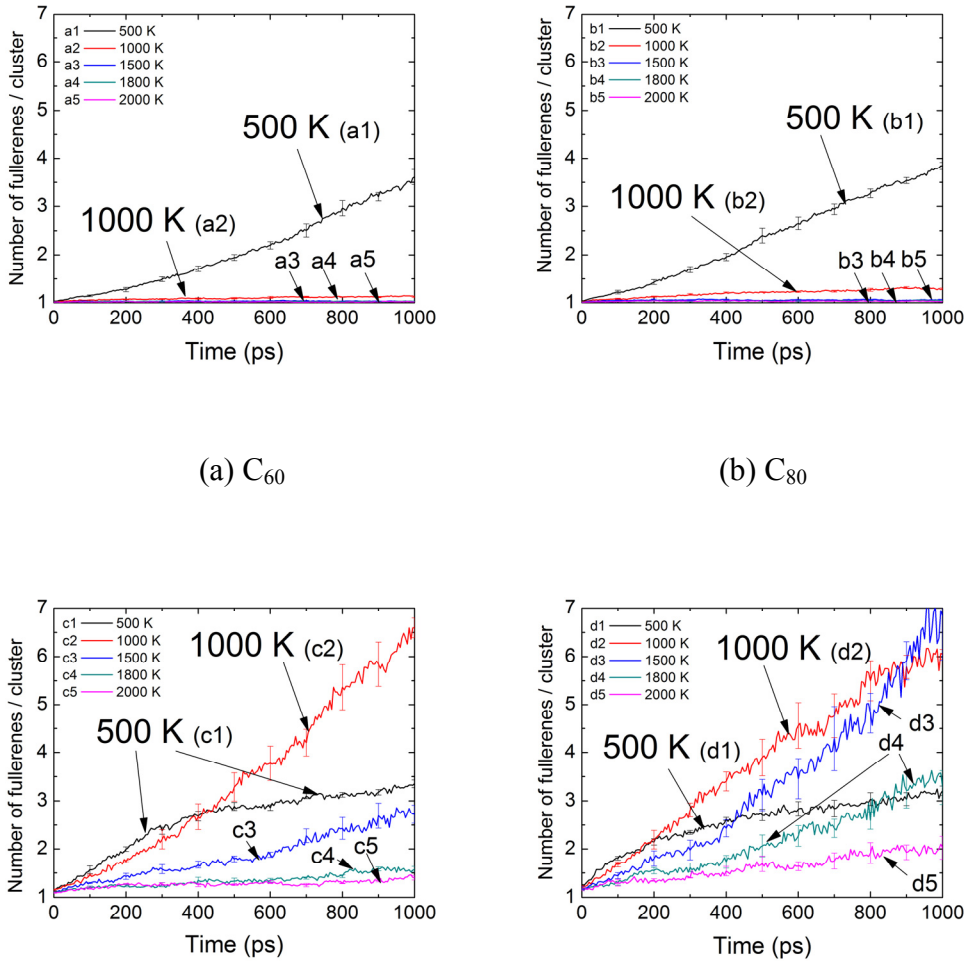

(a) C_{60} (b) C_{80}

(c) C_{180} (d) C_{240}

Figure 3.2. Mean cluster size (number of fullerenes per cluster) as a function of time at various temperatures.

Figure 3.1 and 3.2 report the percentages of fullerenes present in the system as monomers and the number of fullerenes per cluster for C_{60}, C_{80}, C_{180}, and C_{240} molecules as function of time at different temperatures. At 500 K, the systems show a significant number of "sticky" collisions and the percentage of monomers decreases by 80 % over a time interval of 1000 ps reaching an average of 3.5 - 4 fullerenes per cluster. The nucleation rate at 500 K, identified by the disappearance of monomers in the system, is the highest among the conditions investigated. However, for the systems composed of C_{180} and C_{240}, the growth of nuclei at 500 K reaches a plateau between 600 and 700 ps. This result can be explained using the Maxwell-Boltzmann molecular speed distributions of two homogeneous systems at different temperatures, as their conceptual plots are drawn in Figure 3.3 (a). At T_{low} (e.g. 500 K in our simulations), molecules with relatively high translational energies participate to the formation of nuclei since they are able to reach each other within a relative short time, and their energy levels favor binding (Figure 3.3 (b)). Since this process can be faster than the energy transfer, molecules with low translational kinetic energies require longer time to reach the adjacent species and remain in the system as monomers. In this situation, shown as T_{low} in Figure 3.3 (c), the system looks "frozen" due to the low speed of the molecules and nuclei. At higher temperatures, this effect is negligible since the binding probability is relatively low due to the high kinetic energies of the molecules. These two scenarios can explain the cross-over

behaviors reported in Figure 3.2 for the curves c1 and c2 (Figure 3.2 (c)) and d1, d2, d3 (Figure 3.2 (d)).

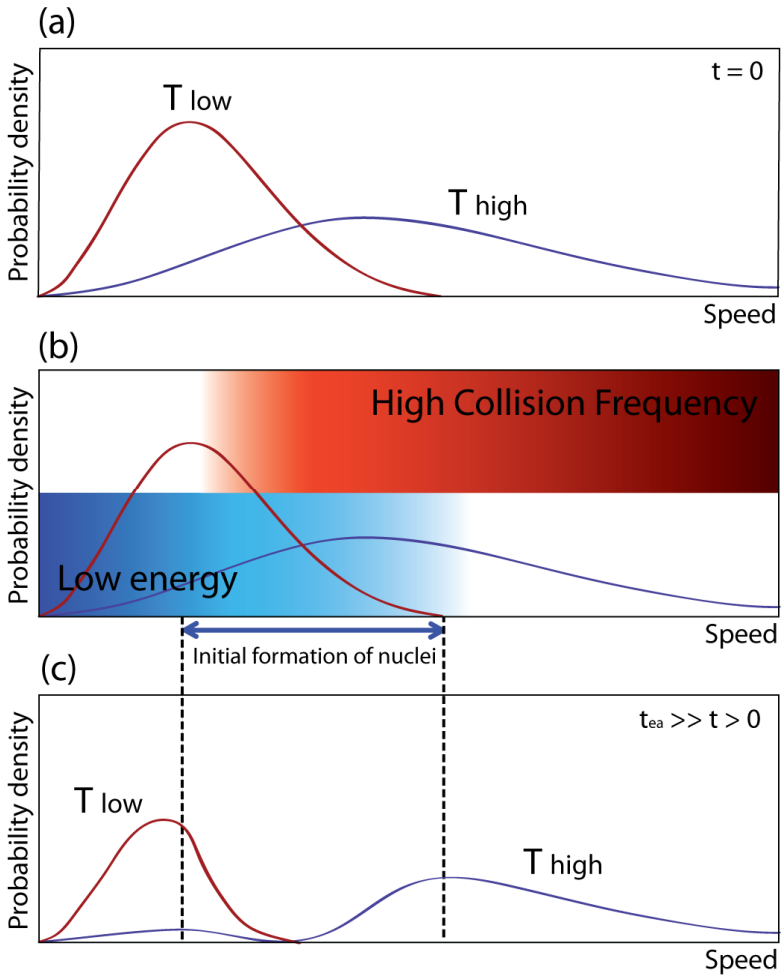

Figure 3.3. Speed probability density functions of molecules at two temperatures using the Maxwell-Boltzmann distribution. Both (a) and (b) are at t = 0 and (c) is at t immediately after few collisions between molecules. These conceptual graphs are drawn using an arbitrary scale.

At 1000 K, the four systems (C_{60}, C_{80} C_{180} and C_{240}) show different behaviors. The average size of C_{60} and C_{80} clusters does not exceed 1.35 fullerenes (Curves a2 and b2 in Figure 3.2) and the percentages of monomers in the systems are ~ 80 % for C_{60} and ~ 60% for C_{80} at the end of 1 ns simulation. C_{60} and C_{80} nuclei are constantly formed but they dissociate because of thermal fluctuations and the majority of the clusters exist as dimers. Differently, in these conditions, C_{180} and C_{240} systems still show agglomeration events. At 2000 K, only the biggest molecules - C_{240} - present some agglomeration events.

To further investigate the behavior of the systems, we computed the Lindemann index (LI) [80], that is an indicator of the molecular disorder. While the LI is typically used to identify phase transitions by observing an increase above a critical value or a departure from linearity in a global LI set [81, 82], in this study, the LI is used to investigate the agglomeration process. The formation of a nucleus lowers the LI significantly and a departure from linearity in a global set can be interpreted as the onset of nucleation process. The LI is defined as:

$$\delta_{lin} = \frac{2}{N(N-1)} \sum_{i,j(i<j)=1}^{N} \frac{\sqrt{\langle R_{ij}^2 \rangle - \langle R_{ij} \rangle^2}}{\langle R_{ij} \rangle} \qquad (3.3)$$

where R_{ij} is the distance between the centers of masses of the molecules, and the angle brackets indicate a time averaged quantity. In equilibrium conditions, the LI

does not depend on the sampling period, if the values are averaged for long time. However, in this study the Lindemann index changes over time due to the non-equilibrium conditions. Therefore, in order to compare the results obtained for the four systems at different temperatures, we averaged the values of LI between 0.75 ns - 1 ns with 5 ps intervals and the results are reported in Figure 3.4.

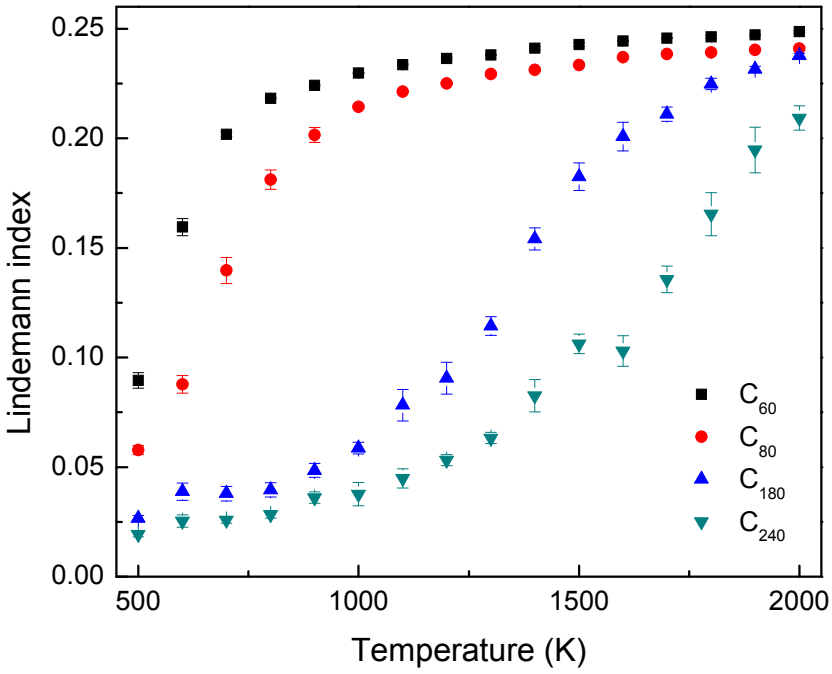

Figure 3.4. Lindemann index for the systems composed of C_{60}, C_{80}, C_{180}, and C_{240} fullerene molecules. The values are averaged over 0.25 ns time window with 5 ps sampling intervals. Temperature ranges from 500 K to 2000 K with increments of 100 K.

The system composed of C_{60} molecules shows the highest values of LI over the temperature range 500 K – 1000 K, implying that the molecules are in a thermally disordered state and the formation of nuclei is not significant. At low temperatures, the values of the LI decrease and the system shows a more ordered state with the formation of nuclei. The system composed of C_{80} molecules has an overall value of the LI slightly lower than the one obtained for the C_{60} ensemble. Large fullerenes (C_{180} and C_{240}) present significantly lower values of the LI over the entire temperature range 500 K – 2000 K when compared with the C_{60} and C_{80} systems, especially between 800 K and 1500 K. The observed behaviors suggest that the mass of the molecules is an important factor for the clustering behavior at flame temperatures and a mass value between those of C_{80} and C_{180} could represent a critical value.

Figure 3.5 reports the intermolecular potential curves for C_{60}, C_{80}, C_{180}, and C_{240} obtained from the inter-atomic LJ potential. The attractive wells become narrower and deeper as the masses of the molecules increase due to the presence of more electrons in the systems and stronger London forces. This result agrees qualitatively with the findings of Herdman and Miller [20]. At any given temperature, while the masses of the molecules contribute to the agglomeration by reducing the molecular speed and hence decreasing the collision rate, the effect of

deeper interaction potentials overcomes the effect of low collision rate due to the increased sticking probability.

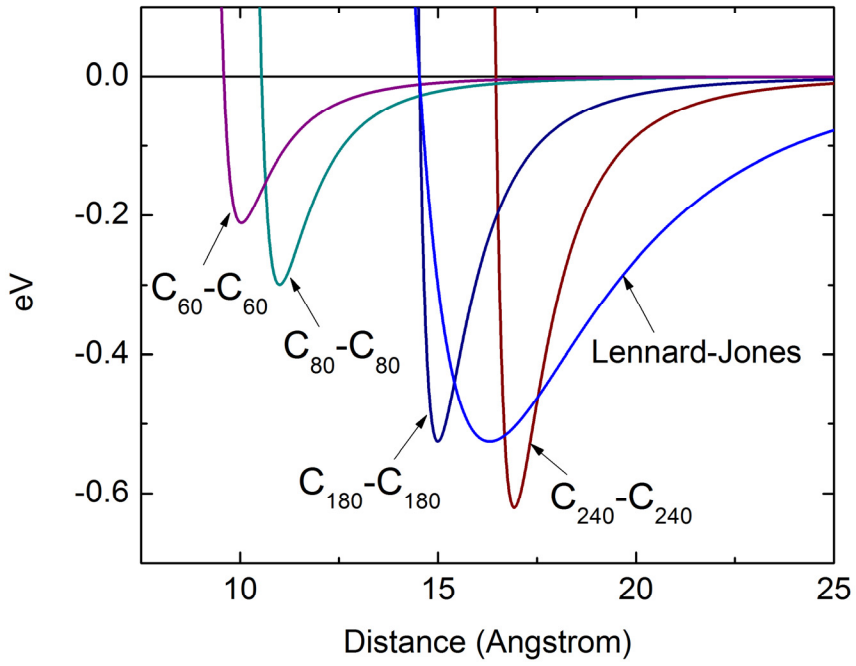

Figure 3.5. Calculated potentials for C_{60}, C_{80}, C_{180}, and C_{240} systems obtained from the inter-atomic Lennard-Jones potential between carbon atoms. The Lennard-Jones potential fitted to C_{180} fullerene's □ (depth of the potential well) and σ (distance at which the inter-particle potential is zero) is reported for comparison.

3.5. Implications for soot nucleation

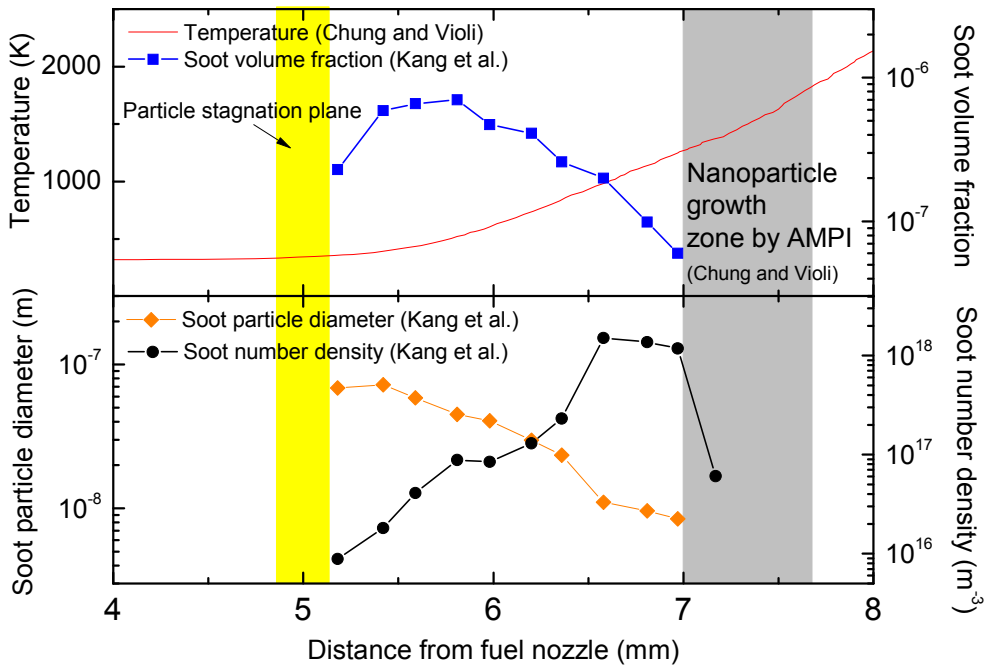

Figure 3.6. Experimental soot volume fraction, soot particle diameter, and soot number density in counter-flow diffusion flame of propane (Adapted from Kang et al. [34]). Computed temperature profile is from the previous chapter. The area with dashed lines depicts the region where the chemical growth is significant according to the results by AMPI code. Total distance between the fuel and the oxidizer nozzles is 14.2 mm and the profiles from 4 mm to 8 mm are plotted in this graph.

The goal of this study is to relate the results obtained using MD simulations to the soot formation process occurring in flame environments. In the previous section, we analyzed two different configurations of counter-flow diffusion flames to determine the effect of combustion environments on particle formation. The first configuration was a Soot-Formation-Oxidation (SFO) propane flame with the flame front located on the fuel side and the gas velocity directed toward the flame. The second one was a Soot-Formation (SF) propane flame with the gas velocity directed towards the stagnation plane and particles moving away from the flame front, which was located on the oxidizer side. The two flame conditions showed different mechanisms for the formation of particle agglomerates, and hence two interesting scenarios for the development of a model to describe the growth of nanoparticles.

For these systems, using the AMPI method, the growth rate of nanoparticles based on chemical interactions between gas phase species and particles was identified as important in SFO flames, showing very good agreement with experimental data, but the conditions depicted in SF configurations required additional growth mechanisms. In Figure 3.6 the experimental data of soot volume fraction, particle diameter and number density obtained by Kang et al. [34] for the SF configuration are shown. Although the experiments illustrates the formation of particles between 5 and 7.7 mm, the chemical growth described via

the AMPI method shows the formation of nanoparticles only between 7 – 7.7 mm (grey area in Figure 3.6). This result is mainly due to the low temperature, which limits the importance of a chemical growth process. Outside the grey area (in Figure 3.6), the soot volume fraction increases by one order of magnitude from z ~ 7 mm to z ~ 5 mm, corresponding to the stagnation plane. Since particle coagulation and agglomeration do not change the soot volume fraction, and at the same time, a growth mechanism based on chemical kinetics is not significant due to the low temperature conditions, a physical agglomeration mechanism could explain the experimental evidences, especially in the range of z = 6.5 – 7.0 mm. In order to determine the feasibility of this hypothesis, below we relate the results obtained in the previous sections using MD simulations to flame conditions. In a gas phase environment, there is a random distribution of collisions between molecules, so that the occurrence of a collision does not affect the likelihood of a subsequent collision [83]. In this case, the number of collisions over a given period of time can be preserved and it can be assumed that the time in a relatively dense system determined using MD simulations, can be associated to the time in a flame. The collision frequency of molecule *A* can be expressed as

$$Z = n_A^2 \pi (b_{coll})^2 \bar{v}_A \qquad (3.4)$$

where n_A and $\bar{v}_A$ are the concentration and average velocity of molecules A in the system, respectively, and b_{coll} is the collision diameter. To simplify the problem,

we assume that the number of collisions between particles is linearly dependent on the nucleation time. This assumption is justified by the fact that at a certain temperature, molecular energies will have similar distributions even for different density systems and, therefore, the percentage of effective collisions that can lead to cluster formation does not depend on system density. Thus, the nucleation time scale of the MD simulation can be related to the nucleation process in flames:

$$Z_{MD}/Z_{Flame} = \Delta t_{Flame}/\Delta t_{MD} \tag{3.5}$$

where Δt_{MD} is the nucleation time scale obtained from MD simulations and Δt_{Flame} is the experimental time in a flame. The collision diameters b_{coll} for the molecules analyzed with MD and the ones in the flame environment are the same in this case. Similarly, if the temperatures of the MD simulations and flame conditions are identical, the average velocities of the particles $\bar{v}_A$ are equivalent. Combining (3.4) and (3.5), we obtain:

$$\Delta t_{Flame} \cong \Delta t_{MD} \times n_{MD}^2/n_{Flame}^2 \tag{3.6}$$

This expression correlates Δt_{Flame} with the MD simulations time and particle concentrations.

In order to validate this correlation, additional MD simulations were carried out varying the density of the system. Twelve different densities were sampled

and, for each case, the simulation times when the percentage of monomers decreases below 75 % were sampled and compared with theoretical values obtained using (3.6). Figure 3.7 reports the relationship between density and Δt, showing very good agreement between the values obtained using MD simulation and prediction obtained with (3.6). Therefore, the correlation described in (3.6) can be justified for this analysis.

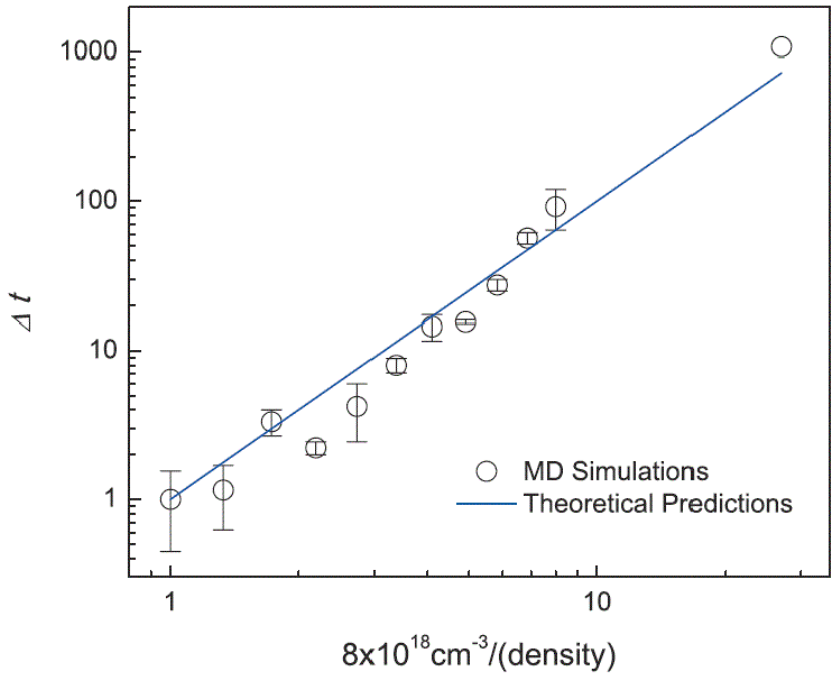

Figure 3.7. Comparison between MD simulation results and the prediction by Eq. (3.6). The circles display MD simulation time when the percentage of monomer molecules decreases below 75 % and the blue line indicates the theoretical prediction. The uncertainties are determined by performing three different simulations for the same density condition.

To assess the relative importance of a chemical mechanism versus a physical process for the formation of clusters, $t_{1.5}$ is defined as the simulation time when the average size of a cluster reaches 1.5 fullerenes. For T > 1000 K the cluster

sizes of the systems composed of C_{60} and C_{80} do not reach 1.5 over the MD simulation time, as reported in Figure 3.8. Differently, for the C_{180} and C_{240} systems, $t_{1.5}$ is on the order of 10^1 or 10^2 ps for the entire temperature range considered. However, as reported in Figure 3.6, the temperature of the grey area exceeds 1300 K and in these conditions, the time scale for the chemical growth calculated using the AMPI code, was between 0.1 ms and 1 ms [33]. For T > 1300K MD simulations predict $t_{1.5}$ on the order of 10^2 ps, even for systems composed of C_{240}.The most important difference between the conditions analyzed by MD simulations and flame conditions is the difference in particle density. Using Equation 3.6, if Δt_{MD} is 10^2 ps and the system density is $n_{MD} = 8 \times 10^{18}$ cm^{-3}, the Δt_{Flame} is 10 ms when $n_{Flame} = 8 \times 10^{14}$ cm^{-3} or Δt_{Flame} is 0.1 ms if $n_{Flame} = 8 \times 10^{15}$ cm^{-3}. Both cases, however, are not practical to describe nanoparticle growth in these flame conditions. In the first scenario, 10 ms is too slow to represent a viable growth mechanism when compared with the chemical growth rate calculated by the AMPI method, which is two orders of magnitude lower. In the second case, the number density of $n_{Flame} = 8 \times 10^{15}$ cm^{-3} is unrealistically high, when considering the maximum carbon atom number density that can be supplied by a fuel. Therefore, as reported in the previous chapter, a chemical mechanism for the cluster growth is expected to be the dominant pathway for the soot nucleation process in this region.

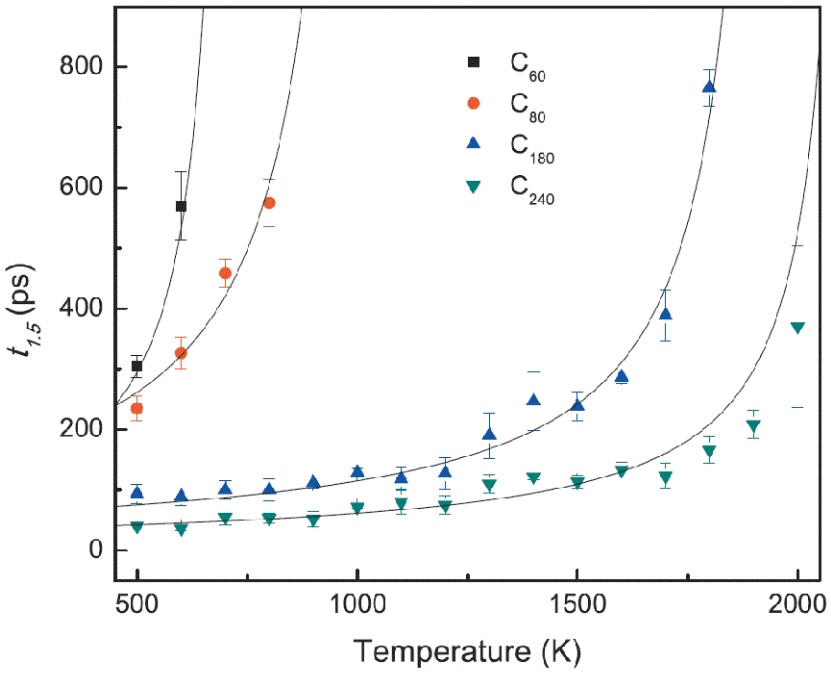

Figure 3.8. Values of $t_{1.5}$, defined as the simulation time for the mean size of the clusters to reach 1.5 fullerenes for the C_{60}, C_{80}, C_{180}, and C_{240} systems of fullerenes. The trend line is also shown for the each system.

This conclusion changes when the particles move out of the grey area toward the stagnation plane. The temperature in this region ranges from 400 K to 1300 K (Figure 3.6) and $t_{1.5}$ of C_{240} is on the order of 10^1 ps. If $t_{1.5}$ is used in (3.6), we obtain a $O(\Delta t) = 1$ ms when the density of $n_{Flame} = 8 \times 10^{14}$ cm^{-3}, that is comparable with the time scale for chemical growth in the grey region. While a

density value of 8×10^{14} cm^{-3} can be considered very high in view of the current experimental predictions [84], it can still be realistic. To show this, we simplify the problem by calculating the total carbon atom density of propane. If the mole fraction of the fuel in a system is 0.5, which is the case for the SF flame shown in Figure 3.6, the available carbon number density at T = 1000 K and P = 1 atm is 1.1×10^{19} cm^{-3}. Since the carbon atom number density of C_{240} is 1.9×10^{17} cm^{-3}, if its molecular density is $n_{Flame} = 8 \times 10^{14}$ cm^{-3}, then only 1.7 % of the entire carbon atom content contributes to the formation of C_{240}. This value is realistic. Santoro et al. [85] reported that in some conditions the percentage of fuel carbon converted to soot particles can reach 10 ~ 15 % in sooting zones under atmospheric pressure and Flower and Bowman [86, 87] demonstrated that at high pressure (~ 10 atm) over 50 % of the fuel carbon can be converted to soot particles. Therefore, a density value of 8×10^{14} cm^{-3} may be achieved for nanoparticles in flames, because their sizes are much smaller than soot particles.

When this last result is combined with the previous AMPI analysis, we can conclude that the nucleation process can be active over the entire soot zone, from the high temperature oxidation side to the low temperature stagnation plane, and flame conditions determine the relative importance of a purely chemical growth mechanism, a physical-clustering process or their combination. These results can

also explain the experimental increase in the soot volume fraction in the low temperature region starting from c.a. z = 7 mm toward the stagnation plane.

A second set of experimental studies reporting data on nanoparticle size distributions and population is represented by *in situ* methods, such as UV-visible light scattering, fluorescence, and extinction measurements. [84, 88] When the wavelength of the light λ is much larger than the size of particles, the absorption and scattering can be expressed as:

$$K_{obs} = -\frac{6\pi}{\lambda}\,\mathrm{Im}\left\{\frac{\tilde{m}^2-1}{\tilde{m}^2+2}\right\} f_v \qquad (3.7)$$

$$Q_{vv} = \frac{3\pi^3}{2\lambda^4}\left|\frac{\tilde{m}^2-1}{\tilde{m}^2+2}\right|^2 f_v d^3 \qquad (3.8)$$

where $\tilde{m}$ is a complex index of refraction, f_v is the volume fraction, and d is the mean diameter. As the measured light scattering is the sum of scattering due to the gas-phase products of combustion as well as of the high molecular mass structures and soot particles, the excess scattering due to gas-phase compounds was estimated and subtracted from the experimental scattering values. For a premixed fuel rich laminar flame with a C/O ratio of 0.51, which is below the sooting threshold, Minutolo et al. [84] reported the average size and the number density of the particles as *ca.* 2.3 nm and 8×10^{12} cm^{-3}, respectively. For a C/O ratio of 0.77, which corresponds to sooting environments, the number density of particles was

around 7×10^{13} cm^{-3} when the average size of the particles was *ca.* 2.5 nm. In these conditions, the experimental Smoluchowski coagulation rate,

$$k = -\frac{1}{N^2}\frac{dN}{dt} \qquad (3.9)$$

where N is the number concentration, is $k \approx 5 \times 10^{-13}$ cm^3/s. [84] To analyze these experiments, we determined the Smoluchowski coagulation rate from MD simulations of a system composed of C_{240} that has mass and size similar to the nanoparticles experimentally identified by Minutolo et al.[23] Figure 3.9 shows the Smoluchowski coagulation rate versus the number density at different temperatures obtained from MD simulations. The Smoluchowski coagulation rate is linearly related to the number density because the MD time scale is quadratically dependent on the number density of the MD simulation. For the experimental number density of 7×10^{13} cm^{-3}, the Smoluchowski coagulation rates are 1.2×10^{-14} cm^3/s, 9.4×10^{-15} cm^3/s, and 5.5×10^{-15} cm^3/s for T = 500 K, 1000 K, and 1500 K, respectively. These values are one order of magnitude lower than the experimental rate of 5×10^{-13} cm^3/s. In our simulations, the experimental value of 5×10^{-13} cm^3/s can be reached only if the number density is on the order of 10^{15} cm^{-3}. Interestingly, this value is very similar to the one proposed for the SF flame.

From these analyses, we can infer that, at least for some flame conditions, the number density of nanoparticles should be on the order of 10^{15} cm^{-3} to explain the physical agglomeration process. As mentioned above, however, the value of density proposed in this study is quite high when compared to currently available experimental data. One possible explanation could be the uniqueness of the refractive index $\tilde{m}$ assigned to all the nanoparticles in the flame environment, since this value is a critical factor in determining results from UV optical diagnostics. Future work is necessary to address this point and determine the role of physical agglomeration process.

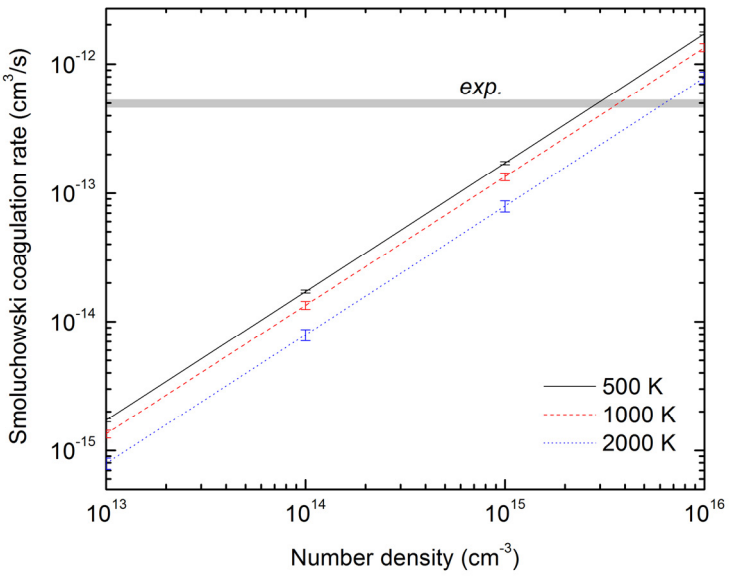

Figure 3.9. Smoluchowski coagulation rates for the system composed of C_{240} as a function of number density at different temperatures.

3.6. Conclusions

In this section we investigated the physical agglomeration process of carbonaceous nanoparticles in the temperature range 500 K - 2000 K using MD simulations with the overall goal to determine the importance of the process in different flame conditions. Four systems, composed of C_{60}, C_{80}, C_{180} and C_{240} fullerenes, were considered and the simulations were carried out over the temperature range 500 K – 2000 K.

For temperatures lower than 1000K, the four systems show similar behaviors in terms of clustering. At higher temperatures, however, molecular clusters are formed only with molecular sizes of C_{180} and C_{240}.

When the computational results are related to flame conditions, agglomeration of small particles, such as C_{60} and C_{80}, cannot justify the experimental values of nanoparticle growth, except for temperatures lower than 1000 K. On the other side, systems composed of bigger nanoparticles (C_{180} and C_{240}) showed considerable clustering between 500 K and 2000 K during the first 1 ns of simulation time.

The results obtained using the Lindemann Index (LI), an indicator of the molecular disorder, show that large fullerenes (C_{180} and C_{240}) present significantly lower values of the LI when compared with the C_{60} and C_{80} systems, especially

between 800 K and 1500 K, and this suggests that a mass value between those of C_{80} and C_{180} can be critical for the agglomeration behavior at flame temperatures.

The MD results obtained in this study help to complement the results of previous chapter on chemical growth of particles using the AMPI model in counterflow diffusion flame by adding feasibility to an alternative route in the low temperature region. The computational results were also correlated with the experimental data from UV-visible light scattering and absorption experiments [84, 88]. The analysis reveals that the number density of nanoparticles in a sooting flame could be ca. 10^{15} cm^{-3} for particle sizes as large as C_{240} to undergo a significant physical agglomeration process. While this value of particle density is high compared with available experimental results, the percentage of fuel carbon conversion to soot particles is indeed reasonable, thus showing the feasibility of this assumption. Fullerenes are expected to present minimal steric hindrance compare to non-fullerenes because their unique morphologies. Therefore, the results in this chapter show that particle nucleation is the result of physical agglomeration and chemical growth pathways, and the combustion conditions determine the relative importance of these two routes.

Chapter 4

Dimerization of polycyclic aromatic hydrocarbon molecules and their collision efficiency

4.1. Objective

The dimerization of polycyclic aromatic hydrocarbons (PAHs) is regarded as an important process in soot formation. In particular, pyrene dimerization is widely used as nucleation step in many soot modeling studies. However, recent findings indicate that the dimerization of pyrene may not be a key step in soot formation. In this chapter, we introduce a theoretical study to investigate the role of various PAHs, including pyrene, using molecular dynamics (MD) simulations. The results from this study can be utilized to obtain accurate nucleation rates for soot models.

4.2. Pyrene dimerization

Pyrene dimerization as a practical soot nucleation step has been widely adopted in many current soot modeling studies. [5, 8, 28-30] However, there is still no definitive experimental data to the dimerization of pyrene as a soot nucleation step [20]. Moreover, recent studies indicate that pyrene dimerization might not be an important step in soot formation process. For example, as stated in Chapter 1, Chung and Violi [31] observed pyrene dimers or trimers using MD simulations and concluded that they are not stable enough to grow into soot nuclei in high temperature conditions. Sabbah et al.[5] also presented experimental measurements and theoretical study on the kinetics of pyrene dimerization. They demonstrated that dissociation of pyrene dimers is highly favored at high temperature and concluded that the dimerization of pyrene may not be a key nucleation step.

Therefore, the pyrene dimerization model for soot nucleation needs to be carefully re-evaluated. In this study, we do that by calculating accurate rates for pyrene dimerization so that its role in soot formation can be evaluated. In addition, we also investigate the dimerizations of larger PAH molecules with different sizes and morphologies to compare their roles to that of pyrene dimerization. Such comparisons can help to identify alternate soot nucleation pathways that involve PAH molecules larger than pyrene.

In particular, we focus our study on the collision efficiency of PAH dimerization, since it is a dominating parameter that determines nucleation rates. The relation between collision efficiency and the nucleation rate is discussed in detail in the following methodology section. Recently, Raj et al.[89] also studied PAH collision efficiency and presented it as an empirical function of molecular mass and diameter. While temperature is a major factor that influences collision efficiency, the empirical relation presented by the authors does not include the effect of temperature. Also, the effect of the morphology of PAH molecules on collision efficiency is not accounted for in this empirical expression. In order to overcome these issues, in this paper, we present temperature dependent dimerization collision efficiency calculated using MD simulations. In addition to homogeneous PAH molecules, the dimerization of different PAH molecules is discussed. The dimerization collision efficiency obtained in this study can be readily adopted by existing soot models, and a possible route will be discussed in our next study.

4.3. Nucleation rate

We can define the nucleation rate through dimerization in terms of the collision frequency and the collision efficiency of two molecules. The nucleation

rate can be expressed as [90]:

$$r_{nuc} = \frac{1}{2N_{avo}} \sum_{i=1}^{\infty} \sum_{j=1}^{\infty} \beta_{ij} N_i N_j \tag{4.1}$$

where r_{nuc} is the nucleation rate, N_{avo} is Avogadro's number, and N_i and N_j are the number density of *i* and *j* species. Assuming a free-molecular regime, β_{ij} is:

$$\beta_{ij} = \beta \times \sigma_{ij} \sqrt{\frac{8k_B T}{\pi \mu_{ij}}} \tag{4.2}$$

where β is the collision efficiency, σ_{ij} is the reaction cross section between species *i* and *j*, and μ_{ij} is the reduced mass of species *i* and *j*. It should also be mentioned that β is not a constant, but highly dependent on temperature because the energy level of two colliding molecules is one of the important factors that determines β.

If the colliding species are the same, the nucleation rate can be expressed as:

$$r_{nuc} = \beta \times N_{avo} d_{PAH}^2 \sqrt{\frac{4\pi k_B T}{m_{PAH}}} \left[PAH \right]^2 \tag{4.3}$$

where d_{PAH} is the diameter of the PAH molecule, m_{PAH} is the mass of the PAH molecule, and $[PAH]$ is the PAH concentration. While all these parameters can be obtained from the reactants and flame conditions, determining the collision efficiency (β) is not straight forward.

4.4. Computational method

4.4.1. MD simulations

To this end we use all-atom MD simulations in order to investigate the dimerization collision efficiency of PAH molecules. In this model, each atom, including hydrogen, is subjected to both non-bonded and bonded interactions. Non-bonded interactions contain a repulsion term, a dispersion term, and a Coulomb term. The repulsive and dispersion terms are combined in the Lennard-Jones (LJ) potential form and all charged atoms interact with each other through the Coulomb term. The non-bonded potential between two atoms is expressed as follows:

$$V_{nonbonded}\left(r_{ij}\right) = 4\varepsilon_{ij}\left(\left(\frac{\sigma_{ij}}{r_{ij}}\right)^{12} - \left(\frac{\sigma_{ij}}{r_{ij}}\right)^{6}\right) + f\frac{q_i q_j}{r_{ij}} \qquad (4.5)$$

where the electric conversion factor $f = 1/4\pi\varepsilon_0 = 138.935485(9)$ kJ mol^{-1} nm e^{-2}. The parameter set used for the LJ potential was originally developed by B. W. van de Waal [91] and used by J. H. Miller and coworkers in their studies on PAH dimerization and soot nucleation process [20, 26]. The effective atomistic charges for the compounds analyzed in our studies were obtained from electronic structure calculations using the Gaussian 09 program [92]. The geometries for all species were optimized by a Becke's three-parameter hybrid method [93] used in conjunction with the correlation functional of Lee et al. [94, 95] (designated B3LYP) with the 6-31G** basis set. Atomistic charges were also obtained using the same level of theory and basis set. For the bonded terms, OPLSAA parameters [96, 97] were applied for the following expressions:

$$V_{bond}\left(r_{ij}\right) = \frac{1}{2}k_{ij}^{b}\left(r_{ij} - b_{ij}\right) \tag{4.6}$$

$$V_{angle}\left(\theta_{ijk}\right) = \frac{1}{2}k_{ijk}^{\theta}\left(\theta_{ijk} - \theta_{ijk}^{0}\right)^{2} \tag{4.7}$$

$$V_{dihedral}\left(\phi_{ijkl}\right) = \sum_{n=0}^{5} C_n \left(\cos\left(\psi\right)\right)^{n} \tag{4.8}$$

For all our simulations, we employed the canonical (NVT) ensemble. A constant temperature is attained using the Nosé-Hoover thermostating method [98]

with a time constant of 0.03 ps. All calculations were performed using the Gromacs 4.0.7 program [99].

4.4.2. Identification of dimers

The MD results are post-processed to obtain collision efficiencies of dimerization. An important component of this study is to accurately identify collision and dimerization events. The MD results are post-processed using the criteria that define collision and dimerization events to obtain collision efficiency of dimerization. While a solely distance based collision criterion can detect the collision events, it is unable to distinguish between mere collisions and effective collisions that lead to dimerization. Therefore, we use an additional lifetime cutoff that distinguishes between collision types. While we selected 1.5σ (σ being the molecular dispersion Lennard-Jones coefficient) as the distance cutoff, choosing a lifetime cutoff value is not straightforward. To identify an optimal lifetime value, collision efficiencies based on cutoff values from 2 ps to 20 ps, with 1 ps interval, were calculated for four different planar PAH molecules and the results are shown in Figure 4.1. All plots show the collision efficiency values decay rapidly with low cutoff values. This is due to inadequate distinction between mere collision events and dimerization events. In contrast, the graphs become stable for lifetime

cutoffs beyond 10 ps, because the cutoff starts to differentiate between mere collision events and dimerization events effectively. To be more conservative, we use 20 ps as a lifetime cutoff for this study.

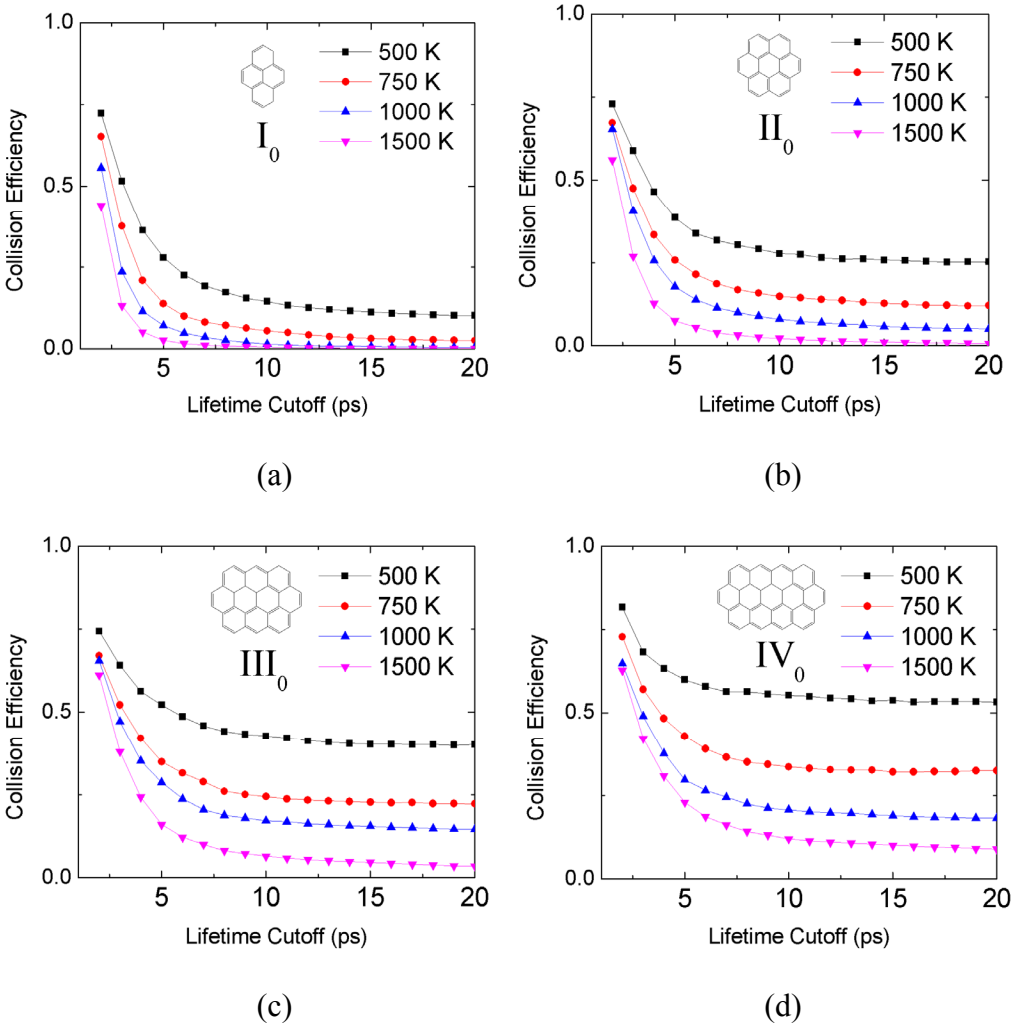

Figure 4.1. Dimerization collision efficiencies of PAHs as a function of the dimerization lifetime cutoff.

4.5. Collision efficiency

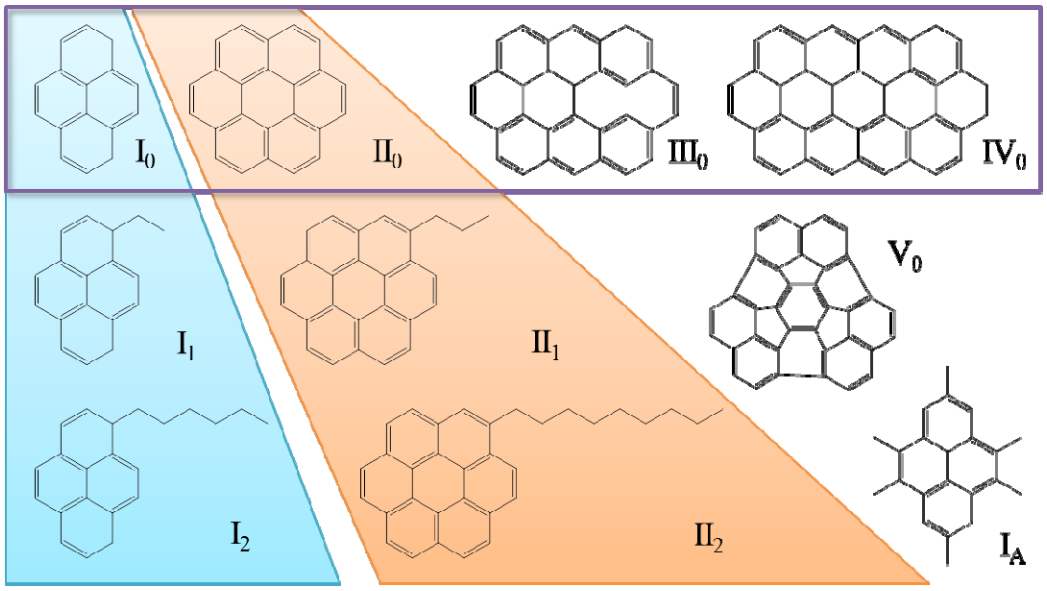

Figure 4.2. Molecules studied in this chapter.

The calculation of nucleation rate, based on (4.4), requires the evaluation of collision efficiency, which depends on various parameters, such as temperature, molecular size, and molecular morphology. In order to identify the effect of temperature on collision efficiency, various systems are simulated at four temperatures (500 K, 750 K, 1000 K, and 1500 K) using MD simulations. All molecules studied in this study are shown in Figure 4.2. We designate the peri-condensed aromatic hydrocarbon (PCAH) molecules, which are aromatic-carbon-

only molecules, as I_0, II_0, III_0, IV_0 and V_0. While I_0, II_0, III_0, IV_0 are flat PAH molecules, V_0 has a curved PAH surface. The molecules with aliphatic chains attached to I_0 are named as I_1, I_2, I_A and those with aliphatic chains attached to II_0 are designated as II_1, II_2. PAH molecules with and without an additional aliphatic chain to evaluate the influence of molecular structure on collision efficiency. In each case, we simulate a system that consists of 1000 molecules for 1 ns, in order to obtain statistically averaged dimerization collision efficiencies.

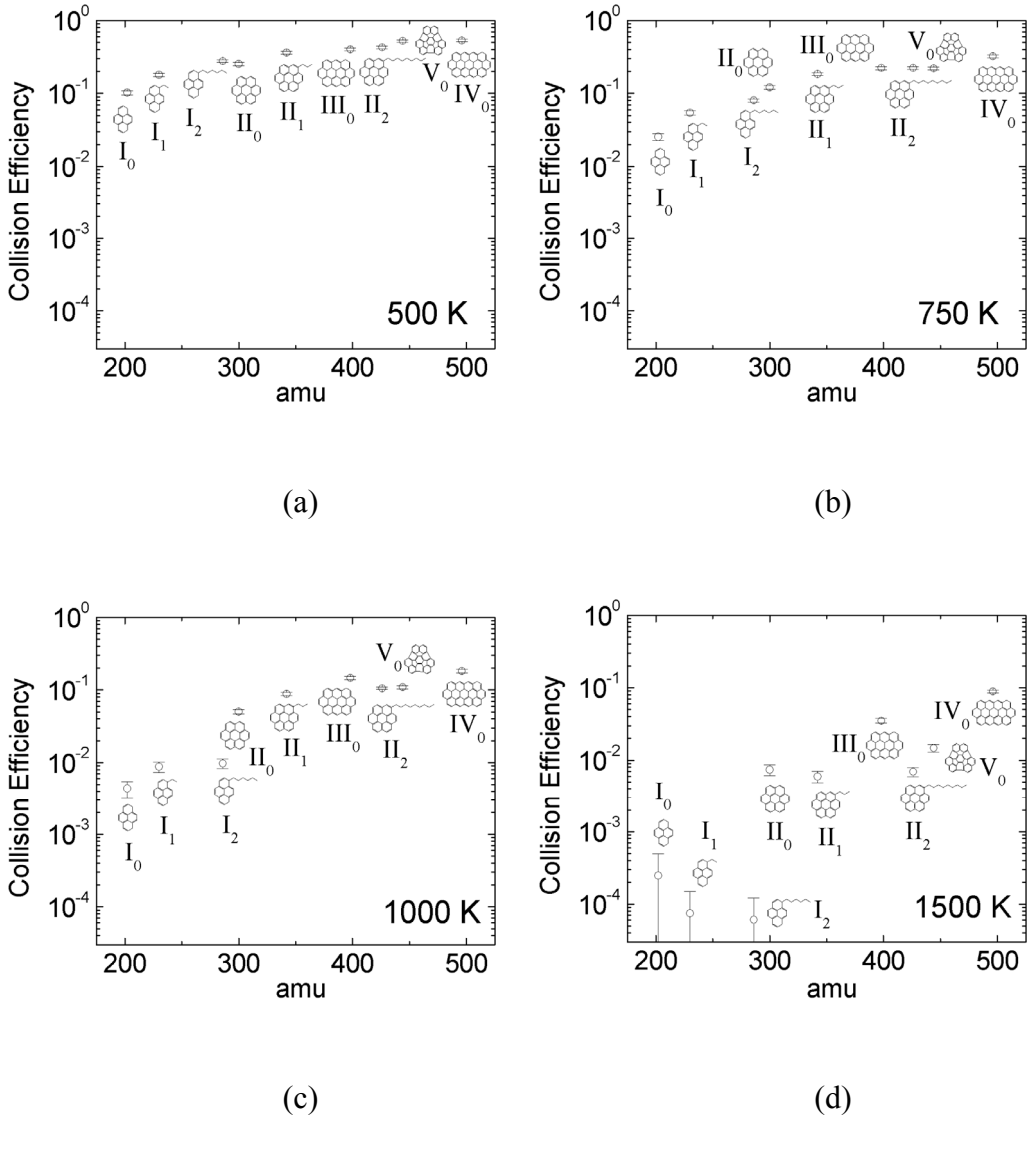

Figure 4.3. Collision efficiency for four different temperature conditions - (a) 500 K, (b) 750 K, (c) 1000 K, and (d) 1500 K.

Figure 4.3 shows the collision efficiency values at 500 K, 750 K, 1000 K, and 1500 K. As shown in this figure, temperature is the parameter that strongly contributes to the collision efficiency. Molecular collisions have the highest collision efficiency at 500 K, and this decreases as temperature increases. The molecular mass is another important factor that determines collision efficiency. In general, it is expected that, at the same temperature conditions, the collision efficiency values correlate with the molecular mass, while there are some deviations from this trend caused by other factors, which will be discussed below.

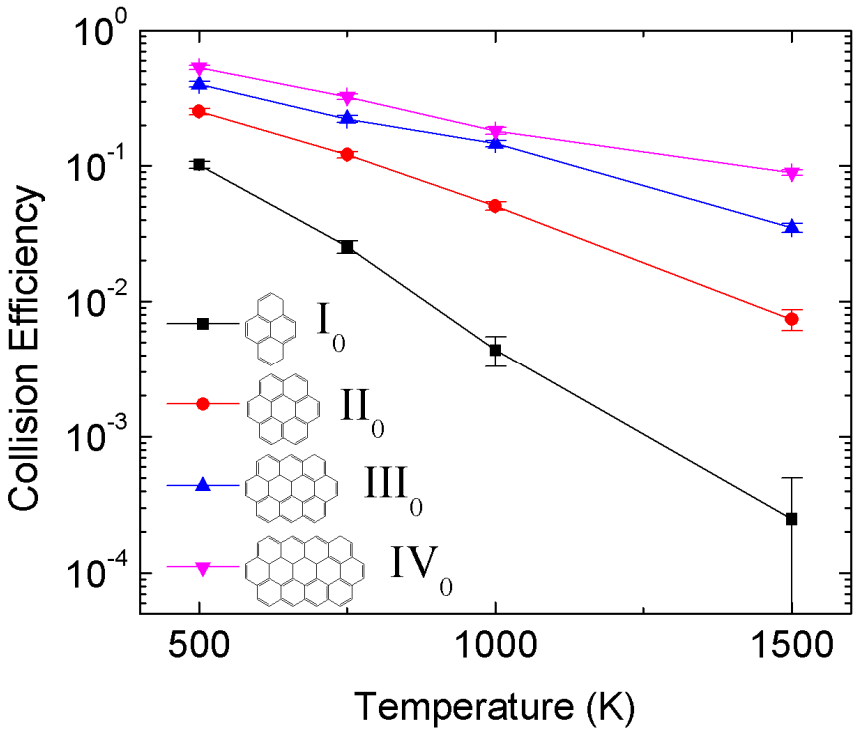

Figure 4.4. Collision efficiency for four peri-condensed aromatic hydrocarbon (PCAH) molecules.

4.5.1. Flat PAH molecules

As shown in Figure 4.4, the effects of molecular size and temperature are more evident when the collision efficiency values for four flat PAH molecules (I_0, II_0, III_0, and IV_0) are plotted separately. The plot shows consistently the influence of two major factors, temperature and molecular mass. In addition, it is important

to note that there is a difference in the magnitude of variation depending on molecular mass in this temperature range. For example, in the case of IV_0, the collision efficiency drops from 0.53 at 500 K to 0.089 at 1500 K, so the variation is within an order of magnitude. In contrast, in the case of I_0, the collision efficiency drops from 0.10 at 500 K to 0.00025 at 1500 K, which is an almost three order of magnitude drop in collision efficiency. Since the temperature of the soot zone is usually within this temperature range, the pyrene (I_0) dimerization route as a soot nucleation process is expected to be highly dependent on flame conditions such as the temperature of soot nucleation zone, while the IV_0 dimerization route is expected to be more consistent at various temperature conditions.

Figure 4.5 shows a surface fit for the collision efficiency values of I_0, II_0, III_0, and IV_0 using the following functional form:

$$\beta(\mathrm{T},\mathrm{AR}) = \exp\left(\mathrm{p00} + \mathrm{p10}\times\mathrm{AR} + \mathrm{p20}\times\mathrm{T}^2 + \mathrm{p11}\times\mathrm{T}\times\mathrm{AR} + \mathrm{p02}\times\mathrm{AR}^2 + \mathrm{p30}\times\mathrm{T}^3 + \mathrm{p21}\times\mathrm{T}^2\times\mathrm{AR} + \mathrm{p12}\times\mathrm{T}\times\mathrm{AR}^2 + \mathrm{p03}\times\mathrm{AR}^3\right) \quad (4.9)$$

where T is temperature (K), AR the number of aromatic rings, and p00, p10, p20, p11, p02, p30, p21, p12, and p03 are fitting coefficients. The coefficient values used to fit are listed in Table 4.1.

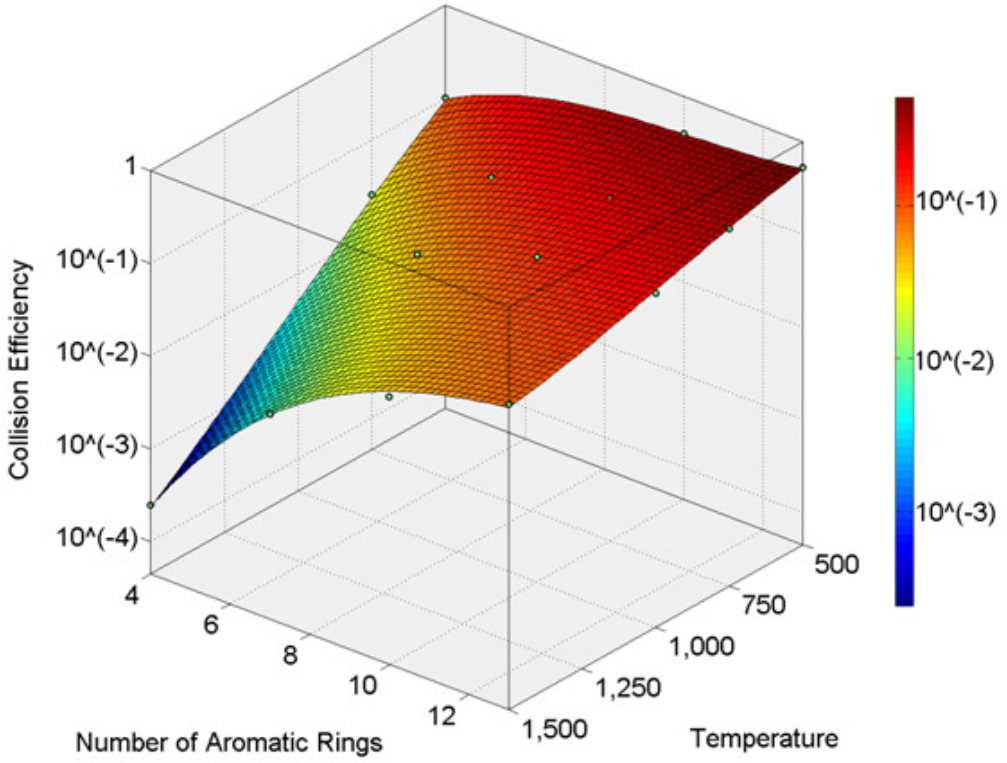

Figure 4.5. Collision efficiency for four peri-condensed aromatic hydrocarbon (PCAH) molecules (Points) and the corresponding surface fit using (4.9) and Table 4.1.

Table 4.1. Fitting coefficients for (4.9).

p00	-1.864
p10	-0.006943
p01	0.7441
p20	-3.56E-06
p11	0.001282
p02	-0.1041
p30	1.07E-09
p21	3.71E-08
p12	-5.24E-05
p03	0.004242

Recently, Raj et al.[89] modeled the PAH collision efficiency as an empirical function of molecular mass and diameter as shown below:

$$C_E = \frac{1}{1+\exp\left(-\left(A\times\frac{D_{\min}^3}{M_{\min}}\right)+\left(\frac{M_{\min}}{B}\right)^6 - C\right)} \qquad (4.10)$$

Three fitting parameters A, B, and C were obtained by matching the shape of computed mass spectra to experimental mass spectra of a laminar premixed

ethylene flame. The collision efficiency values predicted by (4.10) are 0.0072 for I_0, 0.014 for II_0, 0.087 for III_0 and 0.11 for IV_0. These values are lower than those shown in Figure 4.4 at 1000 K, and higher than the values shown in Figure 4.4 at 1500 K. For I_0, the collision efficiency calculated using (4.10) is in between the values at 750 K and 1000 K in Figure 4.4. Hence, (4.10) over-predicts the collision efficiency of small monomers such as I_0 compared to larger monomers. As stated in the introduction section, it is important to note that (4.10) does not depend on temperature, while temperature is a major parameter that influences collision efficiency. This is because isolating the temperature effect from the mass spectra is impossible, since the mass spectra are influenced by the flame temperature variation over the height above the burner, not just a temperature where it is measured.

4.5.2. The presence of an aliphatic chain

While temperature and molecular mass are the two most important factors, molecular morphological effects such as the presence of an aliphatic chain or curvature in the PAH surface also influence collision efficiency. Figure 4.6 (a) shows I_0 with its corresponding structure with an aliphatic chain attachment – I_1, and I_2. The collision efficiency of II_0, which has a molecular mass (300 amu)

comparable to that of I_2 (286 amu) is also plotted for comparison. Similarly, Figure 4.6 (b) presents the collision efficiencies for II_0 with its corresponding structures with aliphatic chain attachments – II_1, and II_2, and the collision efficiency for III_0 is shown for comparison. The addition of an aliphatic chain to these PAH molecules produces different dimerization trends depending on the temperature. We suggest two possible explanations that may contribute to these trends: the addition of low frequency internal vibrational modes and the steric hindrance. At 1500 K, the collision efficiency values of I_1, I_2, II_1, and II_2 are lower than those of corresponding PAH molecules I_0 and II_0, and these results demonstrate that the addition of an aliphatic chain lowers collision efficiency. This is observed despite the fact that the addition of an aliphatic chain increases the total mass of the molecules, which should help increasing the collision efficiency. This effect is likely due to the steric hindrance introduced by an aliphatic chain, which limits the range of effective collision angles that can accommodate PAH stacking. However, the trend becomes opposite when temperature decreases. At lower temperatures such as 500 K, I_1, I_2, II_1, and II_2 have higher collision efficiency than the corresponding I_0 and II_0 molecules. I_2 has an even higher collision efficiency value than II_0, even though II_0 is heavier than I_2. One possible explanation for this phenomenon is the addition of low frequency internal vibrational modes introduced by aliphatic chains. In order to investigate this, the internal vibrational modes are calculated using Gaussian 09 program [92]

with B3LYP/6-31G**. Table 4.2 shows the 10 lowest frequency modes obtained for each molecule. While an additional aliphatic chain with N atoms introduces 3N internal vibrational modes, part of them significantly lower the lowest vibrational frequency of the molecule compared to their corresponding aromatic-only PCAH molecules. These low vibrational modes may facilitate the temporal accommodation of kinetic energy during collisions at relatively low temperature conditions, since the frequencies of translational and rotational motions are nearly zero [100]. In Figure 4.7, collision efficiencies of PAH molecule I_A (286 amu) with six single-carbon aliphatic branches is also compared to that of other molecules with similar mass. This molecule also generates low frequency vibrational modes similar to I_2 (286 amu) as shown in Table 4.2, and it has similar collision efficiency with I_2 at 500 K, as expected. However, it has higher collision efficiency than I_2 at higher temperatures, possibly because the six short aliphatic chains of I_A may present less steric hindrance than the long aliphatic chain of I_2.

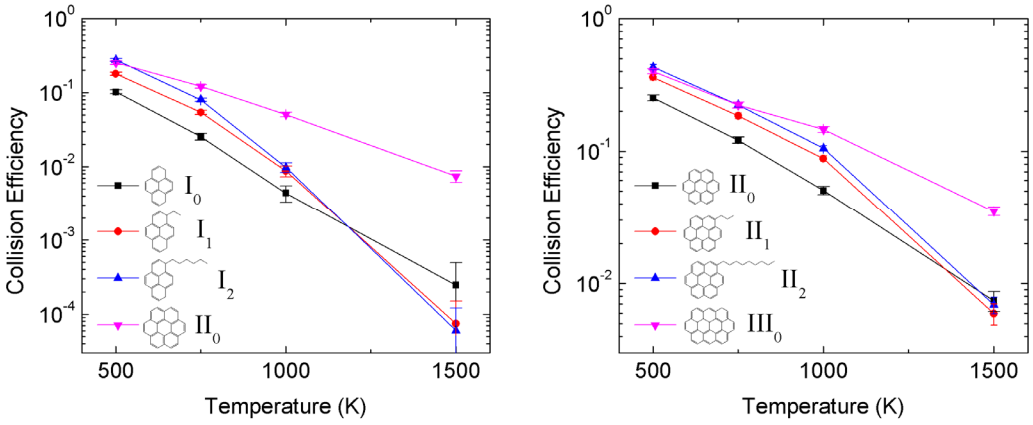

(a) (b)

Figure 4.6. Collision efficiency for PAHs with an aliphatic chain and their corresponding aromatic-only molecules.

Table 4.2. The first ten lowest internal vibrational modes for the molecules in Figure 4.5 and 4.6. (cm^{-1}).

	I_0	I_1	I_2	II_0	II_1	II_2	III_0	I_A
1	101.1077	50.5168	23.6386	91.0358	31.1051	13.2221	62.481	36.7758
2	155.0992	103.8598	43.5319	91.0406	79.2592	21.3909	65.3466	41.8213
3	218.9777	114.8348	58.3493	131.1395	90.7867	35.4711	110.3002	42.1915
4	252.6723	183.4296	69.5631	168.1519	101.7865	42.8167	129.0827	63.7042
5	266.6356	190.6983	103.8597	230.6543	102.0541	73.7885	156.9415	73.0502
6	358.8581	223.8368	118.9634	303.5286	125.7943	75.2488	202.8679	107.3968
7	403.9249	267.0367	139.6433	303.7514	153.5487	84.2938	216.6335	151.2716
8	412.1382	280.1839	154.6507	306.1967	201.1552	95.3237	262.3015	151.8473
9	462.2932	309.1217	158.164	306.4928	245.0242	105.2744	278.6815	157.24
10	502.041	328.2479	182.7755	370.1784	251.5516	125.7995	280.3713	178.0507

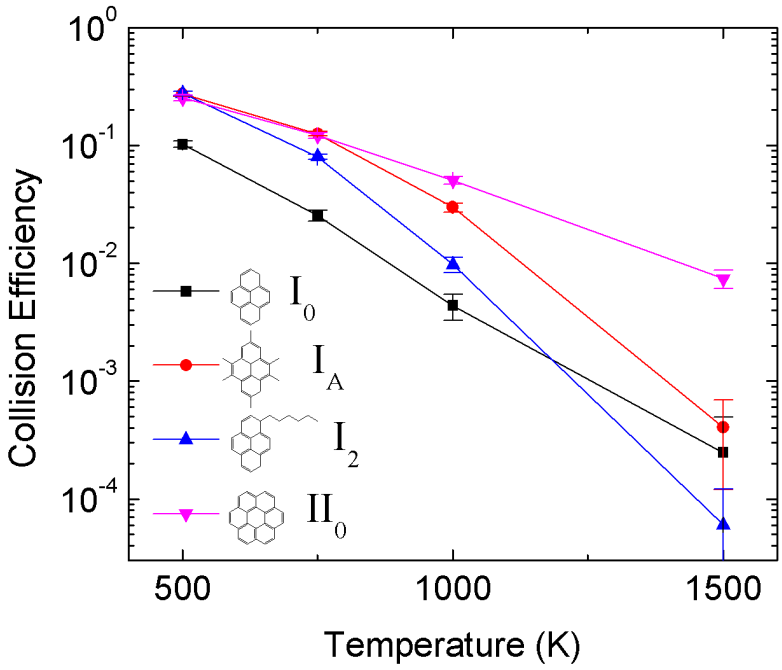

Figure 4.7. Collision efficiency for PAHs with aliphatic chains and their corresponding aromatic-only molecules.

4.5.3. The effect of curvature in the PAH surface

Next, the effect of curvature in the PAH surface is examined. In Figure 4.8, the collision efficiency of V_0, which has three five-membered rings that result in a curved PAH surface, is compared with that of III_0 and IV_0, which are flat PAH molecules. The curved V_0 molecule has a different trend in changes of the

collision efficiency compared to the flat PAH molecules, depending on the temperature, as shown in Figure 4.8. While V_0 (444 amu) is heavier than III_0 (398 amu) and lighter than IV_0 (496 amu), the collision efficiency of V_0 is lower than that of III_0 at temperatures higher than 750 K. We suggest two possible factors that may contribute to this trend: the direction of dimerization and the difference in binding energy for a wide range of collision angles. Firstly, the low collision efficiency of V_0 is due to the curvature in the PAH surface, because there is a preferential direction for dimerization unlike the planar PAH surface, as sketched in Figure 4.9. However, if the temperature is low enough (e.g. 500 K) to accommodate the dimerization in an unfavorable direction, the curvature in the PAH surface may help to increase the collision efficiency. Figure 4.10 shows the possible configurations of dimer structures of PAH molecules with curvatures and PAH molecules with the flat surface. In order to simplify the comparison between two cases, each molecule is assumed to have evenly distributed five interaction sites, and the minimum distance of two PAH molecules is set as 1 (arbitrary scale) for both cases. The interactions within the cutoff distance of 2, which is similar to typical Lennard-Jones potential cutoff in MD simulation, are drawn as dashed lines. Figure 4.11 plots the number of these effective interactions as a function of collision angle. While the number of effective interactions of PAH molecules with the flat surface decreases significantly as the colliding angle increases, the number of effective interactions of PAH molecules with curvature remains same. This

may indicate that, if the temperature is low enough to accommodate the dimerization in an unfavorable direction, curved PAH molecules can have higher collision efficiency than planar PAH molecules, because the curvature enables molecules to have similar binding energies for a wide range of collision angles. This effect is shown in Figure 4.8, where the collision efficiency of V_0 is similar to that of IV_0 at 500K, while IV_0 is more than 10 % heavier than V_0.

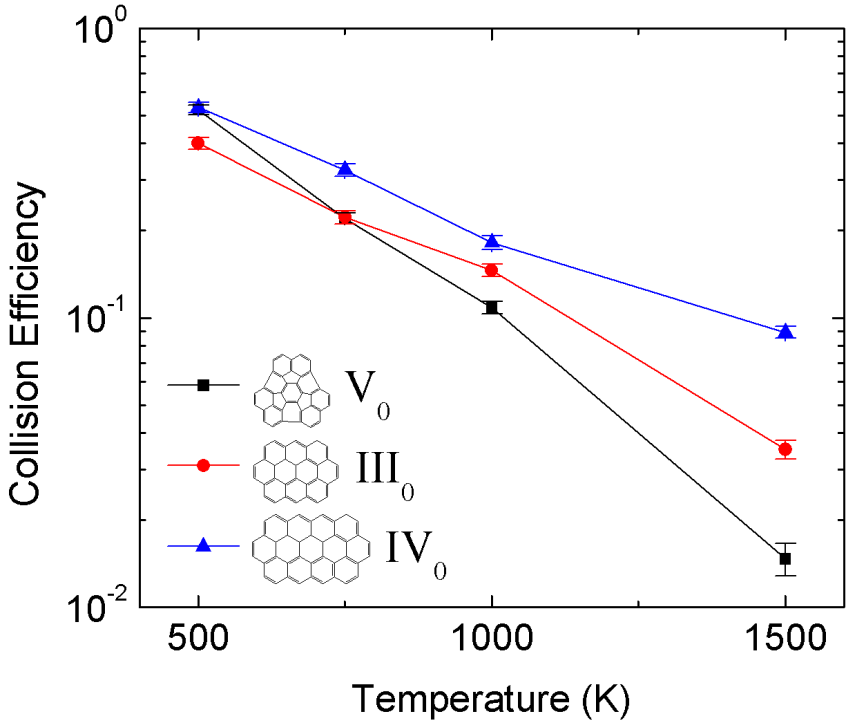

Figure 4.8. Collision efficiency for PAH with curvature (V_0) and PAH with flat surface (III_0 and IV_0).

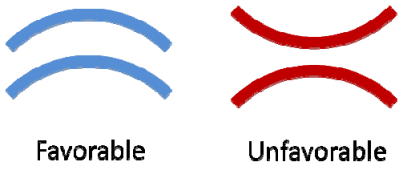

Figure 4.9. Possible configurations of dimer structures of PAH molecules with curvature.

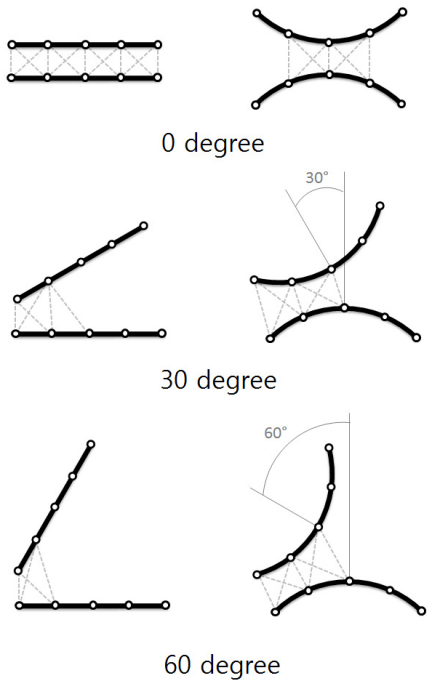

Figure 4.10. Possible configurations of dimer structures of (i) PAH molecules with the flat surface, and (ii) PAH molecules with curvature. Each molecule has five interaction sites. The minimum distance of two PAH molecules is set as 1 (arbitrary scale) and the dashed lines indicate the interactions between the sites within the distance of 2.

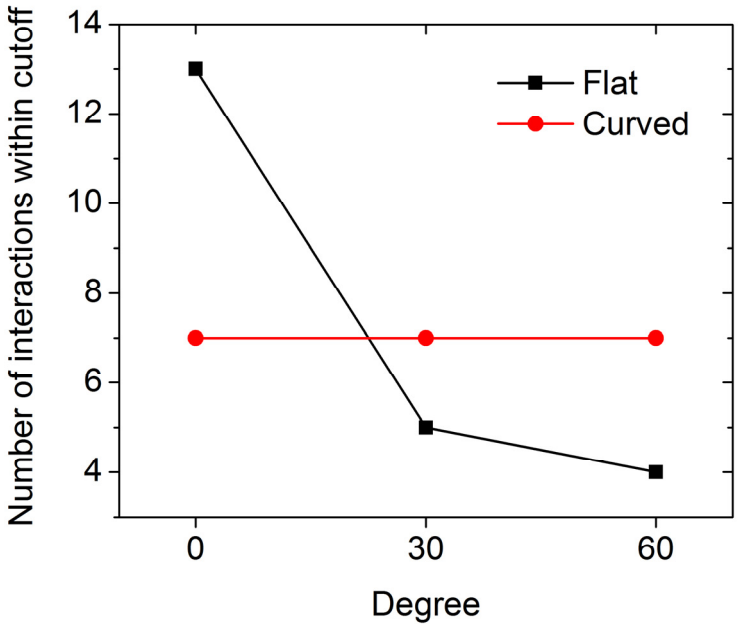

Figure 4.11. Number of effective interactions within the cutoff distance of 2 for the configurations of dimer structures shown in Figure 4.10.

4.5.4. Heteromolecular dimerization

The dimerization of two different planar PAH molecules is also studied. If we follow the argument that the molecular mass is a dominant factor that determines the collision efficiency, one hypothesis we can make is that collision between two molecules with different masses might be expected to result in an efficiency value that falls between the two efficiency values of the corresponding homogeneous

cases. This behavior is because their average mass is between the two different masses. This hypothesis holds true for the case of I_0 and II_0 as shown in Figure 4.12 (a), where the collision efficiency between I_0 and II_0 is between that for I_0 and II_0.

However, as shown in Figure 4.12 (b), the collision efficiency between I_0 and III_0 shows a different trend and it is similar to that of two III_0 molecules. This trend is more evident in Figure 4.12 (c), where the collision efficiency for II_0 and III_0 collisions is higher than that of III_0 only collisions.

One way to account for this trend, which contradicts the hypothesis suggested in the beginning of this section, is by considering collision events of two different molecules with distinct morphologies at various collision angles. Figure 4.13 shows possible configurations of collision events with different angles and orientations and Figure 4.14 plots the corresponding interaction energies. In general, a collision event can occur at any angle, and statistically two thirds of collisions occur at angles greater than 30 degrees. For I_0-III_0, II_0-III_0, and III_0-III_0 cases, the interaction energy values vary sharply from 0 to 30 degrees, but the differences become negligible beyond 30 degrees. In other words, for the majority of collisions, the interaction energies are almost the same regardless of the sizes of these planar PAH molecules.

Moreover, because the smaller molecules have lower average kinetic energies than those of larger molecules in the same temperature conditions, the former has a greater tendency to stack than heavier molecules if the interaction energies are similar. Therefore, since I_0 and II_0 are lighter than III_0, the collision efficiency of I_0-III_0 and II_0-III_0 can be similar to or higher than III_0-III_0 collision case. As shown in Figure 4.12, this phenomenon is more significant in II_0-III_0 case than I_0-III_0 case, since the interaction energies for II_0-III_0 and III_0-III_0 are similar even when they are almost parallel (< 30 degrees), while the interaction energy of I_0-III_0 is relatively weak compared to them (Figure 4.14). Also the number of accessible parallel configurations may influence the results. For example, when interaction energies at 0 degree for A and B types (Figure 4.14 (a) and (b)) are compared, the interaction energies of I_0-III_0 and II_0-III_0 cases are more consistent for both A and B types than that of III_0-III_0 case. This is because smaller planar PAH molecules (e.g. I_0 and II_0) have more accessible parallel configurations than larger planar PAH molecules (e.g. III_0) when they collide with III_0. This can result in lower collision efficiency of III_0-III_0 case than that of II_0-III_0 case.

To sum up, the morphology of PAHs affects collision efficiency significantly in case of heteromolecular collisions. Future study will investigate more complex that involve collision of non-planar PAH molecules.

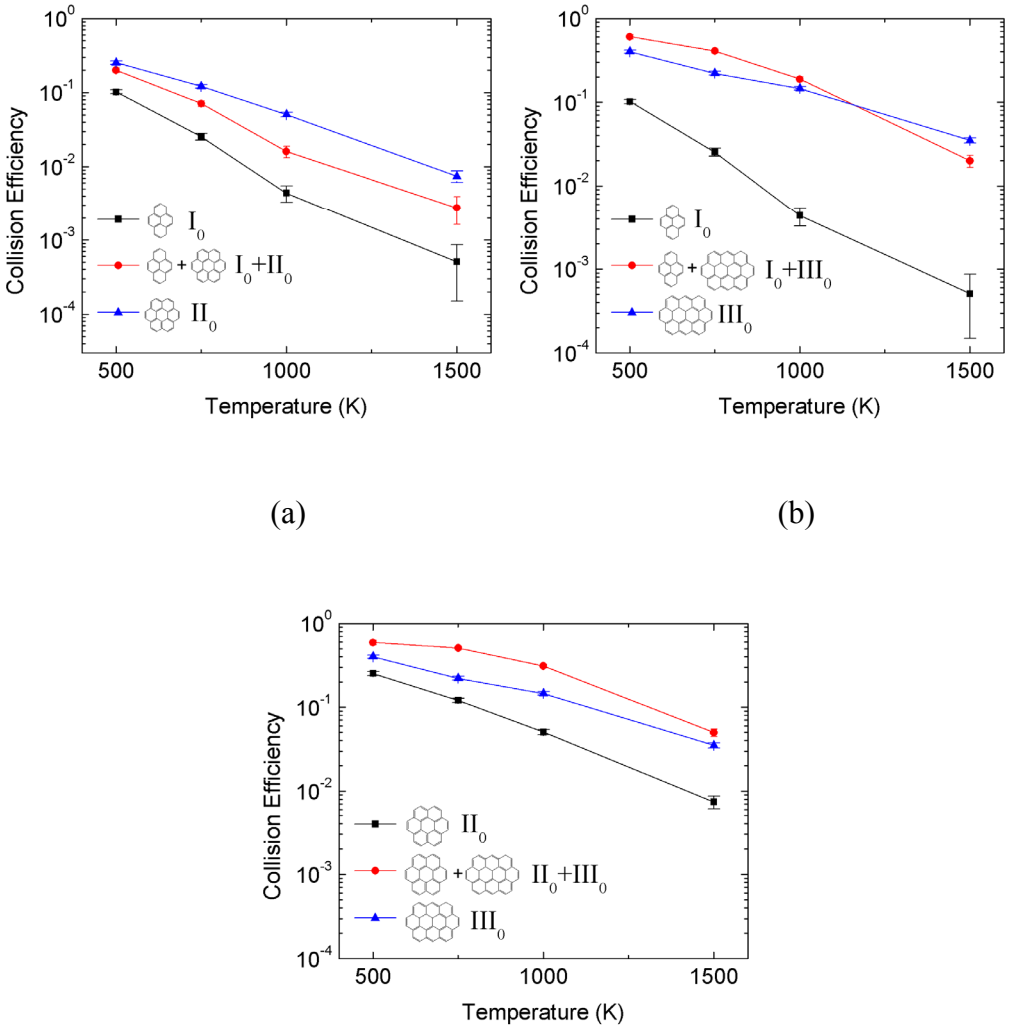

(a) (b)

(c)

Figure 4.12. Collision efficiency for heteromolecular dimerization (red) and homogeneous dimerization of each part (black and blue).

(a) Type A

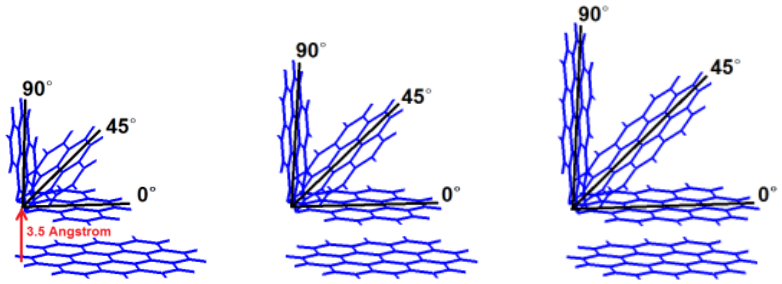

(b) Type B

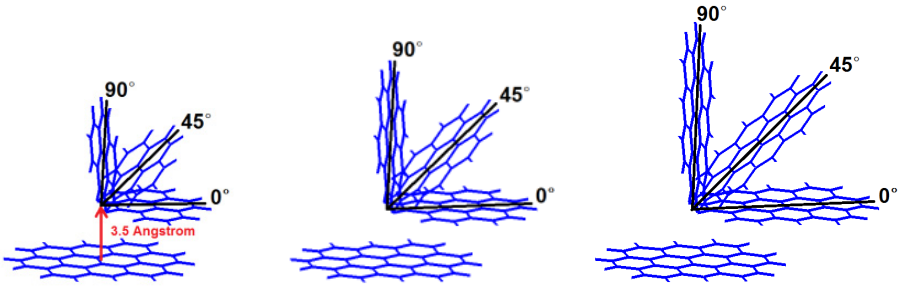

Figure 4.13. Two types of possible configurations of collision events. In the parallel configuration (0 degree), the distance between two PAHs is 3.5 Angstrom.

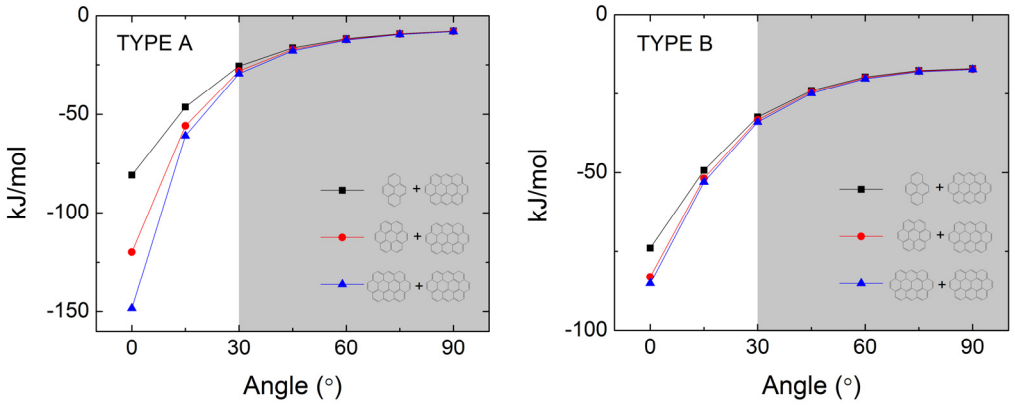

(a) (b)

Figure 4.14. Interaction energies for 0 - 90 degree of the two types of configurations in Figure 4.12. (a) type A (b) type B.

4.6. Conclusions

In this study, MD simulations are used to examine the dimerization collision efficiency of PAH molecules. The pyrene dimerization route as a soot nucleation process is expected to be highly dependent on the various flame temperature conditions, while the larger PAH dimerization route is expected to be more consistent for various temperature conditions. The collision efficiency is primarily influenced by two major factors, temperature and molecular mass. In addition, the presence of aliphatic chains and the curvature of the PAH surface also influence

the dimerization collision efficiency. The steric hindrance and the additional internal vibrational modes are two balancing parameters that determine the effect of aliphatic chains. The dimer configurations influence the collision efficiency of PAHs with curved surface differently in the varied temperature conditions. For the heteromolecular collisions, the interaction energies of various colliding angles induce different behaviors for different molecule types. The results in this chapter will be used for the soot nucleation model in Chapter 5.

Chapter 5

Exploring the role of polycyclic aromatic hydrocarbon dimerization in the soot formation process.

5.1. Objective

In Chapter 4, we obtained a more accurate collision efficiency for pyrene dimerization using molecular dynamics (MD) simulation so that its role in soot formation could be evaluated. The objective of this work is to re-evaluate the current practical use of pyrene dimerization as a soot nucleation process using these collision efficiencies. In particular, two polycyclic aromatic hydrocarbon (PAH) dimerization pathways – pyrene dimerization and coronene dimerization – are evaluated to study the effects of a route that can serve as an alternative to pyrene dimerization. These nucleation pathways are applied to the detailed soot model, and the results are compared with experimental data from a jet-stirred / plug-flow reactor (JSR/PFR) system. We also present the procedure used to obtain

the nucleation rate coefficients as an Arrhenius form from the temperature dependent collision efficiency values.

5.2. Fitting collision efficiency to nucleation rate

As reviewed in the previous chapter, we can define the nucleation rate in terms of the collision rate and the collision efficiency of two molecules. Assuming a free-molecular regime, the nucleation rate can be expressed as [90]

$$r_{nuc} = \beta \times N_{avo} d_{PAH}^2 \sqrt{\frac{4\pi k_B T}{m_{PAH}}} \left[PAH\right]^2 \qquad (5.1)$$

where d_{PAH} is the diameter of the PAH molecule, m_{PAH} is the mass of the PAH molecule, and $\left[PAH\right]$ is the PAH concentration. The collision efficiency (β) is dependent on temperature, and the nucleation reaction is an irreversible reaction that determines the particle nucleation rate. In the CHEMKIN software [90], the nucleation rate is expressed in the Arrhenius form as follows:

$$r_{nuc} = A_{nuc} \times T^{B_{nuc}} \times e^{-E_{nuc}/RT} \times \prod_k \left[\chi_k\right]^{\upsilon_k} \qquad (5.2)$$

To fit the temperature dependent collision efficiency into this equation we suggest the following functional form of β:

$$\beta(T) = A_\beta \times T^{B_\beta} \times e^{-C_\beta / RT} \tag{5.3}$$

where A_β, B_β, and C_β are fitting parameters. Using Equation (5.3), Equation (5.1) is expressed as

$$r_{nuc} = A_\beta N_{avo} d_{PAH}^2 \sqrt{\frac{4\pi k_B}{m_{PAH}}} T^{B_\beta + 1/2} e^{-C_\beta / RT} [PAH]^2 \tag{5.4}$$

The Arrhenius rate coefficients of the nucleation rate can be obtained by comparing Equation (5.4) to Equation (5.2):

$$A_{nuc} = A_\beta N_{avo} d_{PAH}^2 \sqrt{\frac{4\pi k_B}{m_{PAH}}} \tag{5.5}$$

$$B_{nuc} = B_\beta + \frac{1}{2} \tag{5.6}$$

$$E_{nuc} = C_\beta \tag{5.7}$$

These coefficients are used to model the nucleation process in our soot model.

5.3. Soot model

The present study simulates the elementary gas-phase chemistry and subsequent soot particle dynamics using the CHEMKIN software package.

We use the gas-phase reaction mechanism developed by Appel et al. [8], which describes the pyrolysis and oxidation of ethylene molecules. This mechanism includes reactions proposed by GRI-Mech 1.2 [101] and Wang and Frenklach [102] and describes PAH chemistry up to pyrene. PAH growth beyond pyrene is described by a replicating hydrogen-abstraction-acetylene-addition (HACA) reaction sequence. The detailed reaction sequence and rates can be found in the work of Kazakov et al. [28]. This additional reaction mechanism describes PAH growth up to coronene.

Particle dynamics are modeled by the recently introduced CHEMKIN particle tracking module [90], which employs the method of moments developed by Frenklach and coworkers [8, 10, 24]. The method of moments tracks the evolution of a particle system using moments of its particle-size distribution function. Given a particle-size distribution function $n(i)$, where $0 < i < \infty$ represents the particle size class, the *r*-th moment is defined as

$$M_r = \int_0^\infty i^r \times n(i) \times di \qquad r = 0,1,2,... \tag{5.8}$$

Because particle classes are discrete numbers, the number of class *i* particles can be represented by a discrete function N_i and Equation (5.8) is equivalent to

$$M_r = \sum_{i=0}^{\infty} i^r \times N_i \qquad r = 0,1,2,... \tag{5.9}$$

Because the mass of a particle is proportional to its class, the total mass of a soot particle population can be calculated as

$$m_p = \sum_{i=0}^{\infty} \left(i \times m_0 \right) \times N_i = m_0 \times M_1 \tag{5.10}$$

where m_0 is the mass of class 0 particles. A detailed description of the method of moments can be found in the corresponding papers [10, 24].

The nucleation mechanisms are tested against data from experiments of ethylene combustion in a closely coupled JSR/PFR system [103]. In these experiments, extractive probe sampling from the post-flame PFR zone of fuel rich $C_2H_4/O_2/N_2$ combustion (□=2.2) in the JSR (T = 1630 K) yielded detailed profiles of gas species and soot mass concentrations. A more complete description of the experimental setup can be found in reference [103]. In CHEMKIN, the JSR is modeled as a perfectly stirred reactor (PSR). H-abstraction-C_2H_2-addition (HACA) is employed for soot surface growth and the rates used in this study can be found

in [8]. PAH condensation on the soot surface is also employed using the rates given in [104].

5.4. Nucleation Rate Coefficients

To obtain nucleation rate coefficients, Equation (5.3) is fitted to the collision efficiency values reported in our previous study [105]. As shown in Figure 5.1, collision efficiency values are obtained at four different temperatures: 500 K, 750 K, 1000 K, and 1500 K. The curve is fitted using the method of least squares, which assumes that the best-fit curve has the minimal sum of squared errors. The fitting targets are the logarithmic values of the collision efficiency data because the collision efficiency values span a wide range depending on the temperature. For example, the collision efficiency values for pyrene dimerization are 0.102 at 500 K and 0.000248 at 1500 K. If the curves were fitted using nominal values, then the discrepancy between collision efficiency values at different temperature would lead to poor fitting in the high temperature region. Table 5.1 shows the fitting parameters obtained for pyrene and coronene dimerization. As shown in Figure 5.1, the fit curves are very good representations of the data. The Arrhenius rate coefficients in Table 5.2 are obtained from Equations (5.5), (5.6), and (5.7)

using the collision efficiency curve parameters given in Table 5.1. These rate coefficients can be readily adopted by existing soot models.

Table 5.1. Fitting parameters for Equation (5.3).

	A_β	B_β	C_β
Pyrene Dimerization	1.00E+37	-12.3	11130
Coronene Dimerization	1.00E+22	-7.285	6757

Table 5.2. Nucleation rate coefficients for the dimerization of pyrene and coronene.

	A_{nuc}	B_{nuc}	E_{nuc} (cal/mol)
Pyrene Dimerization	1.37E+50	-11.8	11130
Coronene Dimerization	1.36E+35	-6.785	6757

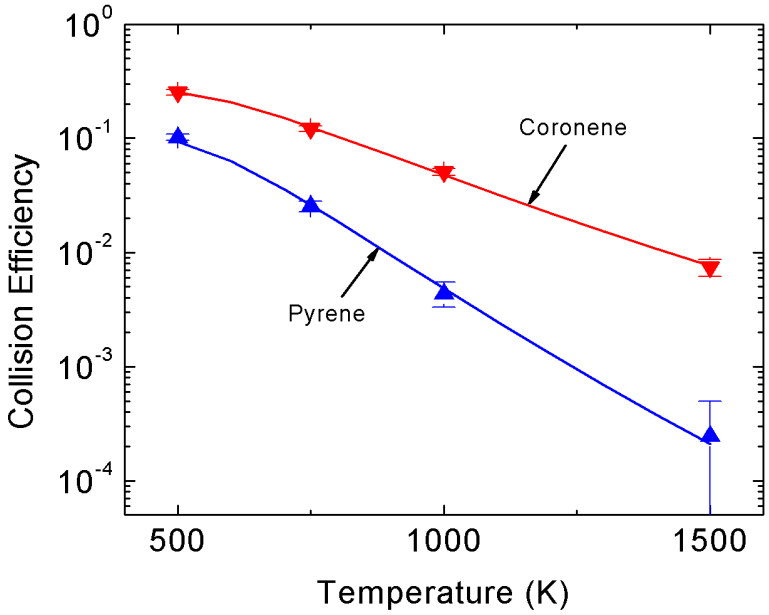

Figure 5.1. Dimerization collision efficiency data [105] and fitted curves obtained from Equation (5.3). The fits are shown to be very close.

As mentioned in Chapter 2, Raj et al. [89] recently modeled the PAH collision efficiency as an empirical function of molecular mass M_{min} and diameter D_{min}, as shown below:

$$C_E = \frac{1}{1+\exp\left(-\left(A\times\frac{D_{\min}^3}{M_{\min}}\right)+\left(\frac{M_{\min}}{B}\right)^6 - C\right)} \qquad (5.11)$$

A, *B*, and *C* are fitting parameters and they were obtained by matching the shape of the computed mass spectra to that of the experimental mass spectra of a laminar premixed ethylene flame. It should be noted that the collision efficiency obtained by Equation (5.11) does not depend on temperature. Hence, as shown in Figure 2, there are large discrepancies at both low and high temperature. In this study, we employ the collision efficiency of Raj et al. [89] and the collision efficiency of Chung and Violi [105] for comparison.

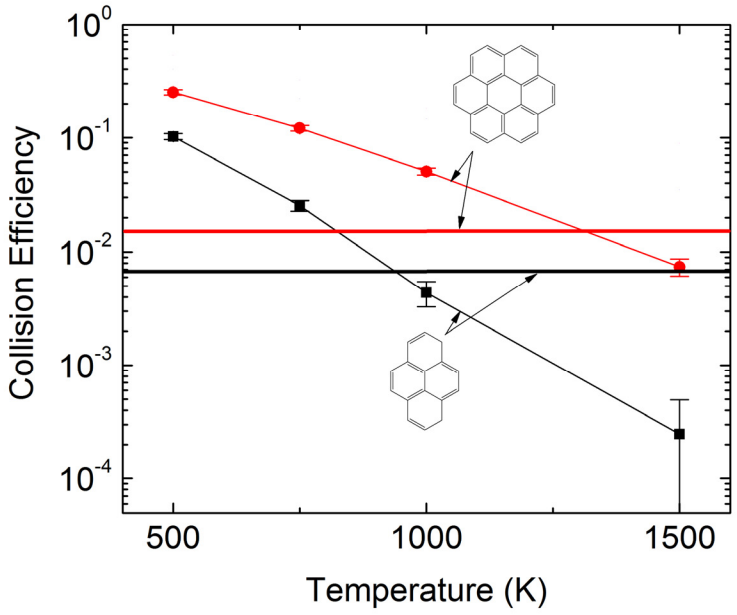

Figure 5.2. Comparison between the dimerization collision efficiency data from Raj et al. [89] and Chung and Violi [105].

5.5. Computational results

As mentioned in the previous section, the gas-phase chemistry developed by Appel et al. [8] is used for gaseous species up to pyrene, and the HACA reaction sequence [28] is used for larger PAH molecules up to coronene. Wen et al. [106] showed that the reaction mechanism by Appel et al. significantly under-predicts the pyrene concentration when the PFR is solved with the soot model. A similar trend is also observed in this study using the same gas-phase chemistry. To improve the pyrene concentration prediction, the coefficients of the reactions leading to pyrene formation are modified by increasing the pre-exponential factors. These reactions and their modified reaction coefficients are listed in Table 5.3. The calculated concentration profiles as a function of PFR residence time are plotted in Figure 5.3 along with the available experimental data [103]. The concentration of pyrene is slightly under-predicted as compared to the experimental data, and the concentration of coronene is also slightly lower than the peak of the experimental data. However, the difference between the calculated pyrene concentration and the coronene concentration is similar to the difference between the experimental measurements of pyrene concentration and coronene concentration. Overall, the predictions of species concentrations generally agree fairly well with the experimental data.

Table 5.3. Reaction coefficients modified and used in this study. The original pre-exponential factors [8] are multiplied by 10^2.

Reaction	A	β	E_a
A3 + C_2H = A3C_2H + H	5.00E+15	0	0
A3- + C_2H_2 = A3C_2H_2	8.00E+63	-14.5	34800
A3- + C_2H_2 = A3C_2H + H	1.20E+28	-3.44	30200
A3- + C_2H_2 = A4 + H	3.30E+26	-3.36	17800
A3C_2H + H = A4 + H	9.00E+40	-7.39	20700
A3C_2H_2 = A4 + H	2.00E+65	-15.28	43200

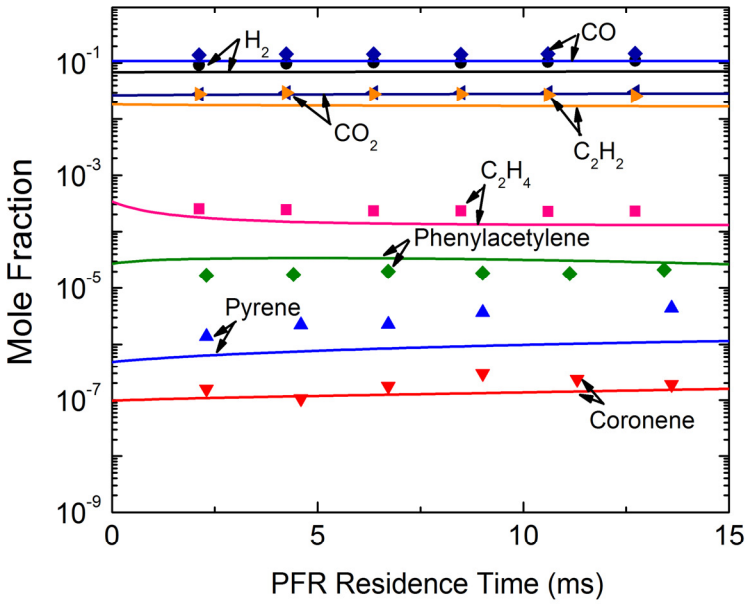

Figure 5.3. Gas-phase species concentration profiles. The symbols represent measurements [103] and the lines indicate simulation results.

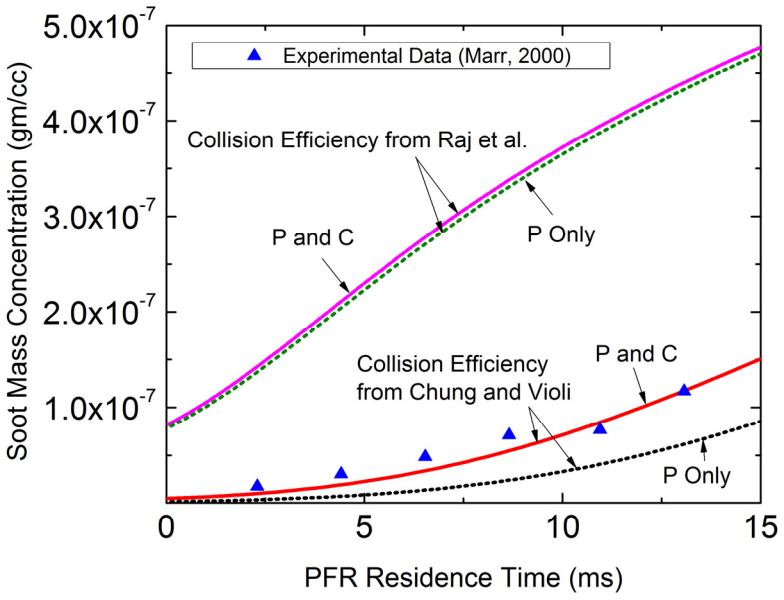

Figure 5.4. Soot mass concentration profiles determined using collision efficiencies obtained from Raj et al.[89] and Chung and Violi[105]. The experimental data are from [103]. The solid lines represent the nucleation rates of the pyrene and coronene dimerization route, and the dashed line represents the rates of the pyrene-only dimerization route.

As mentioned previously, two sets of dimerization collision efficiencies obtained from Raj et al. [89] and Chung and Violi [105] are applied to the JSR/PFR model separately. Furthermore, for each set, two nucleation pathways, pyrene dimerization only and both pyrene and coronene dimerization, are

simulated in order to evaluate the relative roles of pyrene and coronene in the soot nucleation model. Figure 5.4 shows soot mass concentrations in the PFR for all cases studied, plotted as a function of residence time. The results show that the model using the temperature independent collision efficiency presented by Raj et al. significantly over-predicts the soot mass concentration for both the pyrene-only and pyrene and coronene dimerization cases. To more thoroughly investigate the effect of the nucleation pathway, the nucleation rates, defined as mole/cm^3sec, are plotted in Figure 5.5. The plots indicate that the collision efficiency presented by Raj et al. results in higher nucleation rates than the collision efficiency suggested by Chung and Violi. This trend is not surprising because the difference in collision efficiency between the two studies reaches almost two orders of magnitude in the case of pyrene at 1500 K as shown in Figure 5.2. In the soot model using the dimerization collision efficiencies suggested by Chung and Violi, pyrene dimerization alone under-predicts soot formation. The addition of the coronene dimerization route to the pyrene dimerization route, however, improves the match with the experimental data. This shows that, at least for this flame condition, pyrene dimerization, as the sole soot nucleation mechanism, cannot adequately reproduce the experimental soot mass concentration. Coronene dimerization is the dominant nucleation route. The soot nucleation rates in Figure 5.5 also show that the addition of coronene dimerization increases the nucleation rate up to a factor of four, which confirms that coronene dimerization is a more

dominant nucleation pathway than pyrene dimerization in these conditions. In the model using the dimerization collision efficiencies presented by Raj et al., the difference between the pyrene dimerization model and the pyrene and coronene dimerization model is small because the pyrene dimerization route is the dominant pathway when using their temperature independent dimerization collision efficiency values.

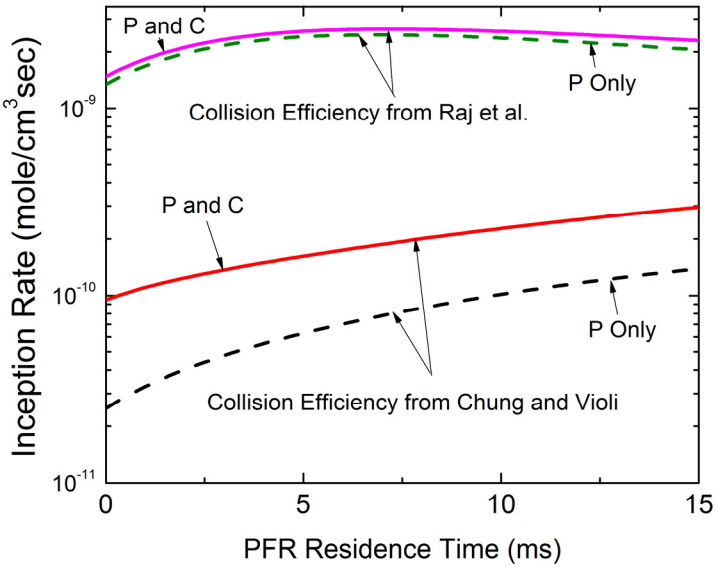

Figure 5.5. Soot nucleation rates determined using collision efficiencies obtained from Raj et al. [89] and Chung and Violi [105]. The solid lines represent the nucleation rates of the pyrene and coronene dimerization route, and the dashed lines indicate the rates of the pyrene-only dimerization route.

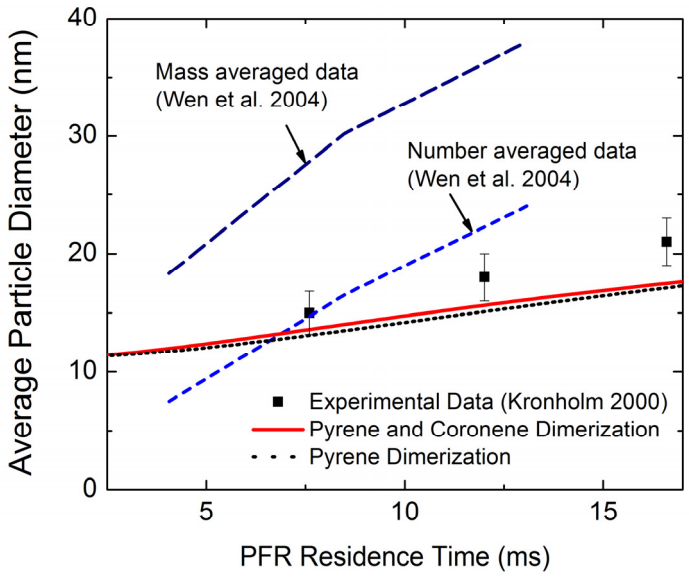

Figure 5.6. Average soot particle diameter. The red line shows the average diameter obtained from the model with the pyrene and coronene dimerization route, and the black dotted line shows that of the pyrene-only dimerization route. The two dashed lines show the predicted values from [106] using the mass averaged value (navy) and the number averaged value (blue). The experimental data are from [107].

Figure 5.6 compares the calculated average soot particle diameter obtained by various methods and measured arithmetic mean diameter data [106]. In contrast to the soot mass concentration, the average diameters obtained from both

pyrene-only and pyrene and coronene dimerization routes differ little. These results suggest that the nucleation mechanism is not a major factor governing the average diameter, and that other mechanisms, such as the surface growth and coagulation of soot particles, must play a dominant role. While these results slightly under-predict the experimental data, they surpass the previous modeling predictions of Wen et al. [106] for the same flame condition. This more accurate prediction further validates the accuracy of our modeling approach.

5.6. Conclusions

This study suggests a novel computational approach that uses temperature-dependent collision efficiency data to obtain PAH dimerization rate coefficients that can be applied to soot formation models. The nucleation rates are obtained from the curve fit of the collision efficiency results from MD simulations. The nucleation rates were tested against data from experiments using JSR/PFR systems. Using the newly obtained Arrhenius form of the nucleation rate of pyrene dimerization from the collision efficiency data of our previous study, we demonstrate that pyrene dimerization, as the key soot nucleation mechanism, cannot adequately reproduce the experimental soot mass concentration. An additional pathway, such as coronene dimerization in this case, must be included

to improve the match with experimental data. In addition, models using the temperature independent collision efficiency values of Raj et al. are studied, and the results show that these models significantly over-predict the soot mass concentration. Overall, the results obtained using the collision efficiency from MD simulations are in accordance with the arguments of previous studies [5, 31] that pyrene dimerization may not be the key nucleation step. Furthermore, the results suggest the possibility that the dimerization of larger PAH molecules may be more important than pyrene dimerization. Therefore, more extensive studies of the underlying physics of the soot nucleation process at the molecular scale are needed to construct a better soot model and to understand the entire soot formation process.

Chapter 6

Conclusions

This study aimed to investigate the major pathways of the soot nucleation process using recently advanced computational approaches such as molecular dynamics (MD) simulation, the kinetic Monte-Carlo (KMC) method, and ab-initio methods. This thesis identified two extreme regimes of nucleation models: a chemical growth and a physical process involving agglomeration of polycyclic aromatic hydrocarbons (PAHs).

The formation of nanoparticles via chemical growth in two counterflow diffusion flames was studied using the atomistic model for particle inception (AMPI) code. Soot formation characteristics in counterflow diffusion flames can be categorized into soot formation/oxidation flame (SFO) and soot formation flame (SF), based on the relative position between the flame and the particle stagnation plane. The AMPI code that describes the particle inception via chemical reactions is able to reproduce very well the experimental trends

observed by Kang et al. [5] for the SFO flame due to the high concentration of C_2H_2 and high temperature (> 1500 K). For the SF flame, the kinetic growth mechanism embedded in the AMPI code was able to describe particle formation at the beginning of the soot zone, but, we did not observe any significant chemical growth for the rest of soot zone where the temperature is reduced to ~ 1250K. To explain the experimental evidence showing particle formation in this region, another possible soot nucleation pathway was needed to be considered.

To complement these results, the dependence of sizes and concentrations on the physical agglomeration of nanoparticles in a wide range of temperatures is explored using fullerenes. Fullerenes have characteristics resembling the particles found in soot, but their simpler structure makes simulation more tractable. The computational findings were related to the experimental data to assess the feasibility of physical agglomeration. The results indicated that particle nucleation is the result of physical agglomeration and chemical growth pathways, and the combustion conditions determine the relative importance of these two routes.

Also, the use of pyrene dimerization, which is currently a de-facto standard to model soot nucleation, was carefully re-evaluated. The dimerization of PAHs has been regarded as one of the most important processes in soot formation. In particular, the dimerization of pyrene is widely used as a nucleation process in many soot modeling studies. However, recent findings [5, 31] indicate that the

dimerization of pyrene may not be a key step in soot formation. In this study, the nucleation rate is defined in terms of the collision frequency and the collision efficiency of two molecules, and MD simulations were used to examine the dimerization collision efficiency of PAH molecules. The results indicate that the role of the pyrene dimerization route as a soot nucleation process is highly dependent on various flame temperature conditions, while the larger PAH dimerization route is more consistent across various temperature conditions. In addition, the results show that the presence of aliphatic chains and the curvature of the PAH surface also influence dimerization collision efficiency. Also, for heteromolecular collisions, the interaction energies of various colliding angles induce different behaviors for different molecule types.

Using the collision efficiencies obtained by MD, the novel procedure to obtain the nucleation rate as an Arrhenius form was presented. Two PAH dimerization pathways – pyrene dimerization and coronene dimerization – were obtained by fitting their collision efficiencies to Arrhenius forms, and were applied to the soot model of a jet-stirred / plug-flow reactor (JSR/PFR) system. The results, such as soot mass concentration, soot nucleation rate, and average particle diameter, were obtained using the method of moment approach and compared with published experimental data. The results suggest that the use of pyrene dimerization alone as a nucleation step is not adequate to model the soot

formation process; instead, different approaches are needed for different flame conditions.

The results of this thesis provide insight on the soot nucleation process and can be utilized to improve current soot formation models. Recommendations for future work include: (i) identify unified model for chemical and physical nucleation pathways, (ii) explore more general description on collision rates, and (iii) study more experimental conditions.

Appendices

A. Atomic partial charges

Atomic partial charges for the molecules in Chapter 4.

Atomic partial charges for I_0.

Atom	Charge (*e*)	X (nm)	Y (nm)	Z (nm)
C	-0.078736	0.04	-0.086	-0.339
C	-0.161397	0.078	0.04	-0.295
C	0.123441	0.063	0.076	-0.16
C	-0.006618	0.008	-0.018	-0.069
C	0.123442	-0.031	-0.147	-0.114
C	-0.161399	-0.014	-0.179	-0.25
C	-0.131147	0.101	0.206	-0.111
C	-0.006618	-0.008	0.018	0.069
C	0.12344	0.031	0.146	0.114
C	-0.131147	0.086	0.239	0.019
C	-0.161397	0.014	0.179	0.25
H	0.083701	0.044	0.279	0.285
C	-0.078737	-0.04	0.087	0.339
C	-0.161399	-0.079	-0.04	0.295
C	0.123443	-0.064	-0.077	0.16

C	-0.131147	-0.102	-0.206	0.112
C	-0.131146	-0.087	-0.24	-0.019
H	0.085061	-0.116	-0.339	-0.057
H	0.085062	-0.144	-0.277	0.184
H	0.085062	0.144	0.278	-0.184
H	0.086035	0.052	-0.114	-0.444
H	0.083701	0.12	0.112	-0.366
H	0.083701	-0.044	-0.278	-0.285
H	0.085062	0.116	0.339	0.057
H	0.086035	-0.053	0.114	0.444
H	0.083702	-0.121	-0.113	0.366

Atomic partial charges for I_1.

Atom	Charge (*e*)	X (nm)	Y (nm)	Z (nm)
C	-0.126459	0.178	0.02	-0.161
C	-0.168774	0.125	0.147	-0.134
C	0.124626	0.013	0.162	-0.052
C	0.004102	-0.047	0.045	0.005
C	0.068392	0.008	-0.085	-0.023
C	0.070223	0.122	-0.097	-0.107
C	-0.130155	-0.044	0.29	-0.023
C	-0.134702	-0.153	0.303	0.057
C	0.12331	-0.216	0.188	0.116
C	-0.012943	-0.162	0.058	0.089
C	0.126997	-0.222	-0.057	0.146
C	-0.137827	-0.166	-0.186	0.117
C	-0.132751	-0.056	-0.199	0.037
C	-0.161546	-0.328	0.198	0.199
C	-0.079783	-0.387	0.084	0.255
C	-0.160968	-0.335	-0.042	0.229

C	-0.24259	0.181	-0.233	-0.137
C	-0.330932	0.303	-0.236	-0.229
H	0.079151	0.265	0.013	-0.225
H	0.081886	0.171	0.234	-0.178
H	0.083594	0.003	0.379	-0.067
H	0.083547	-0.195	0.4	0.079
H	0.083021	-0.212	-0.274	0.16
H	0.081727	-0.016	-0.297	0.018
H	0.082555	-0.37	0.297	0.22
H	0.084979	-0.475	0.095	0.318
H	0.082537	-0.381	-0.13	0.273
H	0.115785	0.208	-0.281	-0.042
H	0.115598	0.102	-0.297	-0.18
H	0.102321	0.336	-0.34	-0.243
H	0.11246	0.387	-0.18	-0.188
H	0.112619	0.28	-0.195	-0.328

Atomic partial charges for I_2.

Atom	Charge (*e*)	X (nm)	Y (nm)	Z (nm)
C	-0.12605	0.038	0.168	-0.044
C	-0.172424	-0.03	0.284	-0.007
C	0.126871	-0.142	0.278	0.077
C	0.001158	-0.186	0.15	0.124
C	0.072172	-0.116	0.032	0.085
C	0.060383	-0.003	0.041	-0.001
C	-0.130731	-0.213	0.396	0.119
C	-0.134764	-0.322	0.388	0.201
C	0.122886	-0.368	0.261	0.249
C	-0.012666	-0.3	0.142	0.209
C	0.127278	-0.346	0.015	0.257
C	-0.138628	-0.274	-0.102	0.215
C	-0.133094	-0.165	-0.094	0.134
C	-0.161532	-0.481	0.25	0.333

C	-0.079788	-0.524	0.125	0.378
C	-0.161084	-0.457	0.009	0.341
C	-0.243521	0.071	-0.084	-0.043
C	-0.1899	0.192	-0.066	-0.136
C	-0.177124	0.259	-0.199	-0.173
C	-0.167436	0.38	-0.183	-0.265
C	-0.174145	0.447	-0.317	-0.302
C	-0.317693	0.568	-0.301	-0.395
H	0.080865	0.124	0.177	-0.11
H	0.081827	0.004	0.381	-0.042
H	0.083471	-0.179	0.492	0.083
H	0.083386	-0.376	0.477	0.231
H	0.082849	-0.308	-0.199	0.251
H	0.082262	-0.114	-0.186	0.105
H	0.08242	-0.533	0.34	0.362
H	0.08481	-0.611	0.12	0.443
H	0.082387	-0.491	-0.087	0.376
H	0.112089	0.104	-0.138	0.046
H	0.112052	0.001	-0.153	-0.093
H	0.09908	0.266	-0.001	-0.088
H	0.099106	0.161	-0.015	-0.228
H	0.089451	0.185	-0.266	-0.22
H	0.089467	0.29	-0.25	-0.081
H	0.08839	0.453	-0.117	-0.218
H	0.088399	0.349	-0.133	-0.357
H	0.091702	0.372	-0.383	-0.349
H	0.091707	0.478	-0.368	-0.21
H	0.099989	0.613	-0.397	-0.419
H	0.102059	0.645	-0.238	-0.349
H	0.102065	0.538	-0.253	-0.489

Atomic partial charges for II_0.

Atom	Charge (*e*)	X (nm)	Y (nm)	Z (nm)

C	-0.143382	0.249	-0.253	-0.119
C	0.100288	0.118	-0.207	-0.154
C	0.016286	0.06	-0.104	-0.077
C	0.01634	0.131	-0.047	0.033
C	0.100319	0.26	-0.094	0.065
C	-0.143496	0.317	-0.198	-0.014
C	0.016367	-0.071	-0.056	-0.11
C	0.016368	0.071	0.057	0.11
C	0.016286	-0.06	0.104	0.078
C	0.01634	-0.13	0.048	-0.032
C	0.100288	-0.118	0.208	0.155
C	-0.143421	-0.044	0.263	0.263
C	-0.143421	0.081	0.217	0.295
C	0.100265	0.142	0.113	0.219
C	-0.143447	0.272	0.064	0.249
C	-0.143381	0.329	-0.036	0.175
H	0.085112	0.43	-0.074	0.199
H	0.085113	0.326	0.108	0.334
H	0.085108	0.294	-0.333	-0.18
H	0.085114	0.418	-0.234	0.012
H	0.085113	-0.091	0.343	0.322
H	0.085122	0.136	0.26	0.38
C	-0.143421	0.046	-0.262	-0.263
C	-0.143421	-0.08	-0.216	-0.294
C	0.100265	-0.142	-0.112	-0.218
H	0.085113	0.092	-0.342	-0.322
H	0.085122	-0.136	-0.259	-0.379
C	-0.143447	-0.272	-0.064	-0.249
C	-0.143381	-0.328	0.036	-0.174
C	0.100319	-0.259	0.094	-0.065
H	0.085113	-0.326	-0.108	-0.334
H	0.085112	-0.429	0.074	-0.199
C	-0.143382	-0.248	0.254	0.12
H	0.085108	-0.293	0.334	0.179
C	-0.143496	-0.316	0.199	0.014
H	0.085114	-0.417	0.235	-0.012

Atomic partial charges for II_1.

Atom	Charge (*e*)	X (nm)	Y (nm)	Z (nm)
C	-0.14337	-0.258	0.388	0.153
C	-0.14442	-0.154	0.427	0.071
C	0.104205	-0.065	0.333	0.014
C	0.010998	-0.084	0.195	0.043
C	0.012384	-0.191	0.153	0.127
C	0.100931	-0.279	0.25	0.183
C	-0.147081	0.043	0.37	-0.07
C	-0.141448	0.128	0.277	-0.124
C	0.102447	0.111	0.138	-0.097
C	0.017738	0.004	0.097	-0.013
C	-0.215424	0.198	0.039	-0.152
C	0.091842	0.182	-0.096	-0.126
C	0.051896	0.073	-0.139	-0.04
C	0.029211	-0.015	-0.042	0.015
C	-0.149546	0.051	-0.275	-0.01
C	-0.149513	-0.053	-0.314	0.072
C	0.103587	-0.142	-0.22	0.129
C	0.010552	-0.122	-0.082	0.1
C	-0.14247	-0.251	-0.258	0.214
C	-0.144464	-0.335	-0.165	0.267
C	0.09964	-0.318	-0.025	0.24
C	0.017442	-0.211	0.015	0.156
C	-0.143101	-0.404	0.074	0.294
C	-0.1447	-0.385	0.207	0.267
C	-0.236257	0.275	-0.2	-0.185
C	-0.187242	0.388	-0.148	-0.275
C	-0.320551	0.476	-0.263	-0.329
H	0.083995	-0.324	0.462	0.195
H	0.084095	-0.139	0.533	0.05
H	0.08382	0.058	0.476	-0.092
H	0.08304	0.21	0.308	-0.188

H	0.078586	0.278	0.073	-0.215
H	0.082296	0.116	-0.352	-0.051
H	0.083187	-0.068	-0.42	0.094
H	0.084288	-0.264	-0.364	0.235
H	0.084455	-0.417	-0.195	0.332
H	0.084175	-0.485	0.042	0.359
H	0.084429	-0.452	0.281	0.309
H	0.111734	0.319	-0.258	-0.103
H	0.111777	0.216	-0.272	-0.242
H	0.103	0.451	-0.079	-0.219
H	0.103004	0.346	-0.092	-0.36
H	0.102511	0.556	-0.225	-0.392
H	0.104162	0.416	-0.334	-0.388
H	0.10416	0.522	-0.319	-0.247

Atomic partial charges for II_2.

Atom	Charge (*e*)	X (nm)	Y (nm)	Z (nm)
C	-0.143254	0.621	-0.052	-0.459
C	-0.144553	0.56	0.065	-0.426
C	0.104198	0.446	0.068	-0.341
C	0.010887	0.396	-0.056	-0.29
C	0.012114	0.459	-0.178	-0.325
C	0.100874	0.573	-0.177	-0.411
C	-0.147374	0.38	0.188	-0.304
C	-0.141027	0.271	0.187	-0.222
C	0.101029	0.219	0.065	-0.17
C	0.018696	0.281	-0.056	-0.205
C	-0.215691	0.105	0.062	-0.085
C	0.092708	0.053	-0.055	-0.034
C	0.053038	0.117	-0.18	-0.069
C	0.028431	0.23	-0.18	-0.154

C	-0.149468	0.069	-0.306	-0.021
C	-0.149794	0.131	-0.423	-0.054
C	0.103195	0.245	-0.426	-0.139
C	0.01074	0.294	-0.303	-0.189
C	-0.142505	0.31	-0.547	-0.176
C	-0.144449	0.42	-0.546	-0.258
C	0.09922	0.473	-0.425	-0.31
C	0.01789	0.409	-0.301	-0.275
C	-0.142994	0.586	-0.421	-0.395
C	-0.144756	0.635	-0.302	-0.444
C	-0.246911	-0.069	-0.056	0.057
C	-0.187074	-0.132	0.079	0.09
C	-0.17784	-0.254	0.067	0.183
C	-0.176229	-0.319	0.201	0.217
C	-0.17501	-0.44	0.189	0.31
C	-0.174196	-0.505	0.323	0.345
C	-0.165737	-0.626	0.311	0.436
C	-0.173745	-0.691	0.445	0.471
C	-0.317495	-0.814	0.432	0.564
H	0.0839	0.709	-0.052	-0.525
H	0.084019	0.598	0.159	-0.464
H	0.083753	0.419	0.282	-0.342
H	0.083024	0.221	0.28	-0.194
H	0.079394	0.058	0.157	-0.06
H	0.082569	-0.017	-0.309	0.045
H	0.083095	0.092	-0.518	-0.016
H	0.084228	0.272	-0.641	-0.138
H	0.084357	0.469	-0.639	-0.285
H	0.084113	0.634	-0.514	-0.422
H	0.084356	0.722	-0.301	-0.509
H	0.11211	-0.146	-0.12	0.012
H	0.112103	-0.042	-0.106	0.151
H	0.099476	-0.162	0.13	-0.002
H	0.099481	-0.057	0.144	0.138
H	0.089591	-0.223	0.016	0.276
H	0.08959	-0.328	0.001	0.135
H	0.08878	-0.348	0.252	0.124
H	0.08878	-0.243	0.266	0.265

H	0.088129	-0.41	0.138	0.403
H	0.088129	-0.515	0.124	0.262
H	0.087728	-0.535	0.374	0.251
H	0.087727	-0.43	0.388	0.392
H	0.087128	-0.597	0.26	0.53
H	0.087128	-0.702	0.246	0.389
H	0.091032	-0.721	0.496	0.379
H	0.091032	-0.617	0.51	0.519
H	0.099259	-0.857	0.53	0.587
H	0.101536	-0.786	0.385	0.659
H	0.101535	-0.891	0.37	0.518

Atomic partial charges for III_0.

Atom	Charge (*e*)	X (nm)	Y (nm)	Z (nm)
C	-0.140163	-0.355	-0.113	0.277
C	0.097727	-0.318	0.019	0.236
C	0.011861	-0.205	0.034	0.15
C	-0.019325	-0.132	-0.081	0.107
C	0.143198	-0.171	-0.212	0.15
C	-0.139729	-0.286	-0.223	0.237
C	0.055127	-0.02	-0.066	0.022
C	-0.019315	0.053	-0.18	-0.021
C	0.143196	0.012	-0.31	0.023
C	-0.261129	-0.099	-0.323	0.107
C	0.011852	0.165	-0.164	-0.107

C	0.097728	0.239	-0.278	-0.15
C	-0.140165	0.196	-0.408	-0.104
C	-0.139726	0.089	-0.423	-0.023
C	0.011854	0.205	-0.034	-0.15
C	0.09773	0.318	-0.019	-0.236
C	-0.149946	0.389	-0.135	-0.277
C	-0.149947	0.35	-0.261	-0.235
C	-0.019326	0.132	0.081	-0.107
C	0.143199	0.171	0.212	-0.15
C	-0.139729	0.286	0.223	-0.237
C	-0.140164	0.355	0.113	-0.277
C	0.055125	0.02	0.066	-0.022
C	-0.019315	-0.053	0.18	0.021
C	0.143198	-0.012	0.31	-0.023
C	-0.261128	0.099	0.323	-0.107
C	0.011842	-0.165	0.164	0.107
C	0.097733	-0.239	0.278	0.15
C	-0.140168	-0.196	0.408	0.104
C	-0.139726	-0.089	0.423	0.023
C	-0.149944	-0.389	0.135	0.277
C	-0.149949	-0.35	0.261	0.235
H	0.085911	-0.441	-0.124	0.343
H	0.086061	-0.316	-0.322	0.269
H	0.084154	-0.129	-0.422	0.14
H	0.085909	0.252	-0.495	-0.138
H	0.086062	0.058	-0.522	0.01
H	0.085332	0.474	-0.123	-0.342
H	0.085331	0.406	-0.348	-0.268
H	0.086061	0.316	0.322	-0.269
H	0.085911	0.441	0.124	-0.343
H	0.084154	0.129	0.422	-0.14
H	0.085909	-0.252	0.495	0.138
H	0.086062	-0.058	0.522	-0.01
H	0.085334	-0.474	0.123	0.342
H	0.08533	-0.406	0.348	0.268

Atomic partial charges for IV_0.

Atom	Charge (*e*)	X (nm)	Y (nm)	Z (nm)
C	0.009181	0.258	-0.213	-0.171
C	0.100502	0.331	-0.328	-0.214
C	-0.138305	0.288	-0.458	-0.168
C	-0.137273	0.181	-0.473	-0.087
C	0.149466	0.105	-0.359	-0.041
C	-0.027975	0.146	-0.228	-0.085
C	-0.264836	-0.005	-0.373	0.042
C	0.184479	-0.08	-0.261	0.086
C	-0.050177	-0.04	-0.13	0.043
C	0.05259	0.073	-0.115	-0.042
C	-0.264836	-0.192	-0.273	0.172
C	0.149465	-0.264	-0.162	0.214
C	-0.027975	-0.225	-0.03	0.171
C	0.052591	-0.113	-0.016	0.086
C	-0.137274	-0.379	-0.174	0.301
C	-0.138306	-0.448	-0.064	0.341
C	0.100497	-0.41	0.069	0.3
C	0.009183	-0.297	0.084	0.214
C	-0.153843	-0.48	0.184	0.341
C	-0.153842	-0.442	0.31	0.299
C	0.100495	-0.331	0.328	0.214
C	0.009181	-0.258	0.213	0.171
C	-0.138304	-0.288	0.458	0.169
C	-0.137273	-0.181	0.473	0.087
C	0.149468	-0.105	0.359	0.042
C	-0.027975	-0.145	0.228	0.086
C	-0.264836	0.005	0.373	-0.042
C	0.184476	0.08	0.261	-0.086
C	-0.050174	0.04	0.13	-0.043
C	0.052586	-0.072	0.115	0.043
C	-0.264834	0.192	0.273	-0.171
C	0.149459	0.264	0.162	-0.214
C	-0.027963	0.225	0.03	-0.171
C	0.05258	0.113	0.016	-0.086

C	-0.137266	0.379	0.174	-0.301
C	-0.138306	0.448	0.064	-0.341
C	0.100502	0.411	-0.069	-0.3
C	0.009172	0.297	-0.084	-0.214
C	-0.15385	0.481	-0.184	-0.34
C	-0.153847	0.442	-0.31	-0.299
H	0.086443	0.345	-0.545	-0.202
H	0.086544	0.151	-0.572	-0.054
H	0.084711	-0.036	-0.472	0.075
H	0.084711	-0.222	-0.372	0.204
H	0.086544	-0.409	-0.272	0.334
H	0.086443	-0.534	-0.075	0.407
H	0.085651	-0.567	0.172	0.405
H	0.085651	-0.498	0.397	0.331
H	0.086442	-0.345	0.545	0.202
H	0.086544	-0.151	0.572	0.054
H	0.084711	0.036	0.472	-0.075
H	0.084711	0.222	0.372	-0.204
H	0.086545	0.409	0.272	-0.334
H	0.086442	0.534	0.075	-0.407
H	0.085652	0.566	-0.173	-0.406
H	0.085653	0.497	-0.397	-0.332

Atomic partial charges for V_0.

Atom	Charge (*e*)	X (nm)	Y (nm)	Z (nm)
C	0.118813	-0.058	-0.401	-0.077
C	-0.046108	-0.054	-0.31	0.028
C	-0.02254	-0.156	-0.221	0.06
C	0.065009	-0.271	-0.198	-0.019
C	-0.122439	-0.29	-0.307	-0.115
C	-0.125591	-0.188	-0.406	-0.14
C	-0.125627	0.073	-0.458	-0.106
C	-0.122418	0.194	-0.403	-0.052

C	0.065047	0.194	-0.291	0.042
C	-0.022651	0.063	-0.264	0.088
C	0.064896	-0.323	-0.055	-0.002
C	-0.022384	-0.245	0.019	0.088
C	-0.046186	-0.224	0.157	0.082
C	0.11882	-0.294	0.243	-0.003
C	-0.125625	-0.402	0.176	-0.073
C	-0.122389	-0.414	0.032	-0.076
C	-0.02254	-0.102	0.186	0.141
C	0.065139	-0.022	0.299	0.11
C	-0.122434	-0.101	0.4	0.041
C	-0.125658	-0.233	0.375	-0.01
C	-0.010627	-0.153	-0.024	0.177
C	-0.010442	-0.07	0.074	0.209
C	-0.010366	0.022	-0.174	0.18
C	-0.010515	-0.107	-0.149	0.163
C	-0.010548	0.106	-0.076	0.211
C	-0.022661	0.225	-0.075	0.149
C	0.065181	0.291	-0.178	0.077
C	-0.010591	0.061	0.048	0.226
C	-0.022514	0.148	0.136	0.174
C	-0.046193	0.261	0.061	0.146
C	-0.122506	0.423	-0.134	0.034
C	-0.125716	0.466	0.003	0.04
C	0.119044	0.378	0.109	0.085
C	0.065003	0.127	0.268	0.13
C	-0.122354	0.252	0.33	0.087
C	-0.125744	0.373	0.254	0.07
H	0.09072	-0.376	-0.302	-0.18
H	0.089022	-0.204	-0.476	-0.222
H	0.089003	0.081	-0.532	-0.185
H	0.090733	0.289	-0.435	-0.094
H	0.08902	-0.465	0.235	-0.14
H	0.090741	-0.482	-0.013	-0.147
H	0.090703	-0.051	0.493	0.014
H	0.089005	-0.281	0.45	-0.071
H	0.090732	0.485	-0.206	-0.02
H	0.089032	0.56	0.03	-0.006

H	0.090694	0.25	0.433	0.054
H	0.08901	0.46	0.303	0.025

B. Tabulation of collision efficiency data

All collision efficiency data plotted in Chapter 4 is given here in tabular form:

I_0

Temperature (K)	β	±βErr
500	0.10214	0.00626
750	0.02544	0.00274
1000	0.00438	0.00109
1500	2.48E-04	2.47E-04

I_1

Temperature (K)	β	±βErr
500	0.17904	0.00918
750	0.05409	0.00376
1000	0.00872	0.00147
1500	7.50E-05	7.49E-05

I_2

Temperature (K)	β	±βErr
500	0.27695	0.01196
750	0.08008	0.00413
1000	0.00976	0.00143
1500	6.06E-05	6.05E-05

II_0

Temperature (K)	β	±βErr
500	0.25255	0.01324
750	0.12116	0.00678
1000	0.05052	0.00353

1500	0.00741	0.00128

II_1

Temperature (K)	β	±βErr
500	0.36118	0.01722
750	0.18492	0.00903
1000	0.0882	0.00436
1500	0.00594	0.00108

II_2

Temperature (K)	β	±βErr
500	0.43015	0.01841
750	0.22382	0.01041
1000	0.10555	0.00433
1500	0.0069	0.00101

III_0

Temperature (K)	β	±βErr
500	0.40084	0.01831
750	0.22231	0.01174
1000	0.14601	0.00734
1500	0.03512	0.00262

IV_0

Temperature (K)	β	±βErr
500	0.53231	0.02058
750	0.32418	0.01552
1000	0.18194	0.00994
1500	0.08917	0.0042

V_0

Temperature (K)	β	±β_{Err}
500	0.52234	0.0207
750	0.22017	0.0098
1000	0.10864	0.00525
1500	0.01472	0.00188

I_0-II_0

Temperature (K)	β	±β_{Err}
500	0.2	0.01368
750	0.07108	0.00632
1000	0.01605	0.00286
1500	0.00275	0.00112

I_0-III_0

Temperature (K)	β	±β_{Err}
500	0.60556	0.03643
750	0.40966	0.0208
1000	0.18868	0.0112
1500	0.01999	0.00325

II_0-III_0

Temperature (K)	β	±β_{Err}
500	0.59135	0.03409
750	0.51003	0.02676
1000	0.31042	0.01539
1500	0.04982	0.00488

References

[1] Seinfeld JH, Pandis SN. Atmospheric Chemistry and Physics - From Air Pollution to Climate Change. Wiley-Interscience 1997.

[2] Jacobson MZ. Short-term effects of controlling fossil-fuel soot, biofuel soot and gases, and methane on climate, Arctic ice, and air pollution health. J Geophys Res. 2010;115(D14):D14209.

[3] Lave LB, Seskin EP. An Analysis of the Association Between U. S. Mortality and Air Pollution. Journal of the American Statistical Association. 1973;68(342):284-90.

[4] Mokdad AH, Marks JS, Stroup DF, Gerberding JL. Actual Causes of Death in the United States, 2000. JAMA: The Journal of the American Medical Association. 2004;291(10):1238-45.

[5] Sabbah H, Biennier L, Klippenstein SJ, Sims IR, Rowe BR. Exploring the Role of PAHs in the Formation of Soot: Pyrene Dimerization. Journal of Physical Chemistry Letters. 2010 Oct;1(19):2962-7.

[6] Frenklach M. Reaction mechanism of soot formation in flames. Physical Chemistry Chemical Physics. 2002;4(11):2028-37.

[7] Pope CJ, Howard JB. - Simultaneous Particle and Molecule Modeling (SPAMM): An Approach for Combining Sectional Aerosol Equations and Elementary Gas-Phase Reactions. 1997.

[8] Appel J, Bockhorn H, Frenklach M. Kinetic modeling of soot formation with detailed chemistry and physics: Laminar premixed flames of C-2 hydrocarbons. Combustion and Flame. 2000 Apr;121(1-2):122-36.

[9] Colket MB, Hall RJ. In: Bockhorn H, ed. Soot Formation in Combustion: Mechanisms and Models. Heidelberg: Springer-Verlag 1994:442.

[10] Frenklach M, Harris SJ. Aerosol dynamics modeling using the method of moments. Journal of Colloid and Interface Science. 1987;118(1):252-61.

[11] Bockhorn H. Soot Formation in Combustion: Mechanisms and Models of Soot Formation. Berlin: Springer-Verlag 1994.

[12] Haynes BS, Wagner HG. Soot Formation. Progress in Energy and Combustion Science. 1981;7(4):229-73.

[13] Calcote HF. Mechanisms of soot nucleation in flames--A critical review. Combustion and Flame. 1981;42:215-42.

[14] Homann KH. Formation of large molecules, particulates and ions in premixed hydrocarbon flames; Progress and unresolved questions. Symposium (International) on Combustion. 1985;20(1):857-70.

[15] Glassman I. Soot formation in combustion processes. Symposium (International) on Combustion. 1989;22(1):295-311.

[16] Richter H, Howard JB. Formation of polycyclic aromatic hydrocarbons and their growth to soot--a review of chemical

reaction pathways. Progress in Energy and Combustion Science. 2000;26(4-6):565-608.

[17] Frenklach M, Wang H. Detailed modeling of soot particle nucleation and growth. Symposium (International) on Combustion. 1991;23(1):1559-66.

[18] Vander Wal RL, Yezerets A, Currier NW, Kim DH, Wang CM. HRTEM Study of diesel soot collected from diesel particulate filters. Carbon. 2007;45(1):70-7.

[19] Warren DR, Seinfeld JH. Prediction of aerosol concentrations resulting from a burst of nucleation. Journal of Colloid and Interface Science. 1985;105(1):136-42.

[20] Herdman JD, Miller JH. Intermolecular potential calculations for polynuclear aromatic hydrocarbon clusters. Journal of Physical Chemistry A. 2008 Jul;112(28):6249-56.

[21] Wedekind J, Reguera D, Strey R. Finite-size effects in simulations of nucleation. The Journal of Chemical Physics. 2006;125(21):214505-7.

[22] Stein SE, Fahr A. High-temperature stabilities of hydrocarbons. Journal of Physical Chemistry. 1985;89(17):3714-25.

[23] Frenklach M, Clary DW, Gardiner JWC, Stein SE. Detailed kinetic modeling of soot formation in shock-tube pyrolysis of acetylene. Symposium (International) on Combustion. 1985;20(1):887-901.

[24] Frenklach M, Wang H. In: Bockhorn H, ed. Soot Formation in Combustion: Mechanisms and Models. Heidelberg: Springer-Verlag 1994:165.

[25] Miller JH, Smyth KC, Mallard WG. Calculations of the dimerization of aromatic hydrocarbons: Implications for soot formation. Symposium (International) on Combustion. 1985;20(1):1139-47.

[26] Miller JH. The kinetics of polynuclear aromatic hydrocarbon agglomeration in flames. Symposium (International) on Combustion. 1991;23(1):91-8.

[27] Schuetz CA, Frenklach M. Nucleation of soot: Molecular dynamics simulations of pyrene dimerization. Proceedings of the Combustion Institute. 2002;29:2307-14.

[28] Kazakov A, Wang H, Frenklach M. Detailed modeling of soot formation in laminar premixed ethylene flames at a pressure of 10 bar. Combustion and Flame. 1995 Jan;100(1-2):111-20.

[29] Bai XS, Balthasar M, Mauss F, Fuchs L. Detailed soot modeling in turbulent jet diffusion flames. Pittsburgh: Combustion Institute 1998.

[30] Mosbach S, Celnik MS, Raj A, Kraft M, Zhang HR, Kubo S, et al. Towards a detailed soot model for internal combustion engines. Combustion and Flame. 2009 Jun;156(6):1156-65.

[31] Chung S-H, Violi A. Peri-condensed aromatics with aliphatic chains as key intermediates for the nucleation of aromatic hydrocarbons. Proceedings of the Combustion Institute. 2011;33(1):693-700.

[32] Chung SH, Violi A. Insights on the formation and growth of carbonaceous nanoparticles in high temperature environments. In: Bockhorn H, D'Anna. A, Sarafim AF, Wang H, eds. Combustion Generated Fine Carbonaceous Particles. Villa Orlandi, Anacapri: Karlsruhe University Press 2007:321-32.

[33] Chung SH, Violi A. Insights on the nanoparticle formation process in counterflow diffusion flames. Carbon. 2007 Oct;45(12):2400-10.

[34] Kang KT, Hwang JY, Chung SH, Lee W. Soot zone structure and sooting limit in diffusion flames: Comparison of counterflow and co-flow flames. Combustion and Flame. 1997 Apr;109(1-2):266-81.

[35] Violi A, Sarofim AF, Voth GA. Kinetic Monte Carlo molecular dynamics approach to model soot inception. 3rd Mediterranean Combustion Symposium. Marrakech, Morocco: Taylor & Francis Ltd 2003:991-1005.

[36] Violi A, Voth GA, Sarofim AF. The relative roles of acetylene and aromatic precursors during soot particle inception. 30th International Symposium on Combustion. Chicago, IL: Combustion Inst 2004:1343-51.

[37] Violi A. Modeling of soot particle inception in aromatic and aliphatic premixed flames. Combustion and Flame. 2004;139(4):279-87.

[38] Violi A, Sarofim AF, Voth GA. Kinetic Monte Carlo molecular dynamics approach to model soot inception. Combustion Science and Technology. 2004;176(5-6):991-1005.

[39] Violi A, Voth GA. A multi-scale computational approach for nanoparticle growth in combustion environments. In: Yang LT, Rana OF, DiMartino B, Dongarra J, eds. 1st International on High Performance Computing and Communications (HPCC 2005). Sorrento, ITALY: Springer-Verlag Berlin 2005:938-47.

[40] Violi A, Venkatnathan A. Combustion-generated nanoparticles produced in a benzene flame: A multiscale approach. Journal of Chemical Physics. 2006 Aug;125(5):8.

[41] Violi A, Izvekov S. Soot primary particle formation from multiscale coarse-grained molecular dynamics simulation. Proceedings of the Combustion Institute. 2007;31:529-37.

[42] Bortz AB, Kalos MH, Lebowitz JL. A new algorithm for Monte Carlo simulation of Ising spin systems. Journal of Computational Physics. 1975;17(1):10-8.

[43] Lutz AE, Kee RJ, Grcar JF, Rupley FM. OPPDIF: A Fortran program for computing opposed-flow diffusion flames; 1996.

[44] Ni B, Lee KH, Sinnott SB. A reactive empirical bond order (REBO) potential for hydrocarbon-oxygen interactions. Journal of Physics-Condensed Matter. 2004 Oct;16(41):7261-75.

[45] Brenner DW, Shenderova OA, Harrison JA, Stuart SJ, Ni B, Sinnott SB. A second-generation reactive empirical bond order (REBO) potential energy expression for hydrocarbons. Journal of Physics-Condensed Matter. 2002 Feb;14(4):783-802.

[46] Brenner DW. The art and science of an analytic potential. Physica Status Solidi B-Basic Research. 2000 Jan;217(1):23-40.

[47] Brenner DW. Empirical Potential for Hydrocarbons for Use in Simulating the Chemical Vapor-Deposition of Diamond Films. Physical Review B. 1990 Nov;42(15):9458-71.

[48] Mayo SL, Olafson BD, Goddard WA. Dreiding - a Generic Force-Field for Molecular Simulations. Journal of Physical Chemistry. 1990 Dec;94(26):8897-909.

[49] Hudson GH, McCoubrey JC. Intermolecular Forces between Unlike Molecules - a More Complete Form of the Combing Rules. Transactions of the Faraday Society. 1960;56(6):761-6.

[50] Senent ML, Smeyers YG, Dominguez-Gomez R, Villa M. Ab initio determination of the far infrared spectra of some isotopic varieties of ethanol. Journal of Chemical Physics. 2000 Apr;112(13):5809-19.

[51] Xu LH, Lees RM, Hougen JT. On the physical interpretation of torsion-rotation parameters in methanol and acetaldehyde: Comparison of global fit and ab initio results. Journal of Chemical Physics. 1999 Feb;110(8):3835-41.

[52] Flaud JM, Camypeyret C, Johns JWC, Carli B. The Far Infrared-Spectrum of H2o2 - 1st Observation of the Staggering of the Levels and Determination of the Cis Barrier. Journal of Chemical Physics. 1989 Aug;91(3):1504-10.

[53] Francisco J. Internal rotational barriers of ClOOCl. Journal of Chemical Physics. 1995;103(20):8921.

[54] Maria U. Alzueta PGKD-J. Experimental and kinetic modeling study of the oxidation of benzene. International Journal of Chemical Kinetics. 2000;32(8):498-522.

[55] Zhong X, Bozzelli JW. Thermochemical and Kinetic Analysis of the H, OH, HO2, O, and O2 Association Reactions with Cyclopentadienyl Radical. J Phys Chem A. 1998;102(20):3537-55.

[56] Frank P, Herzler J, Just T, Wahl C. High Temperature Reaction of Phenyl Oxidation. Twenty-Fifth Symposium (International) on Combustion; 1994: The Combustion Institute, Pittsburgh; 1994. p. 833.

[57] Miller JA, Melius CF. Kinetic and thermodynamic issues in the formation of aromatic compounds in flames of aliphatic fuels. Combustion and Flame. 1992;91(1):21-39.

[58] Tsang W, Hampson RF. Chemical Kinetic Data Base for Combustion Chemistry. Part I. Methane and Related Compounds. Journal of Physical and Chemical Reference Data. 1986;15(3):1087-279.

[59] Manion JA, Louw R. Rates, products, and mechanisms in the gas-phase hydrogenolysis of phenol between 922 and 1175 K. J Phys Chem. 1989;93(9):3563-74.

[60] Emdee JL, Brezinsky K, Glassman I. A kinetic model for the oxidation of toluene near 1200 K. J Phys Chem. 1992;96(5):2151-61.

[61] Knispel R, Koch R, Siese M, Zetzsch C. Ber Bunsenges Phys Chem. 1990;94:1375.

[62] Ko T, Flaherty WF, Fontijn A. Flow-tube kinetics study of the reaction between ground-state hydrogen atoms and nitromethane. J Phys Chem. 1991;95(18):6967-70.

[63] Madronich S, Felder W. Kinetics and mechanism of the reaction of hydroxyl with benzene. J Phys Chem. 1985;89(16):3556-61.

[64] Baulch DL, Cobos CJ, Cox RA, Esser C, Frank P, Th J, et al. Evaluated Kinetic Data for Combustion Modelling. Journal of Physical and Chemical Reference Data. 1992;21(3):411-734.

[65] Du J, Axelbaum RL. The Effect of Flame Structure on Soot-Particle Inception in-Diffusion Flames. Combustion and Flame. 1995 Feb;100(3):367-75.

[66] Violi A, D'Anna A, D'Alessio A, Sarofim AF. Modeling aerosol formation in opposed-flow diffusion flames. Chemosphere. 2003 Jun;51(10):1047-54.

[67] Hwang JY, Lee W, Kang HG, Chung SH. Synergistic Effect of Ethylene-Propane Mixture on Soot Formation in Laminar Diffusion Flames. Combustion and Flame. 1998;114(3-4):370-80.

[68] Hwang JY, Chung SH. Growth of soot particles in counterflow diffusion flames of ethylene. Combustion and Flame. 2001;125(1-2):752-62.

[69] Violi A. Cyclodehydrogenation reactions to cyclopentafused polycyclic aromatic hydrocarbons. Journal of Physical Chemistry A. 2005 Sep;109(34):7781-7.

[70] Frenklach M, Wang H. Twenty-Third Symposium (International) on Combustion; 1990: The Combustion Institute, Pittsburgh; 1990. p. 1559–66.

[71] Harris SJ, Weiner AM. Twenty-Second Symposium (International) on Combustion; 1988: The Combustion Institute, Pittsburgh; 1988. p. 333–42.

[72] Macadam S, Beer JM, Sarofim AF, Hoffmann AB. Soot surface growth by polycyclic aromatic hydrocarbon and acetylene addition. In: Anon, editor. Symposium (International) on Combustion; 1996; Napoli, Italy: Combustion Inst; 1996. p. 2295-302.

[73] Girifalco LA. Molecular properties of fullerene in the gas and solid phases. J Phys Chem. 1992;96(2):858-61.

[74] Girifalco LA, Hodak M, Lee RS. Carbon nanotubes, buckyballs, ropes, and a universal graphitic potential. Physical Review B. 2000;62(19):13104.

[75] Yannoni CS, Johnson RD, Meijer G, Bethune DS, Salem JR. Carbon-13 NMR study of the C60 cluster in the solid state: molecular motion and carbon chemical shift anisotropy. J Phys Chem. 1991;95(1):9-10.

[76] Doye JPK, Wales DJ. Magic numbers and growth sequences of small face-centered-cubic and decahedral clusters. Chemical Physics Letters. 1995;247(4-6):339-47.

[77] Rey C, García-Rodeja J, Gallego LJ, Alonso JA. Clusters and layers of C60 molecules supported on a graphite substrate. Physical Review B. 1997;55(11):7190.

[78] Wedekind J, Reguera D, Strey R. Influence of thermostats and carrier gas on simulations of nucleation. The Journal of Chemical Physics. 2007;127(6):064501-12.

[79] Smith W, Forester TR. DL_POLY_2.0: A general-purpose parallel molecular dynamics simulation package. Journal of Molecular Graphics. 1996;14(3):136-41.

[80] Lindemann FA. The calculation of molecular natural frequencies. Physikalische Zeitschrift. 1910;11:609-12.

[81] Gallego LJ, Garcia-Rodeja J, Alemany MMG, Rey C. Solidlike-to-liquidlike transition in small clusters of C-60 molecules or transition-metal atoms. Physical Review Letters. 1999 Dec;83(25):5258-61.

[82] Piatek A, Dawid A, Gburski Z. The existence of a plastic phase and a solid-liquid dynamical bistability region in small fullerene cluster (C-60)(7): molecular dynamics simulation. Journal of Physics-Condensed Matter. 2006 Sep;18(37):8471-80.

[83] Steinfeld IJ, Francisco SJ, Hase LW. Chemical Kinetics and Dynamics: Prentice Hall 1989.

[84] Minutolo P, Gambi G, D'Alessio A, Carlucci S. Spectroscopic characterisation of carbonaceous nanoparticles in premixed flames. Atmospheric Environment. 1999;33(17):2725-32.

[85] Santoro RJ, Yeh TT, Horvath JJ, Semerjian HG. The Transport and Growth of Soot Particles in Laminar Diffusion Flames. Combustion Science and Technology. 1987;53(2):89 - 115.

[86] Flower WL, Bowman CT. Soot production in axisymmetric laminar diffusion flames at pressures from one to ten atmospheres. Symposium (International) on Combustion. 1988;21(1):1115-24.

[87] Flower WL, Bowman CT. Measurements of the structure of sooting laminar diffusion flames at elevated pressures. Symposium (International) on Combustion. 1985;20(1):1035-44.

[88] Minutolo P, Gambi G, D'Alessio A. Properties of carbonaceous nanoparticles in flat premixed C2H4/air flames with C/O ranging from 0.4 to soot appearance limit. Twenty-Seventh Symposium (International) on Combustion, Vols 1 and 2. 1998:1461-9.

[89] Raj A, Sander M, Janardhanan V, Kraft M. A study on the coagulation of polycyclic aromatic hydrocarbon clusters to determine their collision efficiency. Combustion and Flame. 2010;157(3):523-34.

[90] Kee RJ, Rupley FM, Miller JA, Coltrin ME, J. F. Grcar EM, Moffat HK, et al. CHEMKIN Release 4.1.1. San Diego, CA: Reaction Design 2007.

[91] Vandewaal BW. Calculated ground-state structures of 13-molecule clusters of carbon-dioxide, methane, benzene, cyclohexane, and naphthalene. Journal of Chemical Physics. 1983;79(8):3948-61.

[92] Frisch MJ, Trucks GW, Schlegel HB, Scuseria GE, Robb MA, Cheeseman JR, et al. Gaussian 03. Revision C.02 ed. Wallingford CT: Gaussian, Inc. 2004.

[93] Becke AD. Density-functional thermochemistry .3. The role of exact exchange. Journal of Chemical Physics. 1993 Apr;98(7):5648-52.

[94] Lee CT, Yang WT, Parr RG. Development of the colle-salvetti correlation-energy formula into a functional of the electron-density. Physical Review B. 1988 Jan;37(2):785-9.

[95] Miehlich B, Savin A, Stoll H, Preuss H. Results obtained with the correlation-energy density functionals of Becke and Lee, Yang and Parr. Chemical Physics Letters. 1989 May;157(3):200-6.

[96] Jorgensen WL, Tiradorives J. The OPLS potential functions for proteins - energy minimizations for crystals of cyclic-peptides and crambin. Journal of the American Chemical Society. 1988 Mar;110(6):1657-66.

[97] Kaminski GA, Friesner RA, Tirado-Rives J, Jorgensen WL. Evaluation and reparametrization of the OPLS-AA force field for proteins via comparison with accurate quantum chemical calculations on peptides. Journal of Physical Chemistry B. 2001 Jul;105(28):6474-87.

[98] Hoover WG. Canonical dynamics - equilibrium phase space distributions. Physical Review A. 1985;31(3):1695-7.

[99] Van der Spoel D, Lindahl E, Hess B, Groenhof G, Mark AE, Berendsen HJC. GROMACS: Fast, flexible, and free. Journal of Computational Chemistry. 2005 Dec;26(16):1701-18.

[100] Harvey SC, Tan RKZ, Cheatham TE. - The flying ice cube: Velocity rescaling in molecular dynamics leads to violation of energy equipartition. 1998.

[101] Frenklach M, Wang H, Goldenberg M, Smith GP, Golden DM, Bowman CT, et al. Chicago: Gas Research Institute; 1995.

[102] Wang H, Frenklach M. A detailed kinetic modeling study of aromatics formation in laminar premixed acetylene and ethylene flames. Combustion and Flame. 1997;110(1-2):173-221.

[103] Marr JA. PAH chemistry in a jet-stirred/plug-flow reactor system: Massachusetts Institute of Technology; 1985.

[104] Meeks E, Chow C-P. Accurate Predictions of Chemical Phenomena in Chemically Reacting Flows. European Conference on Computational Fluid Dynamics. The Netherlands 2006.

[105] Chung S-H, Violi A. Dimerization of polycyclic aromatic hydrocarbon molecules and their collision efficiency. 2011.

[106] Wen JZ, Thomson MJ, Park SH, Rogak SN, Lightstone MF. Study of soot growth in a plug flow reactor using a moving sectional model. Proceedings of the Combustion Institute. 2005;30(1):1477-84.

[107] Kronholm DF. Molecular Weight Growth Pathways in Fuel-Rich Combustion: Massachusetts Institute of Technology; 2000.